Title

Phase transition and domain wall control in multistable metamaterials

Permalink

https://escholarship.org/uc/item/0tv890c6

Author

Ramakrishnan, Vinod

Publication Date

2023

Peer reviewed|Thesis/dissertation

UNIVERSITY OF CALIFORNIA SAN DIEGO

Phase transition and domain wall control in multistable metamaterials

A dissertation submitted in partial fulfillment of requirements

for the degree of Doctor of Philosophy

in

Engineering Sciences

(Mechanical Engineering)

by

Vinod Ramakrishnan

Committee in Charge :

Professor Michael J. Frazier, Chair
Professor Nicholas S. Boechler
Professor James R. Friend
Professor Hyunsun A. Kim

2023

The dissertation of *Vinod Ramakrishnan* is approved, and it is acceptable in quality and form for publication on microfilm and electronically.

University of California San Diego

2023

DEDICATION

“Dedicated to my parents Bhanumathi Jayaraman and Ramakrishnan Dharmarajan, my younger brother Karthik Ramakrishnan, for their unconditional love and support and, to my grandparents and extended family for their blessings and well wishes”

EPIGRAPH

कर्मण्येवाधिकारस्ते मा फलेषु कदाचन ।

मा कर्मफलहेतुर्भूर्मा ते सङ्गोऽस्त्वकर्मणी ॥ २-४७ ॥

– Bhagawan Krishna, Shrimad Bhagavad Gita

Chapter 2, Shloka 47

Meaning of Shloka - You only have control over your actions (कर्म). However, the outcomes of your actions (कर्मफल) are beyond your control. Therefore, don't let your desire for a favourable outcome dictate your actions and, keep performing your duty bound actions without contemplating the results.

TABLE OF CONTENTS

LIST OF FIGURES

LIST OF TABLES

ACKNOWLEDGEMENTS

My graduate journey at UCSD has been a wonderful and enriching experience that has positioned me well for a career in research. I wish to acknowledge the support and efforts of multiple people who have helped me navigate the trials and tribulations along this journey and become ‘Dr. Vinod Ramakrishnan’.

I would like to thank my PhD advisor Prof. Michael J. Frazier for his invaluable mentorship and guidance. I appreciate his patient and systematic approach in nurturing independent thinking skills, in-depth knowledge in my research area and helping me grow as a well rounded researcher. I would also like to acknowledge my labmates Jack and Chongan for their insights, feedback, critiques and engaging discussions related to research and graduate life in general.

I would like to thank Mr. Chris Cassidy from the MAE Design Studio, Dr. Steve Roberts from the Electronics lab, Mr. Ian Richardson from the MAE Machine shop and my undergraduate research assistant Haoyi Tian for helping with the experimental setup for the final project in this dissertation. I would like to thank my doctoral committee members - Prof. Nicholas Boechler, Prof. James Friend and Prof. Alicia Kim for their timely research inputs that have enhanced the quality of my dissertation and helped me improve my research and presentation skills.

I would like to thank my parents Bhanumathi Jayaraman and Ramakrishnan Dharmarajan, younger brother Karthik Ramakrishnan and my extended family for being a pillar of strength and inspiration and a source of unconditional love and support. Finally, I would like to thank my friends Somayajulu, Ayushman, Soumya, Digvijay, Saumya, Karan, Vivek, Aparna, Manas, Brianna, Jai, Srinivas, Pravalika, Sharath and my undergraduate friends Harsh Modi, Vismay, Chinmay Sonar, Vaidy, Amogh, Kshiteej, Kaustubh, Arvind, Chinmay Shirpurkar, Pinank and Kapil from

IITGN for their engaging discussions on a variety of topics from research and academics to career, hobbies, social and cultural issues and for keeping me motivated and sane through the turbulent times of COVID and my overall graduate journey.

Chapter 2, in full, is a reprint of the material as it appears in V. Ramakrishnan and M. J. Frazier, “Architected material with independently tunable mass, damping, and stiffness via multi-stability and kinematic amplification”, *J. Acoust. Soc. Am.*, **vol. 153**, **no. 2**, pp. 1283-1292, February 2023. The dissertation author is the primary author of this paper.

Chapter 3, in full, is a reprint of the material as it appears in V. Ramakrishnan and M. J. Frazier, “Multistable metamaterial on elastic foundation enables tunable morphology for elastic wave control”, *J. Appl. Phys.*, **vol. 127**, p. 225104, June 2020. The dissertation author is the primary author of this paper.

Chapter 4, in full, is a reprint of the material as it appears in V. Ramakrishnan and M. J. Frazier, “Transition waves in multi-stable metamaterials with space-time modulated potentials”, *Appl. Phys. Lett.*, **vol. 117**, p. 151901, October 2020. The dissertation author is the primary author of this paper.

Chapter 5, in part, is currently being prepared for submission for publication of the material. V. Ramakrishnan and M. J. Frazier. The dissertation author is the primary author of this material.

VITA

Year	Institution	Degree
2014 - 2018	IIT Gandhinagar	B. Tech, Mechanical Engineering
2018 - 2020	University of California San Diego	MS, Engineering Sciences (Mechanical Engineering)
2018 - 2023	University of California San Diego	PhD, Engineering Sciences (Mechanical Engineering)

Publications

- V. Ramakrishnan and M. J. Frazier, "Architected material with independently tunable mass, damping, and stiffness via multi-stability and kinematic amplification", *J. Acoust. Soc. Am.*, **153**, 1283-1292 (2023)
- V. Ramakrishnan and M. J. Frazier, "Transition waves in multi-stable metamaterials with space-time modulated potentials", *Appl. Phys. Lett.*, **117**, 151901 (2020).
- V. Ramakrishnan and M. J. Frazier, "Multistable metamaterial on elastic foundation enables tunable morphology for elastic wave control", *J. Appl. Phys.*, **127**, 225104 (2020)

Conference Presentations

- V. Ramakrishnan, M. J. Frazier, "Metamaterials With Independently Tunable Acoustic Properties", at International Mechanical Engineering Congress and Exposition 2022, Columbus, OH, October 31 - November 3, 2022.
- V. Ramakrishnan, M. J. Frazier, "Metamaterial with Independently Tunable Mass, Damping and Stiffness", at Engineering Mechanics Institute Conference 2022, Baltimore, MD, May 31 - June 3, 2022.
- V. Ramakrishnan, M. J. Frazier, "Vibration Induced Spatial Ordering of Periodic Patterns in Multistable Metamaterials", at International Mechanical Engineering Congress and Exposition 2021, Virtual, November 1 - 4, 2021.
- V. Ramakrishnan, M. J. Frazier, "Transition Wave Control in Multi-Stable Metamaterials with Space-Temporal Elasticity", at Engineering Mechanics Institute Conference 2021, Virtual, May 25 - 28, 2021.
- V. Ramakrishnan, M. J. Frazier, "Transition Waves in Multi-stable Metamaterials with Space-time Modulated Potentials", at International Mechanical Engineering Congress and Exposition 2020, Virtual, November 16 - 19, 2020.

- V. Ramakrishnan, M. J. Frazier, “Multistable Architectures on Elastic Foundation for Tunable, Reversible Wave Propagation”, at International Mechanical Engineering Congress and Exposition 2019, Salt Lake City, UT, November 11 - 14, 2019.
- V. Ramakrishnan, M. J. Frazier, “Multistable Architectures on Elastic Foundation for Tunable, Reversible Wave Propagation”, at Engineering Mechanics Institute Conference 2019, Pasadena, CA, June 18 - 21, 2019.

ABSTRACT OF THE DISSERTATION

Phase transition and domain wall control in multistable metamaterials

by

Vinod Ramakrishnan

Doctor of Philosophy in Engineering Sciences

(Mechanical Engineering)

University of California San Diego, 2023

Professor Michael J. Frazier, Chair

Ferroics and metal alloys are naturally occurring materials, whose constituent unit cells can co-exist in multiple stable configurations. These different configurations organize into regions (domains) separated by boundaries (domain walls). The stable configurations (phases) are associated with a unique set of properties (e.g., dipole orientation, stiffness), rendering the mesoscale phase distributions a crucial factor in determining macroscale material behavior; hence, the desire to control the distribution. Inspired by non-linear physics and potential applications of these natural materials, this dissertation explores similar physics in materials of an engineered microstructure (metamaterials) featuring purely geometric phases, and develops strategies to control domain walls. The domain management strategies enable control of the phase distribution and thereby the macroscale properties, allowing for a highly tunable post-fabrication performance.

In my primary investigation, I leverage both geometric multistability and kinematic amplification in the metamaterial architecture to enable the effective mass, damping and stiffness to be tuned independently post-fabrication to control wave dispersion. In my second project, I introduce an alternate, less invasive strategy utilizing strain engineering to precisely control the phase distribution. In my third project, I propose a general theory to predict the position and velocity of mobile domain walls (i.e., transition waves) when subjected to a small spatio-temporal modulation. The modulations provide a mechanism to counter domain wall motion spurred by inherent energy minimizing affects (e.g., biased potential, domain wall curvature) which can be leveraged for stabilizing and arbitrarily shaping domain contours. Finally, inspired by the pattern forming dynamics of certain biological and chemical systems, I mimic the effects of the underlying driving and dissipative mechanisms within the context of a customizable mechanical system: an elastic metamaterial incorporating active elements (i.e., electric motors) facilitating non-reciprocal interactions. This construction encodes certain periodic phase distributions to be triggered as an inherent response of the metamaterial to perturbation, which may find utility in morphable surfaces.

In providing several strategies to realize and control the phase distributions within multistable metamaterials, this dissertation promotes their adoption for applications in energy harvesting, mechanical memory devices and deployable structures.

Chapter 1

Introduction

Architected Metamaterials

The field of material science and engineering has been extensively studying the atomic architecture of naturally occurring materials in an effort to understand their correlation with the macroscale material response. In recent years, architected metamaterials have emerged as a fantastic avenue to mimic the atomic architectures of natural materials in some form, at a more accessible scale allowing us to effectively control the macroscale material properties and in some cases, achieve novel, previously unseen material behavior.[1–6] Metamaterials overcome some limitations of natural materials (e.g., chemistry) by providing a purely geometric platform - a meticulously designed internal architecture to affect macroscale material response. Consequently, researchers have explored numerous models to prescribe and control mechanical and acoustic waves,[7–15] electromagnetic waves[16,17] and thermal response,[18–20] promising potentially interesting applications for metamaterials.

Propagation of waves is integral to the flow and distribution of energy, and metamaterials offer a much-awaited advancement over natural materials to the aspect of controllability of wave properties such as direction, phase, velocity, localization. In the context of mechanics and acoustics, the literature is repleted with innovative, original metamaterial designs and tuning methodologies to realize atypical mechanical properties such as negative effective inertia[6,21,22] and stiffness,[23,24] enhanced damping (metadamping[25]) and negative Poisson's ratio.[26–29] Researchers have exploited these newfound effects to create cloaking devices,[30–32] energy absorbers[22,33–35] and harvesters.[36,37] The bulk of these proposals involve unique structural geometries, with permanent material constituents (e.g., defects)[38–40] to affect the wave dynamics, limiting the operability to a specific application and offering little adaptability to changing requirements. Thus, the metamaterial community has been actively exploring techniques to augment the functionality of metamaterials to promote on-demand tuning. In this regard, infusing active elements (e.g., piezo-electrics,[41–48] magnets) into the metamaterial matrix has been investigated as a potential alternative. Once fabricated, the effective stiffness of the material can be altered in real time via electromechanical, electromagnetic coupling, to tune the dispersion characteristics based on the control input, significantly mitigating earlier design impediments. Although, the setup often involves complex circuit design, wiring and controllers and demands external drivers (i.e. electrical or magnetic) to operate. Similar post-fabrication tuning has been realized using soft material constituents endowed with geometric instability.[39,40,49,50] Models incorporating geometric instabilities rely on buckling and wrinkling of constituent elements which can be pre-programmed into the material design at the time of fabrication, eliminating the need to access the material bulk to alter the response. These designs offer a reversible, continuous tuning capability however, like active elements, rely on a steady external control stimuli, to artificially stabilize the material configuration.

Multistability and Phase Transitions in Metamaterials

Multistability overcomes these deficiencies and offers an improved ability to make continuous, reversible, and stable adjustments to the structure. Tuning is realized by re-configuring the material to one of the finite number of stable phases eliminating the need for external support, presenting an exciting opportunity to upgrade the functionality of materials and inspire further innovations in design strategies. Multistability is a naturally occurring phenomenon, encountered in chemical systems, ferro-electrics, multiferroics where the energy landscape can become non-convex and accommodate more than one stable phases. The propagation of topological solitons/transition waves in these materials are a model for transformation phenomena such as polarization switching in ferro-electric[51] and ferro-magnetic[52] materials, and structural phase transitions[53–55] etc, impacting material performance and promoting multi-functionality in applications.[56] Recently, mechanical metamaterials[57] characterized by multistable internal architectures have exhibited similar behavior,[58–66] extending atomic-scale physics and multi-functionality to the readily-accessible structural level. Therefore, command of the mesoscale phase distribution in multistable metamaterials, to affect macroscale material properties, promotes their utility in applications and is a central incentive and motivation for the work presented in this research proposal. In the subsequent chapters, I present a detailed overview of my investigations and findings, exploring different multistable metamaterial designs.

- **Chapter 2**[67]

  In my primary investigation, I leverage both geometric multistability and kinematic amplification in the metamaterial architecture to enable the effective mass, damping and stiffness to be tuned independently post-fabrication to control wave dispersion. In achieving this capability, we can affect greater control over linear wave propagation than permitted by earlier efforts. We can realize multiple effects, including inertial amplification,[68] metadamping,[25] band gap manipulation[69] on a single metamaterial platform.

- **Chapter 3**[70]

  In this project, I introduce a less invasive strategy utilizing strain engineering to precisely control the phase distribution. The strategy utilizes the non-uniform strain field generated in a heterogeneous substrate compressed/stretched at the boundaries to control the initiation, position, and size of domains within the overlaying metamaterial presenting a less invasive approach to tune the elastic properties without accessing the material bulk.

- **Chapter 4**[71]

  In this project, I propose a general theory to predict the position and velocity of mobile domain walls (i.e., transition waves) when subjected to a small spatio-temporal modulation. The strategy models transition waves as a quasi-particle and allows precise, on-demand control of the phase distribution. The theoretical results are supported by numerical analysis of a metamaterial architecture featuring on-site and inter-site multistability subjected to kinematic, spatio-temporal modulations. I then utilize customized spatio-temporal forcing to demonstrate reversibility in an energetically biased 1D lattice (tractor) and to counter the curvature (surface tension) effect, stabilizing the phase distribution in a 2D lattice (repulsor).

- **Chapter 5**

  Finally, inspired by the pattern forming dynamics of certain biological and chemical systems, I mimic the effects of the underlying driving and dissipative mechanisms within the context of a customizable mechanical system: an elastic metamaterial incorporating active elements (i.e., electric motors) facilitating non-reciprocal interactions. This construction encodes certain periodic phase distributions to be triggered as an inherent response of the metamaterial to perturbation, which may find utility in morphable surfaces. This project is a comprehensive endeavor where I analytically investigate and, validate the existence of mechanical Turing patterns in the architected material through numerical and experimental investigations.

Chapter 2

Architected Material with Independently Tunable Mass, Damping and Stiffness via Multi-stability and Kinematic Amplification

This chapter is published in:

The Journal of the Acoustical Society of America, **153**, 1283-1292 (2023)

DOI: 10.1121/10.0017346

2.1 Abstract

We report on a class of architected material lattices which exploit multistability and kinematic amplification to independently adjust the local effective mass, damping, and stiffness properties, thereby realizing congruent alterations to the acoustic dispersion response post-fabrication. The

fundamental structural tuning element permits a broad range in the effective property space; moreover, its particular design carries the benefit of tuning without altering the original size/shape of the emerging structure. The relation between the tuning element geometry and the achieved variability in effective properties is explored. Bloch's theorem facilitates the dynamic analysis of representative 1D/2D systems, revealing, e.g., band-gap formation, migration, and closure and positive/negative metadamping in accordance with the tuning element configuration. To demonstrate a utility, we improvise a waveguide by appropriately patterning the tuning element configuration within a 2D system. We believe that the proposed strategy offers a new way to expand the range of performance and functionality of architected materials for elastodynamics.

2.2 Introduction

Architected materials are a type of artificial media characterized by an engineered internal structure which engenders extraordinary effective properties and functionalities, and thus, have stimulated research across the range of materials science and engineering, including the thermal,[19,20] optical,[72,73] acoustic,[74–76] mechanical,[9,77,78] and biological[79,80] arenas. In the context of elastodynamics, architected materials[57,81,82] utilize their internal structure to manipulate the scattering and resonance phenomena peculiar to wave propagation, enabling an engineered dynamic response that has hitherto achieved, e.g., negative[6,8,83] and amplified[25,68] effective material properties as well as mimicked quantum mechanical[84–87] behavior, and has provided a foundation for new and expanded functionalities[88] and applications.[89] The periodicity typical of these architectures resembles the arrangement of molecules in crystalline solids; although, in the present context, the macroscopic "structural molecule" (i.e., unit cell) which determines the overall material response is of custom geometry and composition. Nevertheless, once fabricated, the unit cell architecture and the performance it engenders are generally fixed, rendering the architected material ill-suited for applications requiring adaptable performance. To broaden the range of response and enhance the functionality of architected materials in acoustics, a tuning capacity at the unit cell level is desirable and the overall aim of this article.

The literature gathers several strategies for tuning the architected material performance post-fabrication, including mechanical pre-loading,[90–92] integrated piezoelectric[43–48] and electromagnetic[38,93,94] elements, phase transitions,[95,96] mass redistribution,[97–99] and geometric instability[39,40,49,50] and multistability.[69,70,100–103] In general, the tuning is continuous, facilitating smooth adjustments to performance; moreover, the tuning is achieved via reversible processes, beneficially granting repeatability. Nevertheless, the above strategies also possess notable disadvantages. With the exception of multistability, each approach suffers the impermanence of the tuned state in the absence of sustained external stimulation. In addition, while these diverse approaches are able to manipulate the effective mass (density), damping, and stiffness relevant to the elastodynamic response, typically, the achieved tuning capability is limited to a single material property; methods that couple two or more properties tacitly accept the necessity for trade-off and compromise in their manipulation. For a more refined control of the wave dynamics, the literature is wanting in a strategy that permits all three properties relevant to wave dynamics to be independently adjusted, a privation which this article will address.

As a consequence of a non-convex potential, geometric multistability characterizes an internal architecture with more than one energy-minimizing configuration. A tuning capacity (albeit, discrete), as developed in the relevant works cited above, arises when the effective stiffness is configuration-dependent. Kinematic amplification describes the outsized motion of a rigid body in space due to the motion of another to which it is related via constraint. By incorporating amplifying mechanisms in the unit cell design, Yilmaz *et al.*[68] leverage enhanced accelerations to realize an inertial amplification effect and achieve wide, low-frequency band gaps in the dispersion diagram. Recently, Frazier[104] demonstrated a tuning strategy that applied both multistability and kinematic amplification toward a configuration-dependent effective mass and dispersion. In order to take full advantage of kinematic amplification and devise a multistable architecture with independently tunable mass, damping, and stiffness (i.e., the complete triad of elastodynamic properties), in addition to the enhanced accelerations, this article develops the basic approach by Frazier[104] to leverage the amplified displacements (for stiffness) and velocities (for dissipation), as well. In general, architectures with kinematic amplification exploit only the accelerations.[105–108] The electro-mechanical system proposed by Al Babaa *et al.*[47] – which amplifies displacements, velocities, and accelerations – is a notable exception; although, consistent with the above-cited methods, the tuned states are not stable and the material properties are coupled, provoking trade-offs.

In the following, we demonstrate the design strategy in one- and two-dimensional lattices where the specific configuration of a tuning element is reflected in the distinct frequency and damping ratio band diagrams produced by the associated complex dispersion relations, now, with tailorable material coefficients. In re-configuring the tuning element, we observe the formation, closure, and migration of band gaps, a change in the sonic wave speed, and both positive and negative metadamping; effects which have been observed across different unit cell designs in the literature, now, collectively achieved by the proposed tuning element. As an exemplary application, we construct a waveguide within a 2D system by spatially prescribing the element configuration and, thereby, the distribution of effective properties, demonstrating a post-fabrication customization in support of a desired function.

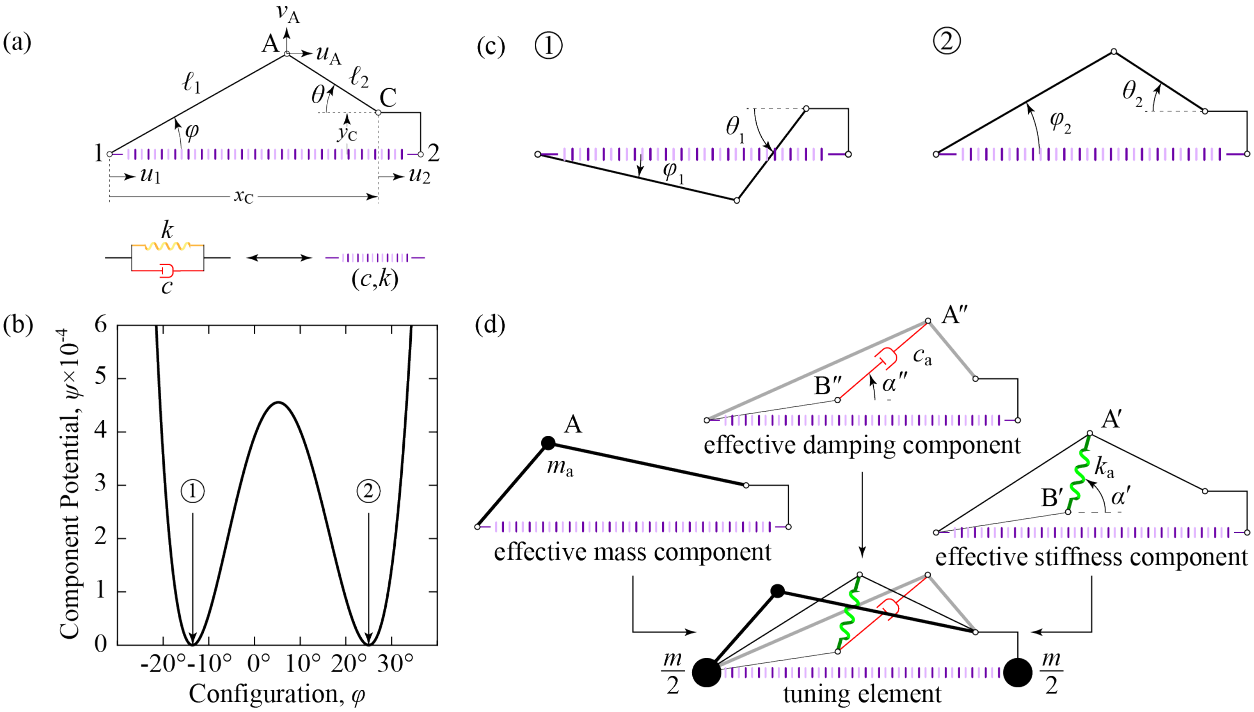

Figure 2.1: Multistable Tuning Element. (a) The bi-stable kinematic amplification component including two-bar linkage and offset. (b) The potential energy landscape indicating the component bi-stability and, by virtue of the symmetry, the recoverability of the elastic components. (c) Stable configurations, labeled according to φ_s where $\varphi_1 < \varphi_2$. (d) The mass, damping, and stiffness components unite to form the tuning element. To accompany k and c, a mass $m/2$ is associated with nodes 1 and 2. Apparently, for $m_a \to 0$, $c_a \to 0$, and $k_a \to 0$, the element reduces to a simple mass-spring-damper system lacking tunability.

2.3 Model Description

2.3.1 The Multistable Element

Central to the architected material tuning ability are the multistability and kinematic amplification provided by the internal architecture. To realize these effects, we exploit the geometry proposed by Frazier[104] (Fig. 2.1a) as a key component of the tuning element that, ultimately, enables adjustments to the effective mass, damping, and stiffness properties. The component comprises a simple, two-bar linkage together with a linear spring of stiffness, k, and a fluid damper of viscosity, c, coupling the motion of the free ends, i.e., nodes 1 and C. As the spring penalizes deformation, the component possesses a finite number of energetically stable arrangements distinguished by the configuration parameter, $\varphi \in [-\pi, \pi]$. Written explicitly, the configuration-dependent deformation energy is expressed as follows:

$$\psi(\varphi) = \frac{k}{2}\left(\sqrt{\ell_2^2 - [y_\mathrm{C} - \ell_1 \sin(\varphi)]^2} - |x_\mathrm{C} - \ell_1 \cos(\varphi)|\right)^2 \tag{2.1}$$

where $(x_\mathrm{C}, y_\mathrm{C})$ are the coordinates of node C as measured from node 1. For an arbitrary set of material and geometric parameters, Fig. 2.1b depicts the energy landscape described by Eq. (2.1), revealing two degenerate minimum-energy states, φ_s, $s = 1,2$ (Fig. 2.1c) indicative of both the component bi-stability and recoverability, i.e., the component regains its undeformed length, a, within each stable configuration. In addition, within the component, we identify two axes of deformation: the primary axis extending through nodes 1 and 2, and the secondary axis passing through nodes 1 and C. Let ℓ_C1 be the length of the segment $\overline{\mathrm{C1}}$. Since the two axes are non-parallel, $\varphi_1 \neq \varphi_2$ such that the response at node A is configuration-specific. Through the rigid-link mechanism, the motion of node A is directly related to that of the free ends. For small amplitude displacements along the primary axis (see Supplementary Material [SM], Sec. 2.6):

$$u_\mathrm{A} = \frac{u_2 + \tan(\theta_s)\cot(\varphi_s)u_1}{1 + \tan(\theta_s)\cot(\varphi_s)}, \tag{2.2a}$$

$$v_\mathrm{A} = (u_1 - u_2)\frac{\cos(\varphi_s)\cos(\theta_s)}{\sin(\varphi_s + \theta_s)}. \tag{2.2b}$$

where, respectively, u and v denote the horizontal and vertical displacement of a given node. The multistable tuning element (Fig. 2.1d) assembles three of the above-described components in order to effect independent adjustments to the effective mass, damping, and stiffness. To this end, while the lengths of the comprising rods may be unique to each rigid-link mechanism, their sum is identical (i.e., $\ell_1 + \ell_2 = \ell_1' + \ell_2' = \ell_1'' + \ell_2'' = L$) so that the process of switching any component from one configuration to another is not encumbered by the insufficient extension of the other components (see SM, Sec. 2.6). For clarity, $\square$, $\square'$, and $\square''$ denote corresponding parameters in the mass, stiffness, and damping components, respectively. Apparently, the inertia supplied by mass, m_{a}, resists the acceleration of node A. Similarly, k_{a} opposes the relative displacement between nodes A$'$ and B$'$; c_{a} opposes the relative velocity between nodes A$''$ and B$''$. To ensure that the deformation energy vanishes in each of the stable configurations (i.e., the element regains its undeformed length), we place node B$'$ along the secondary axis. To simplify the subsequent presentation, B$''$ is assumed co-located with B$'$. Let ℓ_{B1} be the length of the line segment $\overline{\mathrm{B}'1}$. Through rigid connections, the motions of nodes B$'$ and C mirror those of nodes 1 and 2, respectively. In general, for a tuning element comprising n components, there are as many as 2^n stable configurations. Figure S2a in the SM, Sec. 2.6 depicts the eight stable configurations of the current three-component tuning element while MM1 illustrates the switching process.

2.3.2 Effective Properties

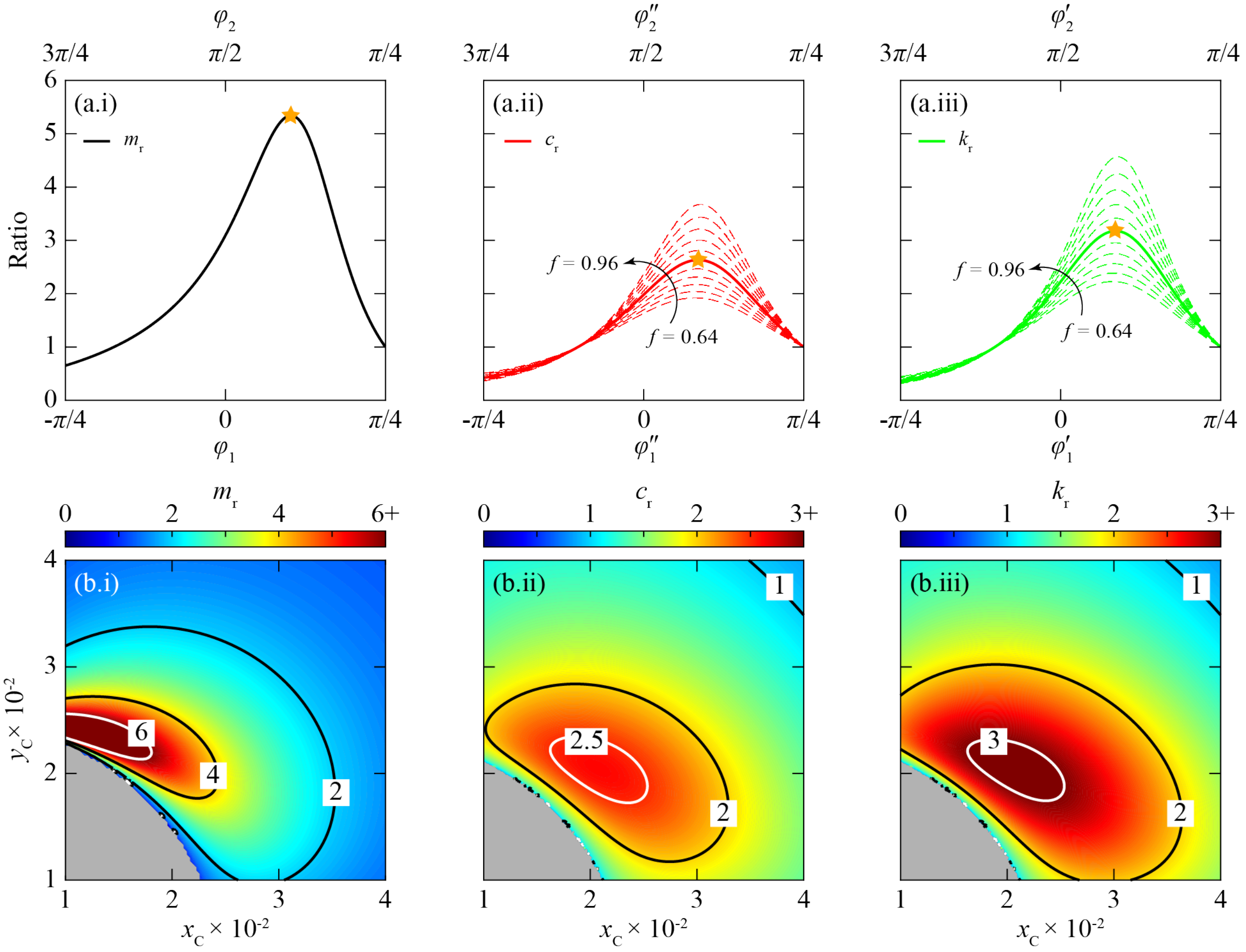

Figure 2.2: Geometric Dependence of Effective Properties. (a) The variation in the effective (i) mass, (ii) damping, and (iii) stiffness ratios as a function of φ_1 for $\bar{L} = 0.12$ and $(x_C, y_C) = (0.02a, 0.02a)$. For k_r and c_r, in particular, the position of B′ along the secondary axis – as specified by the fraction, $f = \bar{\ell}_{B1}/\bar{\ell}_{C1}$ for constant $\bar{\ell}_{C1}$ – presents an additional geometric tuning parameter. For all f, the ratio maxima at occur at $\varphi_1 = \varphi_1' = \varphi_1'' = \pi/10$; the star symbol indicates the maxima for the particular case of $f = 4/5$. (b) The iso-contours of the effective property ratios formed by changing the location of node C while maintaining $\varphi_1 = \varphi_1' = \varphi_1'' = \pi/10$ and $\bar{\ell}_1 = \bar{\ell}_1' = \bar{\ell}_1'' = 0.0717$. The grey shaded regions denote a forbidden geometry, i.e., $\bar{L} < \bar{\ell}_{C1}$ or $|\ell_1 - \ell_2| < \bar{\ell}_{C1}$. The relevant material parameters are: $\bar{m}_a = 1/10$, $\bar{k}_a = 4$, $\bar{c}_a = 3/2$, $\bar{c} = 1/2$.

To characterize the performance of the tuning element, we consider the dynamics of the isolated unit cell in Fig. 2.1d where a mass, $m/2$, is associated with nodes 1 and 2. The relevant equations of motion emerge from the dissipative Euler-Lagrange equation, $(\mathscr{L}_{,\dot{\mathbf{u}}})_{,t} - \mathscr{L}_{,\mathbf{u}} + R_{,\dot{\mathbf{u}}} = \mathbf{0}$, with Lagrangian, $\mathscr{L}(\mathbf{u},\dot{\mathbf{u}})$, and viscous dissipation function, $R(\dot{\mathbf{u}})$. We define the dimensionless displacement and time variables, $\bar{u} = u/a$ and $\bar{t} = \omega_0 t$ where $\omega_0 = \sqrt{k/m}$. Utilizing these definitions and dividing by ka^2, the corresponding non-dimensional kinetic energy, T, deformation energy, V, and incremental energy loss, $\mathrm{d}E = R\mathrm{d}\bar{t}$, are expressed as follows:

$$T = \frac{1}{4}\dot{\bar{u}}_1^2 + \frac{1}{4}\dot{\bar{u}}_2^2 + \frac{1}{2}\bar{m}_\mathrm{a}\dot{\bar{u}}_\mathrm{A}^2 + \frac{1}{2}\bar{m}_\mathrm{a}\dot{\bar{v}}_\mathrm{A}^2, \tag{2.3a}$$

$$V = \frac{1}{2}(\bar{u}_2 - \bar{u}_1)^2 + \frac{1}{2}\bar{k}_\mathrm{a}(\delta\bar{\ell}_\mathrm{AB})^2, \tag{2.3b}$$

$$\mathrm{d}E = \left[\frac{1}{2}\bar{c}(\dot{\bar{u}}_2 - \dot{\bar{u}}_1)^2 + \frac{1}{2}\bar{c}_\mathrm{a}(\delta\dot{\bar{\ell}}_\mathrm{AB})^2\right]\mathrm{d}\bar{t}, \tag{2.3c}$$

where $\bar{m}_\mathrm{a} = m_\mathrm{a}/m$, $\bar{k}_\mathrm{a} = k_\mathrm{a}/k$, $\bar{c} = c/\sqrt{km}$, and $\bar{c}_\mathrm{a} = c_\mathrm{a}/\sqrt{km}$ denote the normalized material parameters; $\delta\bar{\ell}_\mathrm{AB}$ is the change in the length of the line joining nodes A$'$ (or A$''$) and B$'$.

Substituting the definitions from Eq. (2.2) into Eq. (2.3), $\mathscr{L}(\bar{\mathbf{u}},\dot{\bar{\mathbf{u}}})$ and $R(\dot{\bar{\mathbf{u}}})$ become sole functions of the time-dependent boundary displacements, $\bar{\mathbf{u}}^\mathrm{T} = [\bar{u}_1\ \bar{u}_2]$. The dissipative Euler-Lagrange's equation yields the unit cell matrix equations of motion, $\mathbf{M}\ddot{\bar{\mathbf{u}}} + \mathbf{C}\dot{\bar{\mathbf{u}}} + \mathbf{K}\bar{\mathbf{u}} = \mathbf{0}$, where

$$\mathbf{M} = \begin{bmatrix} 1/2 + \bar{m}_\mathrm{a}\sigma_{11} & -\bar{m}_\mathrm{a}\sigma_{12}/2 \\ -\bar{m}_\mathrm{a}\sigma_{21}/2 & 1/2 + \bar{m}_\mathrm{a}\sigma_{22} \end{bmatrix}, \tag{2.4a}$$

$$\mathbf{C} = (\bar{c} + \bar{c}_\mathrm{a}\varepsilon_\mathrm{c}) \begin{bmatrix} 1 & -1 \\ -1 & 1 \end{bmatrix}, \tag{2.4b}$$

$$\mathbf{K} = (1 + \bar{k}_\mathrm{a}\varepsilon_\mathrm{k}) \begin{bmatrix} 1 & -1 \\ -1 & 1 \end{bmatrix}, \tag{2.4c}$$

are the tunable mass, damping, and stiffness matrices, respectively; σ_{ij}, ε_c, and ε_k are configuration-dependent tuning coefficients:

$$\begin{aligned}
&\sigma_{11} = \left[\cos(\varphi_s)\csc(\varphi_s+\theta_s)\right]^2, \\
&\sigma_{12} = \sigma_{21} = 2\cos(\varphi_s)\cos(\theta_s)\csc(\varphi_s+\theta_s)\cot(\varphi_s+\theta_s), \\
&\sigma_{22} = \left[\cos(\theta_s)\csc(\varphi_s+\theta_s)\right]^2, \\
&\varepsilon_\mathrm{c} = \left[\frac{\cos(\alpha_s'') - \sin(\alpha_s'')\cot(\varphi_\mathrm{s}'')}{1+\cot(\varphi_\mathrm{s}'')\tan(\theta_\mathrm{s}'')}\right]^2, \\
&\varepsilon_\mathrm{k} = \left[\frac{\cos(\alpha_s') - \sin(\alpha_s')\cot(\varphi_\mathrm{s}')}{1+\cot(\varphi_\mathrm{s}')\tan(\theta_\mathrm{s}')}\right]^2,
\end{aligned}$$

where α_s' and α_s'' are, respectively, the angles $\bar{k}_\mathrm{a}$ and $\bar{c}_\mathrm{a}$ make with the horizontal (Fig. 2.1d). Specifically, in Eq. (2.4a), notice the off-diagonal entries, termed inertance, coupling the accelerations analogous to spring stiffness and damper viscosity for the displacements and velocities, respectively. Thus, the mass component functions as an inerter, the mechanical element associated with inertance; however, unlike an ideal inerter, it is possible for the mass component to realize an unequal nodal mass distribution (see SM, Sec. 2.6). Recognizing that the isolated unit cell possesses only a single non-zero mode of vibration (i.e., $\bar{\mathbf{u}}^\mathrm{T} = [1 \;\; -1]\bar{u}$) reduces the governing equations to $m_\mathrm{eff}\ddot{\bar{u}} + 4c_\mathrm{eff}\dot{\bar{u}} + 4k_\mathrm{eff}\bar{u} = 0$, where

$$m_\mathrm{eff} = 1 + \bar{m}_\mathrm{a}(\sigma_{11} + \sigma_{22} + \sigma_{12}), \tag{2.5a}$$

$$c_\mathrm{eff} = \bar{c} + \bar{c}_\mathrm{a}\varepsilon_\mathrm{c}, \tag{2.5b}$$

$$k_\mathrm{eff} = 1 + \bar{k}_\mathrm{a}\varepsilon_\mathrm{k}, \tag{2.5c}$$

denote the configuration-dependent element effective mass, damping, and stiffness. Thus, integrated within internal architectures, the multistable tuning element presents the opportunity to tailor the emergent elastodynamic performance post-fabrication via geometric re-configuration, i.e., without the need to add/remove material or to invoke stimuli-response constituents.

As an illustration of the potential disparity in effective properties exhibited by the element's bi-stable components, Fig. 2.2 plots the effective property ratios, $m_\mathrm{r} = m_\mathrm{eff}^{(1)}/m_\mathrm{eff}^{(2)}$, $c_\mathrm{r} = c_\mathrm{eff}^{(1)}/c_\mathrm{eff}^{(2)}$, and $k_\mathrm{r} = k_\mathrm{eff}^{(1)}/k_\mathrm{eff}^{(2)}$ ($\square_\mathrm{eff}^{(s)}$, the configuration-specific value of the effective property) as functions of the geometric design parameters with $\bar{m}_\mathrm{a} = 1/10$, $\bar{k}_\mathrm{a} = 4$, $\bar{c}_\mathrm{a} = 3/2$, and $\bar{c} = 1/2$. In Figs. 2.2a, effective property ratio curves are generated following a parameter study which varies φ_1 (similarly, φ_1' and φ_1'') for a fixed $\bar{L}$ and $(x_\mathrm{C}, y_\mathrm{C})$. The m_r approaches a maximum as $\varphi_1 \to \pi/10$ where, in state $s = 1$, the acceleration amplification at node A achieves its greatest manification compared to that in $s = 2$. Specifically, for a static mass, $m_\mathrm{st} = 1 + \bar{m}_\mathrm{a}$, the maximum corresponds to $m_\mathrm{eff}^{(1)}/m_\mathrm{st} = 5.7$ and $m_\mathrm{eff}^{(2)}/m_\mathrm{st} = 1.07$, indicating a less consequential inertial amplification effect for $s = 2$. In addition, the similar formulation of $\bar{c}_\mathrm{eff}$ and $\bar{k}_\mathrm{eff}$ in combination with the co-location of B' and B'' explains the tandem behavior of c_r and k_r curves. Furthermore, as illustrated by the response to changing $\bar{\ell}_\mathrm{B1}$, the location of B' along the secondary axis acts to scale c_r and k_r. In Figs. 2.2b, the rod lengths remain fixed while φ_s, φ_s', and φ_s'' vary in response to changing the location of node C. In the following, the tuning element is constructed using $(x_\mathrm{C}, y_\mathrm{C}) = (0.02a, 0.02a)$.

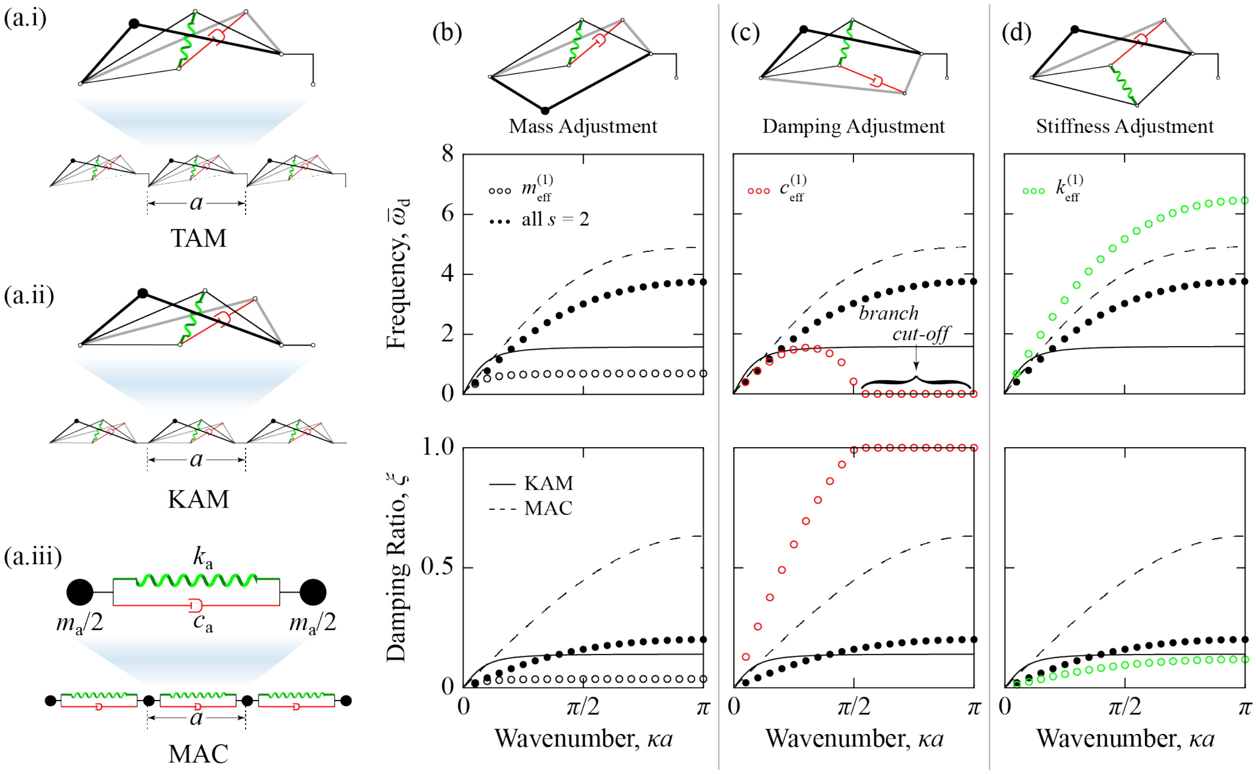

Figure 2.3: Tunable Frequency Band Structure. (a) Three unit cell models identical in composition but distinct in construction: (i) TAM model featuring kinematic amplification, multistability, and offset; (ii) KAM model eschewing the offset of the TAM model and, thus, voiding any tuning capacity due to functionally redundant stable configurations; (iii) MAC model lacking kinematic amplification, multistability, and an offset.(b–d) Configuration-dependent frequency and damping ratio band structures. From all tuning element components in state $s = 2$, selectively switching one component to $s = 1$ amplifies the associated effective property, yielding (b) low-frequency band gaps, (c) branch cut-off, and (d) an increased long-wavelength sound speed. All models utilize the same material parameters: $m_a = 1/10$, $c_a = 1/5$, and $k_a = 1$. For the TAM, the relevant geometric are: $\varphi_1 = \pi/10$, $\varphi'_1 = \pi/5$, $\varphi''_1 = \pi/6$, $\bar{\ell}_1 = 0.0717$, $\bar{\ell}'_1 = 0.0739$, $\bar{\ell}''_1 = 0.0734$, $\bar{L} = 0.12$, and $f = 1.3$. The KAM utilizes the same geometry as the TAM, except the corresponding φ_1, φ'_1, and φ''_1 are each reduced by $\pi/4$ since the primary and secondary axes are aligned.

2.4 Dynamic Analysis

In the following, we investigate the adjustable (linear) dynamic response of a lattice material incorporating the multistable element. To this end, for an analytical treatment, we apply the free-wave formulation of Bloch theorem described by Hussein and Frazier[109] which accommodates temporal attenuation in wave amplitude. This section briefly describes the formulation and interpretation of results.

For the unit cell of a viscously-damped, periodic medium, $\mathbf{M}\ddot{\bar{\mathbf{u}}}+\mathbf{C}\dot{\bar{\mathbf{u}}}+\mathbf{K}\bar{\mathbf{u}}=\mathbf{f}$ represents the discretized equations of motion with $\mathbf{f}$ collecting the forces applied at the unit cell boundaries by its immediate neighbors. Due to the spatial periodicity of the wave solution, the motion of a point separated by lattice vector, $\mathbf{a}$, from a reference exhibits a phase shift, i.e., $\bar{\mathbf{u}}[\boldsymbol{\kappa}\cdot(\mathbf{x}+\mathbf{a}),\bar{t}] = \bar{\mathbf{u}}(\mathbf{x},\bar{t})\mathrm{e}^{\mathrm{i}\boldsymbol{\kappa}\cdot\mathbf{a}}$ with wavevector, $\boldsymbol{\kappa}$. Consequently, one may write, $\bar{\mathbf{u}}=\mathbf{T}\bar{\mathbf{u}}_{\mathrm{e}}$, equating the full set of degrees of freedom to the product of a wavevector-dependent transformation matrix, $\mathbf{T}$, and a subset of essential freedoms, $\bar{\mathbf{u}}_{\mathrm{e}}$. Thus, in terms of $\bar{\mathbf{u}}_{\mathrm{e}}$, the lattice material governing equations are $\mathbf{M}_{\mathrm{e}}\ddot{\bar{\mathbf{u}}}_{\mathrm{e}}+\mathbf{C}_{\mathrm{e}}\dot{\bar{\mathbf{u}}}_{\mathrm{e}}+\mathbf{K}_{\mathrm{e}}\bar{\mathbf{u}}_{\mathrm{e}}=\mathbf{0}$ where $\mathbf{M}_{\mathrm{e}}=\mathbf{T}^{\mathrm{H}}\mathbf{M}\mathbf{T}$, $\mathbf{C}_{\mathrm{e}}=\mathbf{T}^{\mathrm{H}}\mathbf{C}\mathbf{T}$, and $\mathbf{K}_{\mathrm{e}}=\mathbf{T}^{\mathrm{H}}\mathbf{K}\mathbf{T}$ with $\square^{\mathrm{H}}$ denoting the Hermitian transpose. $\mathbf{T}^{\mathrm{H}}\mathbf{f}=\mathbf{0}$ maintains that boundary forces do no work.

Following the free-wave formulation, $\bar{\mathbf{u}}_{\mathrm{e}}(\bar{t})=\tilde{\mathbf{u}}_{\mathrm{e}}\mathrm{e}^{\bar{\lambda}\bar{t}}$, where $\bar{\lambda}$ is a complex frequency. Applying the time derivatives develops a quadratic eigenvalue problem in $\bar{\lambda}$. Alternatively, the governing equation can be recast in the state-space form, $\mathbf{A}\dot{\bar{\mathbf{y}}}+\mathbf{B}\bar{\mathbf{y}}=\mathbf{0}$, where

$$\mathbf{A}=\begin{bmatrix}\mathbf{0} & \mathbf{M}_{\mathrm{e}}\\ \mathbf{M}_{\mathrm{e}} & \mathbf{C}_{\mathrm{e}}\end{bmatrix},\quad \mathbf{B}=\begin{bmatrix}-\mathbf{M}_{\mathrm{e}} & \mathbf{0}\\ \mathbf{0} & \mathbf{K}_{\mathrm{e}}\end{bmatrix},\quad \bar{\mathbf{y}}=\begin{bmatrix}\dot{\bar{\mathbf{u}}}_{\mathrm{e}}\\ \bar{\mathbf{u}}_{\mathrm{e}}\end{bmatrix}.$$

Assuming the solution, $\bar{\mathbf{y}}(\bar{t})=\tilde{\mathbf{y}}\mathrm{e}^{\bar{\eta}\bar{t}}$, formulates the standard eigenvalue problem in complex frequency, $\bar{\eta}$. The solutions appear in conjugate pairs of the form, $\bar{\eta}=-\xi\bar{\omega}_{\mathrm{res}}\pm\mathrm{i}\bar{\omega}_{\mathrm{d}}$, where $\bar{\omega}_{\mathrm{res}}$ is the resonant frequency, $\bar{\omega}_{\mathrm{d}}=\mathrm{Im}[\bar{\eta}]$ the damped natural frequency, and $\xi=-\mathrm{Re}[\bar{\eta}]/\mathrm{Abs}[\bar{\eta}]$ the damping ratio.

In the Sec. 2.5, we apply the free wave Bloch analysis to obtain dispersion results for both 1D and 2D systems. In particular, for the 2D system in Sec. 2.5.2, we complement the Bloch analysis with a simulation of a finite 2D structure (Fig. 2.5c) for which the non-linear terms associated with the kinematic amplification mechanisms (see SM, Sec. 2.6) in the governing equations are maintained but whose effects are negligible due to the small-amplitude motion that is stimulated.

2.5 Results and Discussion

2.5.1 1D Tunable Architected Material

To demonstrate the tuning ability afforded by the multistable element, we first consider the dispersion of the one-dimensional tunable architected material (TAM) defined by the unit cell in Fig. 2.3a.i. Following the application of Bloch theorem, the state-space determinantal equation is found to be:

$$\begin{aligned}\bar{\eta}^2(m_{\text{eff}} - \sigma_{12}[1+\cos(\kappa a)]\bar{m}_{\text{a}})\\ +4\sin^2\left(\frac{\kappa a}{2}\right)(\bar{\eta}c_{\text{eff}} + k_{\text{eff}}) = 0,\end{aligned}$$

which the presence of m_{eff}, c_{eff}, and k_{eff} renders configuration-specific, an attribute extending to $\bar{\omega}_{\text{d}}$ and ξ (see SM, Sec. 2.6). We also consider the dynamics of the kinematic amplification material (KAM) defined by the unit cell in Fig. 2.3a.ii which is identical to that in Fig. 2.3a.i except for the lack of an offset (i.e., the primary and secondary axes are aligned); it retains the multistable and kinematic amplification properties. Nevertheless, due to the symmetry of the stable states in the absence of an offset, multistability does not entail tunability and, thus, this characteristic holds no significance for the KAM model. We also consider the dynamics of the mono-atomic chain (MAC) defined by the unit cell in Fig. 2.3a.iii which represents a simple mass-spring-damper system lacking multistability and kinematic amplification, and for which an offset would be of little significance. Notice that, except for the massless rigid rods, each of the unit cells in Fig. 2.3 emerges from the same building blocks. The m, c, and k parameters are omitted from all models to highlight alone the effect of m_a, c_a, and k_a. In order to maintain a concise presentation, the matrices $\mathbf{M}$, $\mathbf{C}$, $\mathbf{K}$, and $\mathbf{T}$ corresponding to each of the models are provided in the SM, Sec. 2.6.

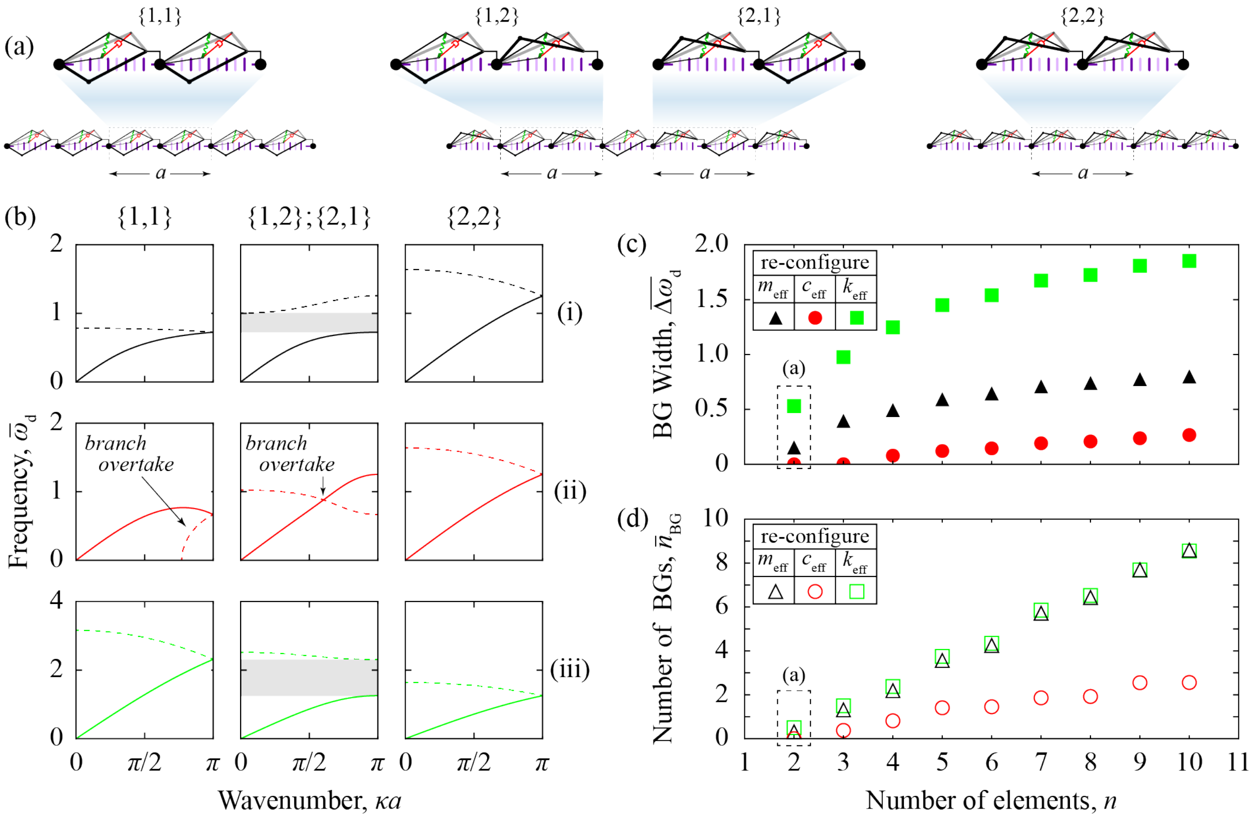

Figure 2.4: Band Gap Evolution (color online). (a) Architected material with unit cell consisting of $n = 2$ copies of the tuning element in series. Each element in the series can be tuned independently. Here, mass tuning is depicted as the configuration, $\{s, s\}$, of the two constituent tuning elements of the unit cell is altered. Apparently, $\{1, 2\} \equiv \{2, 1\}$ as the architected materials constructed from either of these unit cell configurations are identical. (b) The frequency diagram (band gaps shaded) depicting the acoustic (solid) and optical (dashed) branch of 1D architected material defined by a two-element unit cell where the configuration, $\{s, s\}$, of the constituent (i) mass, (ii) damping, or (iii) stiffness components is altered while that of the other two property components is uniformly $s = 2$. (c) The average band-gap width, $\overline{\Delta\omega}_\mathrm{d}$ (solid), and (d) the average number of band gaps, $\bar{n}_\mathrm{BG}$ (hollow), among all (i) m_eff (black), (ii) c_eff (red), and (iii) k_eff (green) configurations of a n-element unit cell. The relevant material/geometric parameters are denoted by the ⋆ symbol in Fig. 2.2a.

Figures 2.3b–d display the dispersion response of each model, in particular, for the TAM and KAM models, as each component is activated in turn. For clarity, of the eight possible configurations each for the TAM and KAM, we highlight only four: the case in which all components are in state $s = 2$, therefore, minimizing the affect of kinematic amplification; and the three cases in which a designated component is singularly in state $s = 1$.

In Fig. 2.3b, switching only the effective mass component to configuration $s = 1$ brings a near thirty-fold increase in m_{eff}, leading to a decrease in the maximum frequency and damping ratio while the sound speed remains unaffected.[68] Similarly, in Fig. 2.3c, switching only the effective damping component to configuration $s = 1$ leads to a six-fold increase in c_{eff}, decreasing the maximum frequency and increasing the damping ratio while maintaining the sound speed. In addition, we also observe *branch cut-off*, the condition whereby $\bar{\omega}_{\text{d}} = 0$ over a portion of the Brillouin zone due to a corresponding $\xi \geq 1$ (i.e., overdamping); thus, opening gaps in the wavenumber range.[109] Notice that, while adjusting the effective mass or damping, the long-wavelength sound speed, $c_0 = \sqrt{k_{\text{eff}}/m_{\text{st}}} = 2.534$, remains constant as as k_{eff} is unchanged and the relative motion between nodes 1 and 2 becomes vanishingly small and, thus, reduces the motion at node A (equiv. A$'$, A$''$) and the influence of amplification on the dispersion. In Fig. 2.3d, switching only the effective stiffness component to configuration $s = 1$ triples k_{eff}, leading to an increase in the maximum frequency and sound speed while the damping ratio decreases. The frequency and damping ratio shifts observed in Figs. 2.3b–d can be understood by relating the wave dispersion results at the boundary of the irreducible Brillouin zone ($\kappa a = \pi$) to the vibration of an isolated unit cell for which $\bar{\omega}_{\text{d}} = \sqrt{4k_{\text{eff}}(1-\xi^2)/m_{\text{eff}}}$ and $\xi = c_{\text{eff}}/\sqrt{k_{\text{eff}} m_{\text{eff}}}$.

For the TAM, the scenarios depicted in Figs. 2.3b–d demonstrate the phenomenon of *metadamping*, a reduction (*negative*)[109] or amplification (*positive*)[25] of dissipative power between two statically equivalent configurations (i.e., identically prescribed mass, damping, effective stiffness). If the configuration with all components in state $s = 2$ is selected as the reference, then switching either the mass or stiffness component to state $s = 1$ decreases the mean damping ratio, $\xi_{\text{avg}} = \pi^{-1}\int_0^{\pi} \xi \, \text{d}(\kappa a)$, relative to the reference (negative metadamping), while switching only the damping component to state $s = 1$ increases ξ_{avg} compared to the reference (positive metadamping). Naturally, the opposite is true if the configuration with all components in state $s = 1$ is the reference and components individually switched to state $s = 2$. As evidenced by recent works,[47,110,111] the metadamping phenomenon continues to attract research attention. In particular, Al Babaa *et al.*[47] actively tuned the metadamping response of an electro-mechanical system exploiting kinematic amplification and piezoelectric shunting circuits.

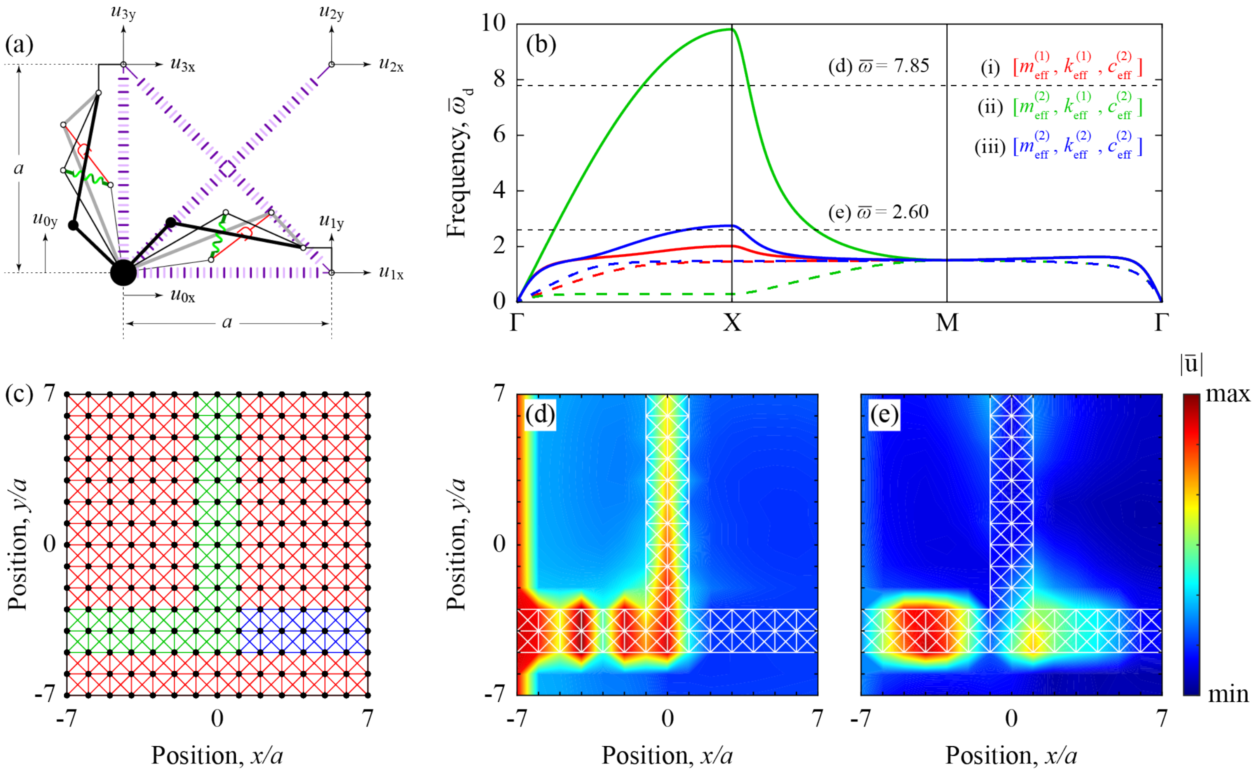

Figure 2.5: Customizable Waveguide (color online). (a) The 2D tunable architected material unit cell with nearest- and next-nearest neighbor connections, and a tuning element oriented along both the horizontal and vertical axis. (b) Homogeneous dispersion curves [*sans* $\xi(\boldsymbol{\kappa})$] for three tuning element configurations with constant $c_{\text{eff}}^{(2)}$: (i) $m_{\text{eff}}^{(1)}$ and $k_{\text{eff}}^{(1)}$ (red), (ii) $m_{\text{eff}}^{(2)}$ and $k_{\text{eff}}^{(1)}$ (green), and (iii) $m_{\text{eff}}^{(2)}$ and $k_{\text{eff}}^{(2)}$ (blue). (c) System of 14×14 unit cells with tuning elements configured to establish a waveguide in the non-uniform distribution of effective properties. In simulation, a sinusoidal displacement, $\bar{u}_x = (5 \times 10^{-5}) \sin(\bar{\varpi}\bar{t})$ for $\bar{t} \in [0, 50]$, is prescribed at the left boundary with frequency (d) $\bar{\varpi} = 7.85$ and (e) $\bar{\varpi} = 2.60$. Subfigures (d,e) plot the observed time-average magnitude of the displacement, $|\bar{\mathbf{u}}|$. The relevant material/geometric parameters are: $\bar{m}_a = 1/10$, $\bar{k}_a = 4$, $\bar{c}_a = 3/200$, $\bar{c} = 1/200$, $\varphi_1 = \varphi_1' = \varphi_1'' = 0.03\pi$, $\bar{\ell}_1 = \bar{\ell}_1' = \bar{\ell}_1'' = 0.2105$, $\bar{L} = 0.4$, $f = -4$.

Since each bi-stable component can be independently configured (see MM2 for demonstration of 3D-printed toy model), the spatial distribution of effective properties as well as the emerging dynamic response are extremely customizable. Consider, now, a 1D architected material unit cell consisting of a chain of n copies of the tuning element which, in total, supports 2^{3n} configurations; however, due to equivalent dynamics among certain configurations, realizes a lesser number of unique dispersion responses. The n-element unit cell permits a non-uniform property distribution conducive to the formation of finite band gaps as exemplified by the results in Fig. 2.4b for $n = 2$ which are based on the model in Fig. 2.1d with geometry and effective properties corresponding to that marked by the $\star$ symbol in Fig. 2.2a which yields $m_{\text{eff}}^{(1)} = 6.28$, $m_{\text{eff}}^{(2)} = 1.18$, $c_{\text{eff}}^{(1)} = 1.31$, $c_{\text{eff}}^{(2)} = 0.5$, $k_{\text{eff}}^{(1)} = 3.15$, and $k_{\text{eff}}^{(2)} = 1$. In addition, we observe *branch overtaking* – the scenario whereby damping leads to higher modes occupying a frequency range below lower ones – between the acoustic and optical modes.[109] Figure 2.4c tracks the average band-gap width, $\overline{\Delta\omega}_{\text{d}}$, and Fig. 2.4d the average number of band gaps, $\bar{n}_{\text{BG}}$ for a n-element system (i) of uniform $k_{\text{eff}}^{(2)}$ and $c_{\text{eff}}^{(2)}$, and the 2^n configurations of m_{eff}, (ii) of uniform $m_{\text{eff}}^{(2)}$ and $k_{\text{eff}}^{(2)}$, and the 2^n configurations of c_{eff} and (iii) of uniform $m_{\text{eff}}^{(2)}$ and $c_{\text{eff}}^{(2)}$, and the 2^n configurations of k_{eff}. As n increases, each scenario exhibits a monotonic increase in $\overline{\Delta\omega}_{\text{d}}$ which, nevertheless, appears to asymptotically approach a limiting value. Further inspection of the band structures reveals that this result reflects the tendency of unit cell morphologies to broaden band gaps at higher frequencies while gaps at lower frequencies either shrink or close. Moreover, although a n-element system may exhibit up to $n-1$ band gaps, due to the band-gap closures that manifest for certain configurations, Fig. 2.4d shows $\bar{n}_{\text{BG}} \leq n-1$. The band gaps tend to be wider when varying the stiffness, followed by the inertial and damping induced band gaps, consistent with the nature of dependency of $\bar{\omega}_{\text{d}}$ on the specific properties. Compared to the variable m_{eff} and k_{eff} distribution scenarios, the case of variable c_{eff} distribution sees lower $\overline{\Delta\omega}_{\text{d}}$ and $\bar{n}_{\text{BG}}$ owing to annihilation of band gaps by the unique conditions of branch overtaking and overdamping.[109]

2.5.2 2D Tunable Architected Material

Figure 2.5a shows the unit cell of a square lattice incorporating the multistable element along both its horizontal and vertical edges. For small-amplitude displacements, the corresponding matrices **M**, **C**, **K**, and **T** are provided in the SM, Sec. 2.6. Different from the tuning element used to generate Fig. 2.4, in the following studies, $\bar{L} = 0.4$, $\varphi_1 = \varphi_1' = \varphi_1'' = 0.03\pi$, and $\bar{\ell}_{\mathrm{B1}}/\bar{\ell}_{\mathrm{C1}} = -4$, yielding effective property ratios of $m_{\mathrm{r}} = 31$ and $k_{\mathrm{r}} = 26$. Although $c_{\mathrm{r}} = 19$, in preparation for the subsequent simulations, the attenuation experienced by propagating waves is significantly reduced by keeping the damping small with $\bar{c} = 1/200$ and $\bar{c}_{\mathrm{a}} = 3/200$. Apparently, setting the tuning element along each axis to different configurations generates an anisotropic response[104, 112, 113] in one or more of the effective properties which may assist the realization of tunable directional behavior. Nevertheless, following the procedure outlined in Sec. 2.4, we determine the two-dimensional dispersion relations, for three cases for which $c_{\mathrm{eff}}^{(2)}$ and the tuning elements along each axis are in identical states: (i) $m_{\mathrm{eff}}^{(1)}$ and $k_{\mathrm{eff}}^{(1)}$, (ii) $m_{\mathrm{eff}}^{(2)}$ and $k_{\mathrm{eff}}^{(1)}$, and (iii) $m_{\mathrm{eff}}^{(2)}$ and $k_{\mathrm{eff}}^{(2)}$. Figure 2.5b reflects the dynamics of each of these unit cell configurations, the longitudinal mode (solid) displaying behavior reminiscent of that exhibited by the 1D system.

In order to support the analytical dispersion results as well as to demonstrate the tuning element as a mechanism for realizing functionality, we simulate the dynamic response of a 14×14 square lattice (using the Noh-Bathe scheme[114]) for which, of the myriad available morphologies, the particular spatial distribution of three unit cell configurations and corresponding effective properties is set in the form of a waveguide (Fig. 2.5c). We prescribe a small-amplitude, sinusoidal displacement at the left boundary and depict the response in Figs. 2.5d,e. The dispersion curves (Fig. 2.5b) for systems homogeneously in each of the three configurations aid in selecting the excitation frequencies which stimulate waves capable of propagating within one or more regions of the waveguide. For an excitation frequency $\bar{\omega} = 7.85$ (Fig. 2.5d), waves propagate along the channel defined by unit cells with tuning elements in configuration (ii) and, otherwise, decay since the excitation frequency falls within a semi-infinite band gap of regions in configuration (i) or (iii). Alternately, for an excitation frequency $\bar{\omega} = 2.60$, the bulk of the wave energy is directed from the horizontal portion of channel of configuration (ii) into the horizontal channel of configuration (iii) (Fig. 2.5e). Apparently, although wave propagation is supported in the vertical portion of channel (ii), since waves are no longer barred from entering channel (iii), little wave energy is re-directed into the vertical column. The waveguide is just one functionality realizable post-fabrication in lattices leveraging the tuning element for effective property re-distribution.

2.6 Conclusion

In this article, we present a novel structural element which leverages geometric multistability and kinematic amplification to independently adjust its effective mass, stiffness, and viscous damping properties with consequences for the dynamic response of architected lattice materials for which it is a part of the unit cell design. This is significant since, despite the well-established impact of all three properties in mechanical vibration and wave propagation, alternative approaches typically manipulate a single parameter. In addition, the specific implementation of multistability in the proposed structural element ensures that re-configuration does not entail a change in length and, therefore, does not necessitate a change in the size/shape of the realized lattice structure, a beneficial quality in practical settings where the structure is subject to geometric constraints.

To demonstrate the tuning ability granted by the multistable element, we analytically and numerically investigate the adjustable dynamic characteristics of 1D/2D tunable architected material models for which it appears as a part of the unit cell. It is shown that the band structure depends on the specific configurations of the multistable element: the sound speed, the frequency range(s) of propagation, and the propagation modality (e.g., underdamped or overdamped) are each amenable to manipulation. Moreover, in organizing the spatial distribution of the element states, custom and re-definable mesoscopic morphologies of the effective properties are attainable with the potential for functionalization (e.g., the impromptu formation of a waveguide).

The proposed concept offers a new way to expand the performance space of lattice materials post-fabrication. In addition, as a product of geometry rather than, e.g., specific material constituents or external apparatuses, the proposed technique grants flexibility in implementation, and is amenable to current and emerging additive manufacturing technologies.

Acknowledgements

This work is supported by start-up funds provided by the University of California.

Supplementary Material

See Supplementary Material[1] for additional results, detailed derivations and calculation procedures.

---

[1] `https://www.scitation.org/doi/suppl/10.1121/10.0017346`

Declaration

Chapter 2, in full, is a reprint of the material as it appears in V. Ramakrishnan and M. J. Frazier, “Architected material with independently tunable mass, damping, and stiffness via multi-stability and kinematic amplification”, *J. Acoust. Soc. Am.*, **vol. 153**, **no. 2**, pp. 1283-1292, February 2023. The dissertation author is the primary author of this paper.

Chapter 3

Multistable Metamaterial on Elastic Foundation Enables Tunable Morphology for Elastic Wave Control

This chapter is published in:

Journal of Applied Physics, **127**, 225104 (2020)

DOI: 10.1063/1.5145324

3.1 Abstract

We present a strategy for continuously and reversibly tuning the propagation of elastic waves in one-dimensional systems without need for persistent external stimulation. The general approach places a bistable metamaterial on an elastic substrate which is subsequently deformed via

prescribed boundary displacements. The internal substrate deformation, which is shaped by a prescribed spatial variation in elasticity, is reflected in the overlaying metamaterial and facilitates the reconfiguration of bistable elements over isolated regions. As each configuration is associated with a unique stiffness, these regions represent an adjustable, mesoscale morphology amenable to tuning elastic waves. The essential bistability is characterized by an asymmetric, double-welled equipotential energy function and is developed by mechanical rather than phenomenological means. The asymmetry provides for the unique, configuration-specific (stable) equilibrium stiffnesses; the equipotential promotes reversibility (i.e., no one configuration is energetically preferred). From a uniform metamaterial-substrate system, we demonstrate the utility of our strategy by producing a waveguide with shifting pass band and a metamaterial with variable unit cell morphology.

3.2 Introduction

Architected metamaterials[57,82,115] are remarkable for their extraordinary thermal,[18–20] mechanical,[7–9] acoustic,[10–15] and optical[16,17] performance stemming from a cleverly designed internal architecture, comprising both a characteristic (often periodic) structural geometry and constituent material morphology – in a sense, representing the emancipation of material behavior from the limitations of chemistry. In particular, research pertaining to elastic wave propagation has realized extreme/counter-intuitive effective properties[6,8] that bring once fantastic applications into practical reach.[116–119] In addition, illustrating a broad range of applicable scales, new strategies for, e.g., thermal management,[120,121] signal processing,[122] acoustic sensing,[123] energy harvesting,[37,124,125] and earthquake mitigation[126,127] have also been proposed.

However, utilizing “stiff” material constituents in the metamaterial construction leaves little opportunity to adapt the dynamic performance for scenarios where the target frequency range may fluctuate significantly (e.g., as in environmental vibration mitigation and energy harvesting applications), thus limiting effectiveness outside a fixed service range. One remedy is the class of active architectures which leverage shunted piezoelectric elements[43, 45, 46, 97, 128, 129] to adjust the effective stiffness via electro-mechanical coupling, thus tuning the native dispersion characteristics of the metamaterial. Nevertheless, it is conceivable that for certain metamaterial applications, obviating the need for the accompanying complex wiring and external controllers is desirable. Serving to accommodate this requirement, a second approach toward inherently tunable performance utilizes soft material constituents for which deforming the internal architecture modifies the effective stiffness and, consequently, the characteristic wave dispersion. By exploiting instability and multistability in readily re-configurable soft architectures, efforts to imbue metamaterials with an inherent tuning capability, generally, effect one of two outcomes: (i) the tuning is continuous and reversible, though the tuned configurations are reliant on the constant support of an external field or prescribed boundary condition[39, 49, 50, 90, 130–133] or (ii) the tuning is among a finite number of discrete, stable configurations, though the process is energetically fated to follow an energy-minimizing sequence,[2, 58, 69, 101–103, 134] prohibiting restoration to an earlier configuration; thus, tuning is irreversible and, ultimately, terminated. Continuous tuning allows for small adjustments; reversible tuning facilitates repeated adjustments; and stable tuning eliminates the need for an ever-present supporting field or boundary condition. Xia *et al.*[135] demonstrated these tuning abilities in a silicon-coated microlattice utilizing an electro-chemical reaction. A metamaterial system possessing a inherent tuning capability independent of chemistry and external controllers which permits continuous, reversible, and stable adjustments to the dispersion characteristics [i.e., combining the desirable attributes of outcomes (i) and (ii)] is appealing and the aim of the present work.

In this article, we propose a class of architected metamaterial utilizing a modified bistable element described in earlier works[61,136] as a mechanical analogue of a buckled axial member, minus the instability, whose effective stiffness as well as its distribution is continuously, stably, and reversibly adjustable for adaptive dynamic performance using the technique of strain engineering. The general strategy couples a soft, multistable metamaterial to a relatively stiff (though deformable) foundation which, when strained, assists in reconfiguring the multistable architecture, modifying the metamaterial performance. A similar approach has been explored in the context of controllable electronic and photonic performance in thin-film materials.[137,138] Following this strategy, the strain state in the elastic substrate is reflected in the overlaying metamaterial, causing isolated regions to switch to the opposing configuration characterized by a unique effective stiffness, i.e., one that is acoustically distinct to the propagating wave. Moreover, dependent upon the strain magnitude, the size of the switched regions are customizable, enabling a post-fabrication redistribution of the stiffness property. This redistribution of a mechanical property, achieved without an external controller or appeal to chemistry, adds a second dimension to the tuning operation and is unique to the relevant literature. As the non-convex potential energy landscape is not biased toward a particular configuration, the tuned stiffness patterning in the re-configured metamaterial is stable (permitting quasi-static removal of the instigating boundary displacements) and potentially reversible (requiring the same effort to elicit and reverse the tuned state). In one dimension, we introduce and analyze two such metamaterial systems. While the multistability is localized in one system, it is interactive in another which affects reversibility. In addition, continuous tuning, i.e., that permitting small adjustments in configuration, is demonstrated. Our approach will be applied to the establishment of waveguides with shifting transparency and metamaterial unit cells with tunable (stiffness) morphology.

The remainder of the article is organized as follows: Section 3.3 presents simple realizations of our strategy in the form of mass-spring systems, including a qualitative and analytical description of the energetic and dispersion characteristics. In Section 3.4, we analyze and discuss the results of numerical simulations illustrating the tunable wave filtering properties. We demonstrate the concept in the form of (1) a waveguide with an adjustable pass band and (2) a metamaterial with a variable unit cell (stiffness) morphology. Finally, in Sec. 3.5, we draw insights from the numerical results and suggest avenues for further study.

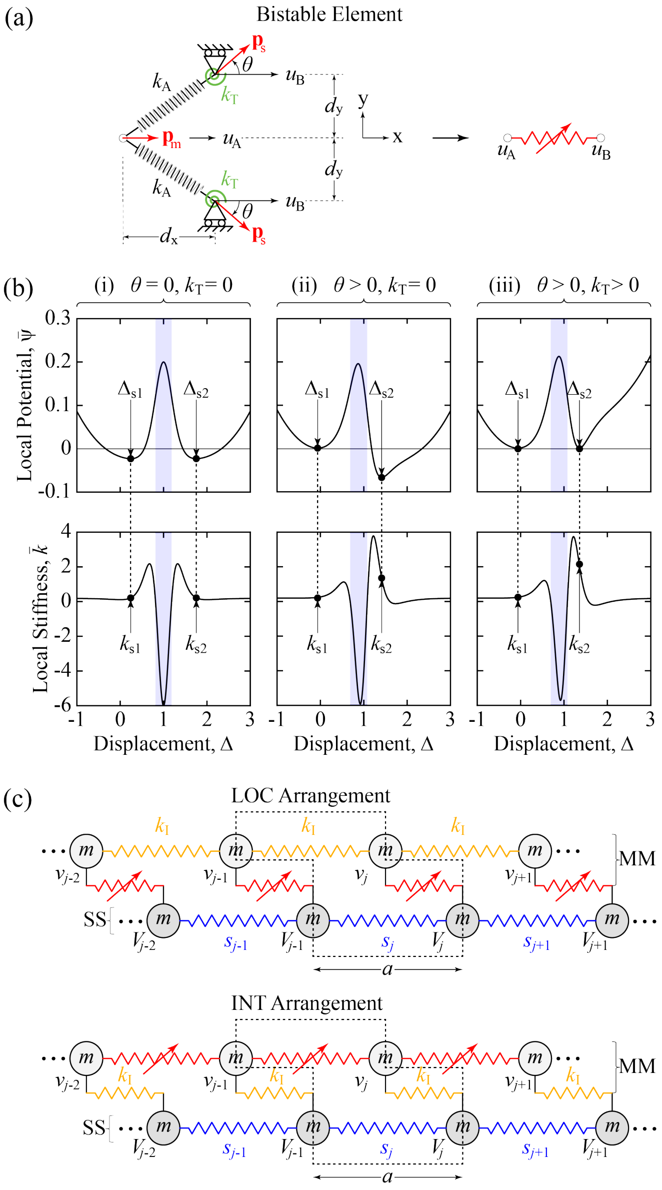

Figure 3.1: (Color online). Bistable Metamaterial on Elastic Foundation. (a) The essential bistable element of the metamaterial-substrate systems. (b) The non-convex energy function is adjusted by the geometric and material parameters to yield an asymmetric, equipotential profile. The asymmetry is reflected in the corresponding stiffness function, resulting in a unique stiffness, $k = \{k_{s1}, k_{s2}\}$, for each of the two equilibrium configurations, $\Delta = \{\Delta_{s1}, \Delta_{s2}\}$. The shaded region identifies the negative stiffness region. (c) Two metamaterial-substrate (MM-SS) arrangements with lattice constant, a: one in which the bistable element is local (LOC) to each metamaterial degree-of-freedom; another in which the bistable element couples two metamaterial degrees-of-freedom (INT). For compact display, the bistable element is represented as a nonlinear spring which is indicated by an arrow.

3.3 Model Description

3.3.1 The Asymmetric, Equipotential Function

Figure 3.1a illustrates the basic structural element giving rise to the metamaterial multistability, representing an elaborated conception of the bistable unit found in related works.[101, 136] In part, the bistable element comprises two identical, pin-connected axial springs, k_A, arranged symmetrically about and at an angle to the x-axis as illustrated. This construction ensures that, as the pinned end displaces, u_A, the combined reaction from the axial springs is always parallel to the displacement. A notable distinction with earlier works, the remote ends of each spring are not fixed, but may displace, u_B, along the horizontal axis. Given the relative displacement, $\Delta = (u_\mathrm{A} - u_\mathrm{B})/d_\mathrm{x}$, the corresponding non-convex potential function, $\psi_\mathrm{A}(\Delta)$, is symmetric about the unstable equilibrium configuration, $\Delta = 1$. In addition to $\psi_\mathrm{A}(\Delta)$, the total bistable energy has contributions from an elastic potential, $\psi_\mathrm{T}(\Delta)$, originating from a pair of torsional springs, k_T, at the remote ends of each k_A, and a magnetic potential, $\psi_\mathrm{M}(\Delta)$, stemming from the interaction between a horizontally-aligned magnetic dipole moment, $\mathbf{p}_\mathrm{m}$, affixed to pinned end and a pair of dipole moments, $\mathbf{p}_\mathrm{s}$, collocated with the torsional springs and oriented an angle, θ, with respect to the x-axis (see Fig. 3.1a). Together, these contributions foster the crucial asymmetric equipotential necessary for stable, reversible tuning. Specifically, the total bistable potential becomes

$$\psi(\Delta) = \psi_\mathrm{A}(\Delta) + \psi_\mathrm{M}(\Delta) + \psi_\mathrm{T}(\Delta), \tag{3.1}$$

where the full equations for each component is given in the Appendix. The corresponding stiffness function is given as $k(\Delta) = \partial^2\psi/\partial\Delta^2$. The two stable equilibrium configurations, $\Delta = \{\Delta_{\mathrm{s1}}, \Delta_{\mathrm{s2}}\}$ ($\Delta_{\mathrm{s1}} < \Delta_{\mathrm{s2}}$), are characterized by stiffnesses $k = \{k_{\mathrm{s1}}, k_{\mathrm{s2}}\}$.

Figure 3.1b illustrates the effect of each component in Eq. (3.1) on the shape of the bistable energy landscape and stiffness function. While $k_{\mathrm{T}} = 0$ and the dipole moments $\mathbf{p}_{\mathrm{s}}$ are oriented such that $\theta = 0$, the bistable potential is symmetric [Fig. 3.1b.(i)]; consequently, $k_{\mathrm{s1}} = k_{\mathrm{s2}}$. Changing either of these conditions alone, generally, biases the energy landscape toward a specific equilibrium configuration [Fig. 3.1b.(ii)] and hinders reversible tuning; however, a suitable choice of k_{T} and $\mathbf{p}_{\mathrm{s}}$ will produce an asymmetric, equipotential landscape with $k_{\mathrm{s1}} \neq k_{\mathrm{s2}}$ [Fig. 3.1b.(iii)].

3.3.2 The Governing Equations and Homogeneous Dispersion Relations

Two metamaterial-substrate arrangements are considered, distinguished by the placement of the bistable element within the unit cell of an N-cell chain (schematically represented as a nonlinear spring in Fig. 3.1c). In one arrangement (LOC), the bistable element couples the local metamaterial and substrate degrees-of-freedom, i.e., $\{u_{\mathrm{A}}, u_{\mathrm{B}}\} \to \{v_j, V_j\}$; in another (INT), the bistable element links nearest neighbors in the overlaying metamaterial, i.e., $\{u_{\mathrm{A}}, u_{\mathrm{B}}\} \to \{v_{j-1}, v_j\}$. In the preceding statement, the right arrow maps the displacements of the bistable element, u_{A} and u_{B} (Fig. 3.1a), to those of the metamaterial layer, v, and substrate layer, V (Fig. 3.1c). The substrate features springs of variable stiffness, s_j, joining neighboring degrees-of-freedom. The variability enables an inhomogeneous strain. In addition, each arrangement features springs, k_{I}, which are interactive in the LOC arrangement and local in the INT arrangement.

Dimensionless governing equations will enable the investigation of the dynamics without reference to explicit geometric and material parameters. For this reason, displacements, position, and time are scaled by suitable quantities:

$$\bar{v} = v/d_{\mathrm{x}}, \quad \bar{V} = V/d_{\mathrm{x}}, \quad \bar{x} = x/a, \quad \bar{t} = \omega_0 t,$$

where $\omega_0^2 = k_{\mathrm{I}}/m$. In addition, $k_{\mathrm{I}}d_{\mathrm{x}}^2$ defines a convenient unit of energy. Thus, for a chain of N unit cells, the dimensionless Lagrangian is

$$\begin{aligned} \mathscr{L}^{\mathrm{LOC}} =& \sum_{j=1}^{N} \left[\frac{1}{2}(\dot{\bar{v}}_j^2 + \dot{\bar{V}}_j^2) - \bar{\psi}(\bar{V}_j, \bar{v}_j) \right] \\ & - \frac{1}{2} \sum_{j=2}^{N} \left[\bar{s}_j(\bar{V}_j - \bar{V}_{j-1})^2 + (\bar{v}_j - \bar{v}_{j-1})^2 \right], \end{aligned} \tag{3.2a}$$

$$\begin{aligned} \mathscr{L}^{\mathrm{INT}} =& \frac{1}{2} \sum_{j=1}^{N} \left[\dot{\bar{v}}_j^2 + \dot{\bar{V}}_j^2 - (\bar{v}_j - \bar{V}_j)^2 \right] \\ & - \sum_{j=2}^{N} \left[\frac{\bar{s}_j}{2}(\bar{V}_j - \bar{V}_{j-1})^2 + \bar{\psi}(\bar{v}_j, \bar{v}_{j-1}) \right], \end{aligned} \tag{3.2b}$$

where $\bar{s}_j = s_j/k_{\mathrm{I}}$ is the normalized local substrate stiffness and $\bar{\psi} = \psi/k_{\mathrm{I}}d_{\mathrm{x}}^2$. Accordingly, for an arbitrary unit cell, j, the Euler-Lagrange governing equations stemming from Eqs. (3.2) are

$$\ddot{\bar{v}}_j + (2\bar{v}_j - \bar{v}_{j-1} - \bar{v}_{j+1}) + \frac{\partial \bar{\psi}(\bar{V}_j, \bar{v}_j)}{\partial \bar{v}_j} = 0, \tag{3.3a}$$

$$\ddot{\bar{V}}_j + \bar{s}_j(\bar{V}_j - \bar{V}_{j-1}) + \bar{s}_{j+1}(\bar{V}_j - \bar{V}_{j+1}) + \frac{\partial \bar{\psi}(\bar{V}_j, \bar{v}_j)}{\partial \bar{V}_j} = 0. \tag{3.3b}$$

for the LOC arrangement and

$$\ddot{\bar{v}}_j + (\bar{v}_j - \bar{V}_j) + \frac{\partial \bar{\psi}(\bar{v}_j, \bar{v}_{j+1})}{\partial \bar{v}_j} + \frac{\partial \bar{\psi}(\bar{v}_j, \bar{v}_{j-1})}{\partial \bar{v}_j} = 0, \tag{3.4a}$$

$$\ddot{\bar{V}}_j + (\bar{V}_j - \bar{v}_j) + \bar{s}_j(\bar{V}_j - \bar{V}_{j-1}) + \bar{s}_{j+1}(\bar{V}_j - \bar{V}_{j+1}) = 0, \tag{3.4b}$$

for the INT arrangement. In the simulations to follow, Eqs. (3.3) and (3.4) are used to model the response of the system to prescribed substrate boundary displacement.

To evaluate harmonic wave propagation in the overlaying metamaterial, we assume $\bar{s}_j$ is such that the substrate is comparatively rigid so that any disturbance propagating within the metamaterial does not transfer a meaningful portion of its energy into the substrate. Thus, we need only consider Eqs. (3.3a) and (3.4a) in the analysis. For the simplest case of a homogeneous

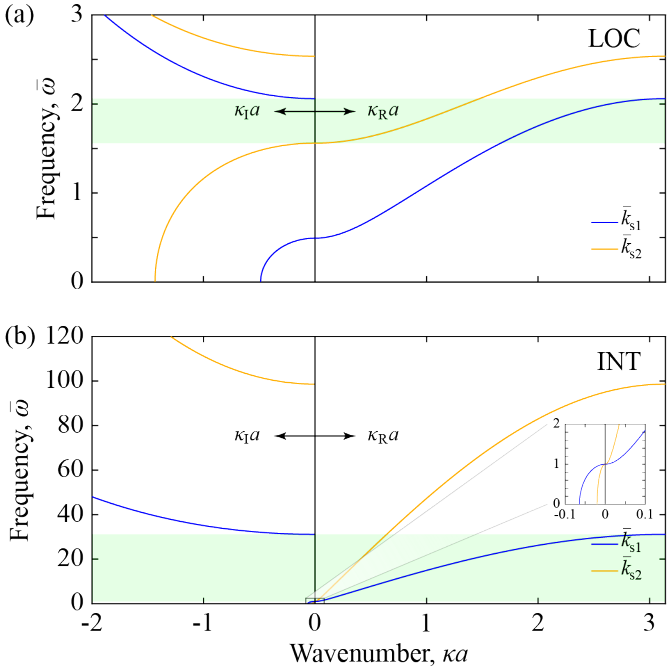

Figure 3.2: Dispersion Diagram. For an asymmetric bistable potential, the equilibrium stiffnesses are, generally, distinct, producing unique dispersion diagrams. In the above, the shaded region identifies the shared frequency range of the configuration-specific pass bands. The inset shows the frequency region of the lower band gap.

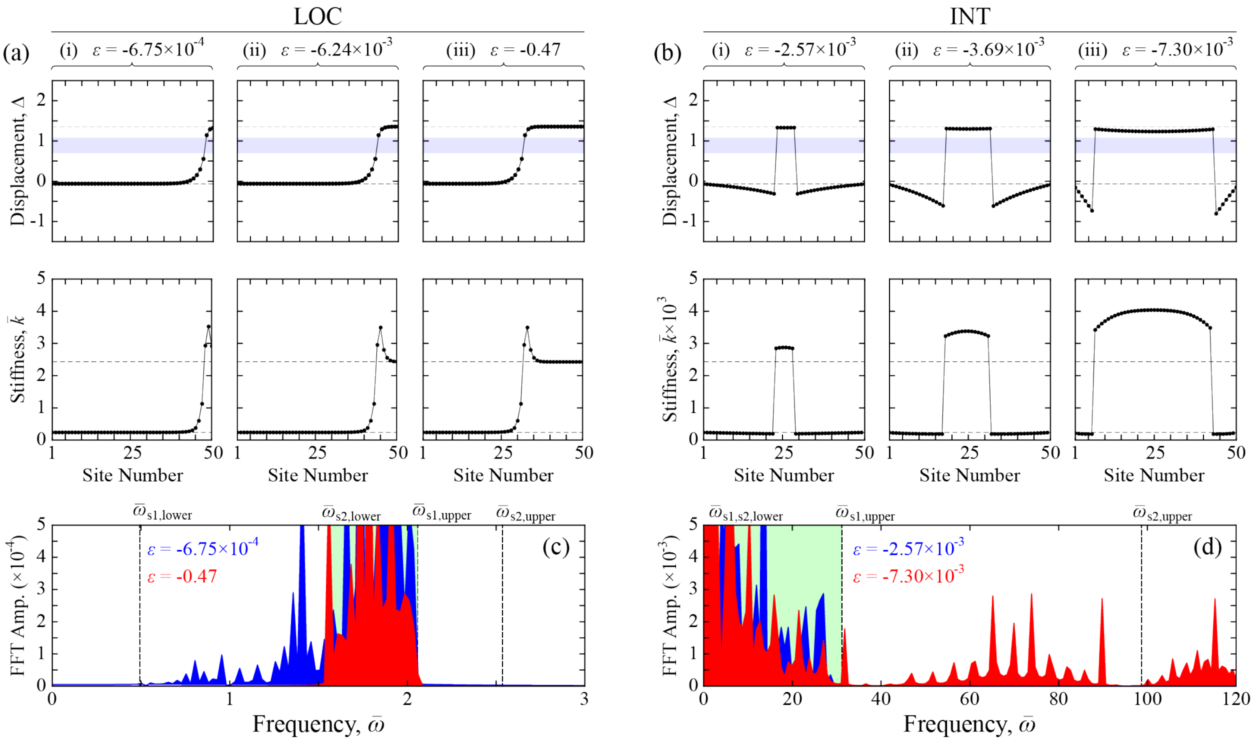

Figure 3.3: (Color online). Waveguide with Shifting Transparency. The relative displacement and stiffness profiles of bistable elements in the (a) LOC and (b) INT metamaterial-substrate arrangements. The dashed lines identify the stable equilibrium displacements, $\Delta_{s(i)}$, and stiffnesses, $\bar{k}_{s(i)}$. The indicated strain, ε, is that induced in the substrate by a quasi-statically applied (and subsequently removed) boundary displacement. (c,d) The strain-dependent stiffness profile affects the propagation of waves generated by an impulse. This is apparent in the non-coincident Fourier transforms of $\bar{v}_{50}(\bar{t})$ at different strains. The dashed lines represent the upper and lower frequency bounds of the pass bands for the homogeneous Δ_{s1} and Δ_{s2} configurations. The shaded region identifies the shared frequency range of the configuration-specific pass bands

metamaterial (i.e., bistable elements in identical configuration), the application of Bloch's theorem provides the characteristic dispersion relations for the LOC and INT arrangements, respectively, (see Appendix)

$$2+\bar{k}_{s(i)}-\frac{1}{\gamma}-\gamma=\bar{\omega}^2, \quad \text{(LOC)} \tag{3.5a}$$

$$1+\bar{k}_{s(i)}\left(2-\frac{1}{\gamma}-\gamma\right)=\bar{\omega}^2, \quad \text{(INT)} \tag{3.5b}$$

where $\bar{\omega} = \omega/\omega_0$ is the normalized wave frequency and $\gamma = \exp(\mathrm{i}\kappa a)$ the propagation constant with dimensionless complex wavenumber, κa. In solving Eqs. (3.5) for γ, the real (propagating) and imaginary (attenuating) components of the complex wavenumber are extracted as: $\kappa_{\mathrm{R}} a = |\mathrm{Re}\,(\mathrm{i}\ln\gamma)|$ and $\kappa_{\mathrm{I}} a = |\mathrm{Im}\,(\mathrm{i}\ln\gamma)|$.

3.4 Numerical Results

For analysis, the material and geometric parameters contained in Table 3.1 are utilized and are unique to each system. As detailed in the Appendix, the parameters define the bistable potential function, $\bar{\psi}$. Consequently, for both the LOC and INT arrangements, $\bar{k}_{\mathrm{s}2}/\bar{k}_{\mathrm{s}1} = 10$. Figure 3.2 displays the arrangement-specific dispersion curves for the metamaterial uniformly in each of the two stable configurations. The configuration-specific frequency ranges over which the metamaterial supports propagating waves begins to illustrate the anticipated performance tuning capability.

In the following subsections, respectively, we utilize substrates with constant and periodic spatial variation in stiffness, $\bar{s}_j$, to re-configure the overlaying metamaterial and alter its dynamic performance in the context of wave propagation. These will be applied to the establishment of waveguides with shifting transparency and metamaterials with tunable pass bands.

Table 3.1: Material and Geometric Parameters

	$\bar{k}_{\mathrm{A}}$	$\bar{k}_{\mathrm{T}}$	$\bar{k}_{\mathrm{M}}$	δ	ω_0^2
LOC	1/10	187/8791	71/565	2	100
INT	100	1957/92	14200/113	2	1/10

3.4.1 Waveguide with Shifting Transparency

To demonstrate the enhanced functionality acquired by a bistable metamaterial coupled to a strained elastic substrate, we first study the case of a homogeneous foundation, i.e., $\bar{s}_j =$ const. We consider a chain of $N = 50$ unit cells and, without loss of generality, initiate each bistable element in the first stable configuration, $\Delta_{\mathrm{s}1}$; thus, the original, untuned metamaterial is characterized by the stiffness, $\bar{k}_{\mathrm{s}1}$. Prescribed displacements are applied quasi-statically to the substrate boundaries, establishing a uniform internal strain, $\varepsilon = (\bar{V}_N - \bar{V}_1)/N$. As a consequence of substrate coupling, the metamaterial simultaneously deforms, effecting switching in certain bistable elements. Subsequently, the boundary displacements are quasi-statically removed, leaving a stable pattern of original and re-configured bistable elements which establishes the tuned metamaterial.

For the LOC arrangement, the k_{I} resist the metamaterial deformation, leading to a relative displacement between the local metamaterial and substrate degrees-of-freedom, $\Delta_j = \bar{v}_j - \bar{V}_j$, which changes signs about the midpoint of the mass-spring chain. Thus, switching is facilitated in bistable elements on one half of the metamaterial (especially closer to the boundary) and hindered in those elements on the opposite half. At most, substrate strain may re-configure only half of the bistable elements in the chain. A single domain wall separates the original and the switched elements, each characterized by acoustically distinct stiffnesses, $\bar{k}_{\mathrm{s}1}$ and $\bar{k}_{\mathrm{s}2}$, respectively. These effects are depicted in Fig. 3.3a for increasing (compressive) substrate strain.

For the INT arrangement, the bistable elements oppose the metamaterial deformation, $\Delta_j = \bar{v}_j - \bar{v}_{j+1}$, which, due to the free metamaterial boundaries, decreases in magnitude from the chain midpoint but does not change sign. Therefore, all elements are susceptible to re-configuration, although elements nearer the metamaterial interior will switch first. In addition, as switching entails $\Delta_j \neq 0$, in the absence of the substrate, the tuned metamaterial would exhibit a lingering deformation (i.e., a residual strain) – the more elements that switch, the greater the effect. However, the substrate counteracts this effect and, since it is rigid (though elastic) compared to the metamaterial, generally, $\Delta_j \neq \Delta_{\mathrm{s}(i)}$, as for the LOC arrangement. For the INT arrangement, two domain walls form as a consequence of interior elements switching before those nearer the boundaries; however, since Δ_j deviates from the equilibrium values, $\Delta_{\mathrm{s}(i)}$, the local stiffness, $\bar{k}_j$, also deviates from $\bar{k}_{\mathrm{s}(i)}$. These effects are depicted in Fig. 3.3b for increasing (compressive) substrate strain.

To demonstrate the strain-dependent wave dynamics of the tuned metamaterial, Figs. 3.3c,d display the FFT of the time signal $\bar{v}_{50}(\bar{t})$ following an impulse, $\dot{\bar{v}}_1(\bar{t})\delta(\bar{t}-\bar{t}_0)$, which instigates a propagating disturbance. An absorbing boundary consisting of an additional 200 cells with $\bar{k}_j = \bar{k}_{50}$ $(51 \leq j < 250)$ and linearly increasing damping is utilized. Dependent upon the specific tuned stiffness profile, $\bar{k}_j$, the frequency range over which the metamaterial is transparent to propagating waves shifts. For the LOC arrangement in Fig. 3.3c, following a substrate strain of $\varepsilon = -6.75 \times 10^{-4}$, the metamaterial dynamics is essentially unchanged as few bistable elements are re-configured; consequently, components of the transmitted signal lie within the pass band associated with $\bar{k}_{\mathrm{s}1}$ in Fig. 3.2a. Following a substrate strain of $\varepsilon = -0.47$, the metamaterial exhibits two domains characterized by $\bar{k}_{\mathrm{s}1}$ and $\bar{k}_{\mathrm{s}2}$, respectively; therefore, the components of the transmitted signal are restricted to the narrower frequency range in which the dispersion curves in Fig. 3.2a overlap. Outside this range, wave motion is hindered by Bragg scattering and confined to the domain in which the disturbance was generated. A similar effect is observed for the INT arrangement in Fig. 3.3d where sufficient substrate strain causes most of the bistable elements to

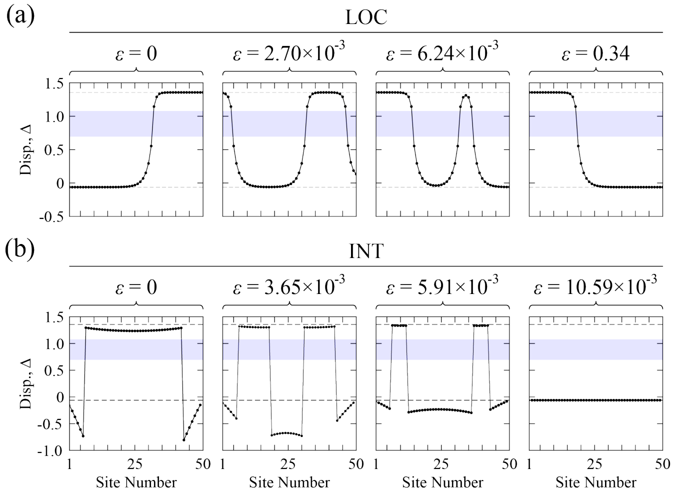

Figure 3.4: Reversibility of LOC and INT Arrangements. In response to substrate strain, the relative displacement, Δ_j, exhibits a sign change in the LOC arrangement but not in the INT arrangement. Above, metamaterials in the (a) LOC and (b) INT arrangements are initialized in the tuned configurations in Figs. 3.3a.(iii) and b.(iii), respectively, which were attained via substrate compression. Subsequently, submitting the substrate to tension reveals the reversibility of tuning the overlaying metamaterial. The INT metamaterial is able to return to its original, untuned state while the LOC metamaterial is not.

switch. Note, however, that the residual strain causes the stiffness profile to deviate from $\bar{k}_{s2}$ in the switched region and so the frequency range of components within the transmitted wave deviates from that indicated by Fig. 3.2b.

The results depicted in Fig. 3.3 demonstrate the utility of an elastic substrate for tuning metamaterials with multistable elements: with access to only the substrate boundaries, the multistable elements at the boundary and within the interior may be switched. In contrast, earlier works utilizing multistable elements for tunable metamaterial performance offer no means of switching individual or isolated groups of elements in the interior. For both the LOC and INT arrangements, a strained substrate enables altering the metamaterial morphology (i.e., the stiffness distribution)[2] and, as a result, the transmission of incoming waves.

---

[2] For the LOC arrangement, the interaction springs prevent the transition region from advancing beyond the midpoint. The INT arrangement is not so limited.

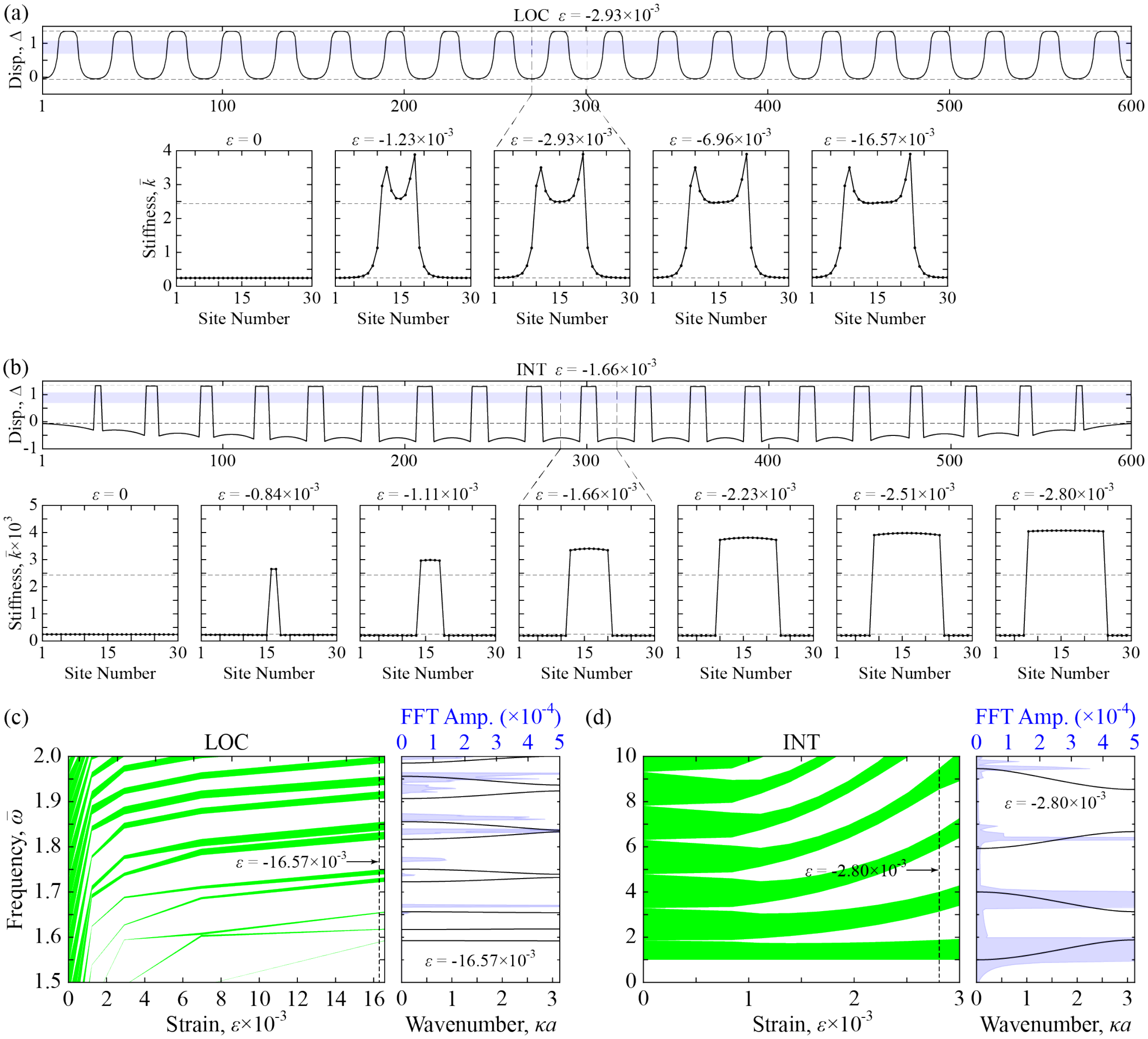

Figure 3.5: (Color online). Metamaterial with Tunable Unit Cell Morphology. (a,b) Subject to boundary displacement, a substrate with periodic stiffness variation elicits a displacement profile, Δ_j, with similar periodicity, leading to periodic element re-configuration and stiffness modulation, $\bar{k}_j$. The (analytical) dispersion pass bands and the (numerical) FFT of a simulated disturbance are compared, revealing rough agreement for the (c) LOC system away from flat bands and excellent agreement for the (d) INT arrangement at lower frequencies.

The manner in which the two arrangements facilitate switching bistable elements impacts the reversibility of the tuned metamaterial configurations. Recall that, for the LOC arrangement, Δ_j exhibits a sign change about the system midpoint, promoting switching in one half of the mass-spring chain and reinforcing the native state it in the other half. From the tuned metamaterial configuration, reversing the substrate strain inverts Δ_j and, thus, the bistable elements in re-configured half are directed back to the native state while those in the native state are switched. Therefore, generally, the LOC arrangement does not support reversible tuning. Alternatively, for the INT arrangement, Δ_j does not exhibit a sign change but is maximum (in magnitude) near the system midpoint, causing switching to commence there. From the tuned metamaterial configuration, inverting Δ_j by reversing the substrate strain returns the switched elements to their native configurations without re-configuring any elements presently in the native configuration. Therefore, generally, the INT arrangement supports reversibility. These effects are observed in Fig. 3.4 and the Supplemental animations.

3.4.2 Unit Cell with Variable Morphology

In the preceding subsection, a homogeneous substrate (i.e., $\bar{s}_j = \text{const.}$) supports a uniform strain distribution which re-configures the bistable elements in the overlaying metamaterial: for the LOC arrangement, switching commences at one of the metamaterial boundaries; for the INT arrangement, switching initiates within the interior. Naturally, substrates with a variable stiffness profile (i.e., $\bar{s}_j \neq \text{const.}$) will alter these results and may deliver an enhanced tuning capability. A substrate with monotonic stiffness function, for example, (not presented here) would permit switching elements in the LOC chain beyond (or short of) the current limit at the chain midpoint and, in the INT chain, would allow switching to initiate at or nearer a boundary rather than the interior. Nevertheless, in the following, we consider an elastic foundation with periodic stiffness function in order the effect a metamaterial with variable unit cell morphology for wave control.

For simplicity, we consider a bi-material substrate with stiffnesses α and β ($\alpha < \beta$) which, as before, are sufficiently large to ensure that the substrate is rigid compared to the overlaying metamaterial. These stiffnesses are distributed periodically within the substrate with a unit cell comprising thirty springs; therefore, the overlaying metamaterial, once tuned, is expected to exhibit the same periodicity. In particular, for the LOC arrangement, $\bar{s}_j = \alpha$ for $j \leq 15$ and $\bar{s}_j = \beta$ for $15 < j \leq 30$; for the INT arrangement, $\bar{s}_1 = \alpha$ and $\bar{s}_j = \beta$ for $1 < j \leq 30$. The interface between the two stiffness regions provides a nucleation site at which switching may commence. Utilizing alternative bi-material distributions or multi-material substrates, isolated regions of the metamaterial may be designed to switch in a pre-determined sequence; nevertheless, this is not present interest. In the following, we consider wave propagation within finite systems consisting of twenty of the earlier defined unit cells.

Figures 3.5a,b illustrate the state of the bistable elements in the metamaterial for the LOC and INT arrangements, respectively. In particular, the first row shows the relative displacement, Δ_j, for the twenty-cell systems corresponding to the indicated nominal strain induced by boundary displacement. Apparently, the periodic substrate supports an internal strain field with the same periodicity which assists in switching the bistable elements at the same spatial intervals. To the purpose of tunable wave propagation, the second row of each sub-figure, focuses on the variation of the morphology, $\bar{k}_j$, over the unit cell at several levels of substrate strain. Substrate strain changes the distribution of the bistable stiffness within the unit cell which impacts the metamaterial dispersion characteristics.

We compute the dispersion curves utilizing the stable, strain-dependent metamaterial unit cells. In each stable configuration, following the definition in Sec. 3.3. A., the local stiffness $\bar{k}_j = k(\Delta)$ is determined at each jth element of the re-configured unit cell, and then a dispersion analysis is performed for the system of $N = 30$ elements by suitably extending Eqs. (3.3) and (3.4) and apply Bloch's theorem, $\bar{v}_1 = \bar{v}_{30}\gamma$ (see Appendix). Figures 3.5c,d show how the frequency range of pass bands, respectively, in the overlaying LOC and INT metamaterials change as a function of substrate strain. We also determine the FFT of the time signal $\bar{v}_{600}(\bar{t})$ following an impulse, $\dot{\bar{v}}_1(\bar{t})\delta(\bar{t}-\bar{t}_0)$. Again, an absorbing boundary with $\bar{k}_j = \bar{k}_{600}$ ($601 \leq j < 800$) and linearly increasing damping is utilized. For a particular strain, we compare the computed dispersion and the FFT from time simulation. For both the LOC and the INT arrangement, there is excellent agreement between the analytical and numerical results. These results, together with those of the previous section, support the notion of inherent and tunable wave control via an adjustable material morphology. Comparing the common frequency regions in the FFTs in Figs. 3.3c,d and 3.5c,d, we notice that periodic distributions of $\bar{k}_j$ opens additional band gaps, illustrating the impact of the present repeating morphology with respect to the relatively simple variations in Sec. 3.4.1. Although, the overlaying metamaterial in the LOC arrangement is capable of stable and continuous tuning, except for a narrow range of tuned configurations, it is irreversible. However, in the case of an INT-type system, the tuning processes is able to meet all three requirements – stable, reversible, and continuous.

3.5 Conclusion

Typically, metamaterial tuning schemes demonstrate continuity, stability, or reversibility individually or in pair-wise but not triple combination. In this article, we propose a one-dimensional system comprised of a bistable metamaterial on an elastic substrate which permits continuous, stable, and reversible adjustments to the morphology through strain engineering and, thus, tunable dynamic performance. This is demonstrated in the form of a waveguide with variable pass band and a metamaterial unit cell with flexible morphology supporting a tunable dispersion. The strategy of strain engineering for morphological tuning can be extended to higher dimensions, however, the results are generally not stable[61, 139] in the absence of persistent substrate strain. However, e.g., defects and the interaction of nonlinear wave modes with the transition zone represent two promising methods to overcome this obstacle. In addition, as s_j approaches $\bar{k}_{\mathrm{I}}$, the substrate not only begins to participate in shaping the wave dynamics together with the metamaterial but also begins to sustain an apparent deformation profile (i.e., warping) in the face of non-uniform metamaterial morphologies (see Supplementary Material, Sec. 3.5). This effect suggests an alternative route to programming shape in soft matter.[140]

Supplementary Material

See Supplementary material[3] for animations, further details of the tuning and potential recovery of the metamaterial in LOC and INT arrangements.

Appendix

Potential Function

Consider each term in Eq. (3.1) in turn. From the geometry illustrated in Fig. 3.1a, where $\delta = d_{\mathrm{y}}/d_{\mathrm{x}}$, the instantaneous length of an axial spring is $\ell(\Delta) = d_{\mathrm{x}}\bar{\ell}(\Delta) = d_{\mathrm{x}}\sqrt{(1-\Delta)^2+\delta^2}$ and, therefore, its natural length is $\ell_0 = d_{\mathrm{x}}\bar{\ell}(0)$. Thus, the contribution of axial springs to the on-site

---

[3] `https://aip.scitation.org/doi/suppl/10.1063/1.5145324`

potential is given by

$$\psi_{\mathrm{A}}(\Delta) = k_{\mathrm{A}} d_{\mathrm{x}}^2 \left[\bar{\ell}(\Delta) - \bar{\ell}_0\right]^2.$$

In general, for a dipole moment $\mathbf{p}$ in a magnetic field $\mathbf{B}$, the potential energy is given by $\psi_{\mathrm{M}} = -\mathbf{p} \cdot \mathbf{B}$. The field $\mathbf{B}$ of an arbitrary, point-like magnetic dipole $\mathbf{p} = p\hat{\mathbf{p}}$ is[141, 142]

$$\mathbf{B}(\mathbf{p}, \mathbf{r}) = \frac{\mu_0 p}{4\pi |\mathbf{r}|^3} \left[\frac{3}{|\mathbf{r}|^2}(\hat{\mathbf{p}} \cdot \mathbf{r})\mathbf{r} - \hat{\mathbf{p}}\right],$$

where $\mathbf{r}$ is the position vector of a point in space relative to the position of the field-generating dipole and μ_0 is the permeability of free space. At present, the dipole moment under consideration is that affixed to the mass, $\mathbf{p}_{\mathrm{m}}$, and $\mathbf{B}$ is that resulting from the superposition of fields generated by the $\mathbf{p}_{\mathrm{s}}$ pair at the site of $\mathbf{p}_{\mathrm{m}}$. To ensure a horizontal resultant, $\mathbf{p}_{\mathrm{m}}$ remains parallel to the x-axis while the orientation, θ, of $\mathbf{p}_{\mathrm{s}}$ is symmetric about the horizontal axis. For our system, the position vector can be written $\mathbf{r} = d_{\mathrm{x}}\bar{\mathbf{r}}$ and the magnetic potential becomes

$$\psi_{\mathrm{M}} = k_{\mathrm{M}} d_{\mathrm{x}}^2 \sum_{i=1}^{2} \frac{\hat{\mathbf{p}}_{\mathrm{m}}}{|\bar{\mathbf{r}}_i|^3} \cdot \left[\frac{3}{|\bar{\mathbf{r}}_i|^2}(\hat{\mathbf{p}}_{\mathrm{s}(i)} \cdot \bar{\mathbf{r}}_i)\bar{\mathbf{r}}_i - \hat{\mathbf{p}}_{\mathrm{s}(i)}\right],$$

where $k_{\mathrm{M}} = \mu_0 p_{\mathrm{s}} p_{\mathrm{m}} / 4\pi d_{\mathrm{x}}^5$. Notice that the magnetic potential does not include contributions from dipole moments in neighboring bistable elements.

Finally, the torsional springs resist the angular displacement, $\varphi(\Delta)$, of the axial springs relative to some arbitrary offset, φ_0, and may be regarded as the bending resistance from the ends of the axial springs fixed to the substrate. For simplicity, $\varphi_0 = \tan^{-1}[(1 - \Delta_{\mathrm{s}(i)})/\delta]$, where the specific value of i is that for which $\Delta_{\mathrm{s}(i)}$ is in the upper energy well of the total potential constructed from ψ_A and ψ_M alone; consequently,

$$\psi_\mathrm{T}(\Delta) = k_\mathrm{T}\left[\tan^{-1}\left(\tfrac{1-\Delta}{\delta}\right) - \tan^{-1}\left(\tfrac{1-\Delta_{\mathrm{s}(i)}}{\delta}\right)\right]^2.$$

Following the normalization described in Sec. 3.3.2, we define $\bar{k}_\mathrm{A} = k_\mathrm{A}/k_\mathrm{I}$, $\bar{k}_\mathrm{M} = k_\mathrm{M}/k_\mathrm{I}$, and $\bar{k}_\mathrm{T} = k_\mathrm{T}/k_\mathrm{I}d_\mathrm{x}^2$.

Dispersion Relations

Following Eqs. (3.3) and (3.4), the matrix equations of motion for an arbitrary unit cell are given by:

$$\begin{bmatrix} 1 & -1 \\ -1 & 1+\bar{k}_{\mathrm{s}(i)}-\bar{\omega}^2 \end{bmatrix}\begin{bmatrix} \bar{v}_{j-1} \\ \bar{v}_j \end{bmatrix} = \begin{bmatrix} f_{j-1} \\ f_j \end{bmatrix}, \quad \text{(LOC)}$$

$$\begin{bmatrix} \bar{k}_{\mathrm{s}(i)} & -\bar{k}_{\mathrm{s}(i)} \\ -\bar{k}_{\mathrm{s}(i)} & 1+\bar{k}_{\mathrm{s}(i)}-\bar{\omega}^2 \end{bmatrix}\begin{bmatrix} \bar{v}_{j-1} \\ \bar{v}_j \end{bmatrix} = \begin{bmatrix} f_{j-1} \\ f_j \end{bmatrix}, \quad \text{(INT)}$$

where f_j and f_{j-1} are the forces applied by the adjacent unit cells. Following Sec. 3.3. A., the local stiffness is given by $\bar{k}(\Delta) = \partial^2\bar{\psi}/\partial\Delta^2$; therefore, $\bar{k}_{\mathrm{s}(i)} = \bar{k}(\Delta_{\mathrm{s}(i)})$ are the stiffnesses associated with the two stable configurations, $\Delta_{\mathrm{s}(i)}$, $i = 1,2$. Recall, for the LOC arrangement, $\Delta = \bar{v}_j - \bar{V}_j$ and, for the INT arrangement, $\Delta = \bar{v}_{j-1} - \bar{v}_j$. Following Bloch's theorem, $\bar{v}_{j-1} = \bar{v}_j\gamma$, where $\gamma = \mathrm{e}^{-\mathrm{i}\kappa a}$ is the complex propagation constant with wavenumber κ. Thus, the displacement transformation $\left[\bar{v}_{j-1}, \bar{v}_j\right]^\mathrm{T} = \mathbf{T}\bar{v}_j$, where $\mathbf{T} = [\gamma \quad 1]^\mathrm{T}$ is the Bloch transformation matrix. Simultaneously, pre-multiplying the matrix equations of motion by the conjugate transpose, $\mathbf{T}^\mathrm{H}$, and applying the displacement transformation – recognizing that cell equilibrium requires $\mathbf{T}^{\mathrm{H}}\mathbf{f} = \mathbf{0}$ – reduces the equation dimensions. The subsequent determinate establishes the metamaterial characteristic wave dispersion relations in Eqs. (3.5).

Declaration

Chapter 3, in full, is a reprint of the material as it appears in V. Ramakrishnan and M. J. Frazier, “Multistable metamaterial on elastic foundation enables tunable morphology for elastic wave control”, *J. Appl. Phys.*, **vol. 127**, p. 225104, June 2020. The dissertation author is the primary author of this paper.

Chapter 4

Transition Waves in Multistable Metamaterials with Space-time Modulated Potentials

This chapter is published in:

Applied Physics Letters, **117**, 151901 (2020)

DOI: 10.1063/5.0023472

4.1 Abstract

This letter introduces a strategy for transition wave (soliton) management in multistable mechanical metamaterials, enabling on-demand, post-fabrication control of the associated phase transformation kinetics and distribution. Specifically, the wave dynamics are controlled by a

small, kinematically-prescribed spatio-temporal variation in the elastic potential, constituting a driving force. The stability of the wave profile under slow-propagation conditions and the characteristic spatial localization of the Hamiltonian energy supports an analogy with a Newtonian particle traversing a viscous medium under forcing. The theoretical analysis adopts this particle perspective, describing the soliton dynamics through ordinary, rather than partial, differential equations. While myriad definitions for the potential modulation are possible, a traveling sinusoid assists the development of analytical solutions. Following this prescription, two wave propagation regimes are revealed: in one, the soliton is carried by the modulation with a commensurate velocity; in the other, the soliton is out-paced by the modulation and, thus, travels at reduced velocity. To illustrate the utility of this method, we demonstrate both the tractor and repulsor effects in multistable systems away from equilibrium: as a tractor (repulsor), the potential variation attracts (repels) the transition wave front in opposition to the system's energy-minimizing tendency. This method provides greater flexibility to the transformation performance of multistable metamaterials and supports the adoption of such systems in applications demanding multi-functionality.

4.2 Introduction

Thus, understanding the nature and behavior of topological solitons/ transition waves is a crucial avenue to control the response of multistable metamaterials. In this project, we now perform a theoretical study of (topological) soliton response to a general external spatio-temporal forcing and put forth a modified bistable element model to practically implement this method via kinematic modulations to the elastic potential, commanding the soliton dynamics.

Solitons[143] are a class of spatially localized, large-amplitude solutions to non-linear equations which describe a variety of processes within several domains of science, including biology,[144–146] chemistry,[147,148] cosmology,[149,150] and the materials sciences.[151–154] In the context of materials with multiple equilibrium states, the propagation of topological solitons is a model for, e.g., polarization switching in ferroelectric[51] and ferromagnetic[52] materials, and structural phase transitions[53–55] – transformation phenomena which impact material performance and underpin multi-functionality in applications.[56] Recently, mechanical metamaterials[57] characterized by multistable internal architectures have exhibited similar behavior,[58–66] extending atomic-scale physics and multi-functionality to the readily-accessible structural level. Command of the soliton dynamics promotes their utility in applications; however, for metamaterials, strategies for soliton management are few and often involve permanent modifications to the internal architecture (e.g., local/extended defects[62,64]) which "lock in" performance at fabrication, preventing on-demand control of the transformation kinetics and phase distribution. The tunable elastic metamaterial design resting on a periodic, stiff elastic medium described in the previous section provided a finite discrete number of stable configurations, essentially relocating the transition regions within, to switch the effective acoustic response on application of a boundary strain. Although the design provides an improved capacity to dictate soliton positions, these states are pre-programmed into the structure once the periodicity of the substrate and elastic elements are chosen. Thus, a general, continuous means to control soliton dynamics is a desirable capability and motivates the present letter.

In practice, at the atomic scale, the environment in which a soliton [henceforth, synonymous with transition wave and (anti-)kink] propagates is hardly ideal: external fields, the effects of thermal noise, and structural impurities are each factors which affect the soliton dynamics and have been the subject of intense investigation, especially in the context of solid-state physics.[155–157] In addition to their relevance as incidental affects, these factors are simultaneously of practical import as instruments of transition wave control[158,159] which also extend to the metamaterial platform. In particular, the application of spatio-temporal forcing to the soliton wave front (e.g., by electric/magnetic fields) does not necessarily require permanent modifications to the internal architecture and opens the door to remote control. In the following, we study the dynamics of an elastic bistable lattice with spatio-temporal forcing arising from a similarly variable potential function; the modulation stimulating the propagation of otherwise static topological solitons with predictable velocity. The results contribute to the theoretical understanding of soliton dynamics in multistable metamaterials, facilitating the integration of these systems into applications demanding post-fabrication tuning and multi-functionality.

4.3 Theory

For the theoretical analysis, we consider the evolution of a one-dimensional, bistable continuous mechanical system, subject to prescribed spatio-temporal forcing, $f(x,t)$. The governing equation for the displacement field, $u(x,t)$, has the basic form

$$u_{,tt} - u_{,xx} + \psi'(u) = f(x,t) - \eta u_{,t}, \tag{4.1}$$

where η is the viscosity and $\psi'(u)$ is the force stemming from a symmetric, non-convex on-site potential, $\psi(u)$; one with two degenerate ground states, u_{S1} and u_{S2} (Fig. 4.1a). Under free-wave conditions ($\eta = 0, f = 0$), the system supports a number of traveling solutions; in particular, the topological modes (e.g., the anti-kink [Fig. 4.1b]) which we intend to manipulate.

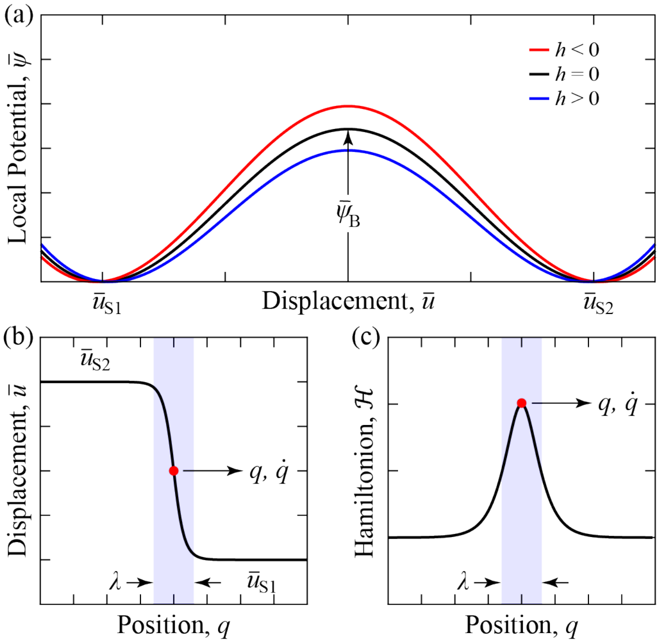

Figure 4.1: Bistable Potential and Soliton Properties. (a) Local bistable potential facilitating the formation of (b) a soliton mode (anti-kink) with wavelength, λ, measuring the width of the transition region (shaded) [i.e., where $\psi''(u) < 0$]. The energy barrier, $\psi_{\mathbf{B}}$, separates degenerate ground states, u_{S1} and u_{S2}. (c) The Hamiltonian density, $\mathscr{H}$, exhibiting the characteristic soliton energy localization with $\mathscr{H} \to 0$ as $|q| \to \infty$. The dot identifies the energy maximum.

With characteristic length, a, a snapshot of the corresponding Hamiltonian density,[160] $\mathscr{H} = \frac{1}{a}[\frac{1}{2}u_{,t}^2 + \frac{1}{2}u_{,x}^2 + \psi(u)]$, reveals the compact nature of the soliton energy distribution, reminiscent of a particle, an object with localized properties (Fig. 4.1c). Apart from myriad alternative choices, the point at which the energy density is maximal is a natural choice for the soliton center; therefore, for the soliton quasi-particle, we define the time-dependent position, $q(t) = (\Delta u)^{-1} \int_{-\infty}^{\infty} x u_{,x} \, \mathrm{d}x$, and velocity, $\dot{q}(t) = s(t) = (\Delta u)^{-1} \int_{-\infty}^{\infty} x u_{,xt} \, \mathrm{d}x$, where $\Delta u = \int_{-\infty}^{\infty} u_{,x} \, \mathrm{d}x$.

From $\mathscr{H}$, the total energy, E, of the free soliton particle is readily determined:[160]

$$E = \int_{-\infty}^{\infty} \mathscr{H} \mathrm{d}x = \sqrt{\frac{2}{1-s^2}} \int_{u_1}^{u_2} \sqrt{\psi(u)} \mathrm{d}u = m_0 \gamma,$$

where $m_0 = \sqrt{2} \int \sqrt{\psi(u)} \mathrm{d}u$ is the particle rest mass. The relativistic mass, $m = m_0 \gamma$, is tied to the soliton velocity, s, via the Lorentz contraction factor, $\gamma^{-1} = \sqrt{1-s^2}$. Likewise, γ also regulates the soliton shape, decreasing the wave width, λ, with increasing propagation speed. Thus, the mass properties of the proposed soliton particle are not fixed quantities. However, if $s \ll 1$ (i.e., $\gamma \approx 1$), then measures of the relativistic and rest mass coalesce, and the soliton profile is, essentially, unchanged compared to the static case. Provided that the slow propagation condition, $s \ll 1$, is realized, then the interpretation of the free soliton as a non-relativistic (i.e., Newtonian) particle is justified;[160,161] similarly, Eq. (4.1) represents a particle acted upon by perturbing forces, $-\eta u_{,t}$ and $f(x,t)$. In the following, we utilize the particle description to apply Newtonian dynamics to determine the response of transition waves to simultaneous space- and time-dependent forcing stemming from a similar dependency in the potential of the host medium. As a phenomenological construction, Eq. (4.2) is, perhaps, the simplest description of a dissipative system with independent local and non-local potential variation:

$$u_{,tt} - [1+g(x,t)]\, u_{,xx} + [1-h(x,t)]\, \psi'(u) = -\eta u_{,t}, \tag{4.2}$$

which can be arranged in the form of Eq. (4.1) with $f(x,t) = g(x,t)u_{,xx} + h(x,t)\psi'(u)$. More complicated formulations may, e.g., include additional spatial derivatives of u with space-time coefficients. In the context of the physical metamaterial, space-time coefficients such as $g(x,t)$ and $h(x,t)$ may be the effects of, e.g., prescribed external fields on stimuli-responsive elastic constituents or kinematically-activated geometric non-linearities.

Accompanying the particle position and velocity is the momentum, $p(t) = m\dot{q}(t)$, whose time rate-of-change balances the perturbing forces (see Supplementary Material [SM], Sec. 4.5):

$$\begin{aligned}\dot{p} &= \int_{-\infty}^{\infty} [f(x,t) - \eta u_{,t}]\, u_{,x}\, \mathrm{d}x \\ &= \int_{-\infty}^{\infty} f(x,t) u_{,x}\, \mathrm{d}x - \eta m \dot{q}(t) = m_0 \gamma^3 \ddot{q}(t),\end{aligned}$$

where we utilize the relation $p(t) = \int_{-\infty}^{\infty} u_{,t}\, u_{,x}\, \mathrm{d}x$. Evaluating the integral, $I(t) = \int_{-\infty}^{\infty} f(x,t) u_{,x}\, \mathrm{d}x$, and solving for $\ddot{q}(t)$ yields

$$\ddot{q}(t) = \frac{1}{m_0 \gamma^3} I(t) - \frac{\eta}{\gamma^2} \dot{q}(t) \approx \frac{1}{m_0} I(t) - \eta \dot{q}(t), \tag{4.3}$$

the main theoretical result; the approximation recognizes the requisite slow-propagation condition, $s \ll 1$ (i.e., $\gamma \approx 1$). Furthermore, although soliton propagation may be stimulated by $f(x,t)$, if significant deformation of the soliton profile occurs, then the accuracy of the prediction [Eq. (4.3)] diminishes. Naturally, integrating Eq. (4.3) delivers the desired $q(t)$ and $\dot{q}(t)$.

4.4 Numerical Analysis

To demonstrate the effectiveness of our strategy as well as to validate our theoretical predictions, we consider the non-linear dynamics of the discrete bistable metamaterial chain depicted in Fig. 4.2 which is a variant of the well-known system found in many theoretical[70, 101, 136] and experimental[60, 62] studies. Although we could proceed with model stimuli-responsive stiffness elements (results are qualitatively similar [see SM, Sec. 4.5]), we opt for a purely kinematic approach. The essential bistable element comprises two identical, pin-connected springs of stiffness k_{B} symmetrically arranged about the horizontal axis. The mass, m, affixed to the common

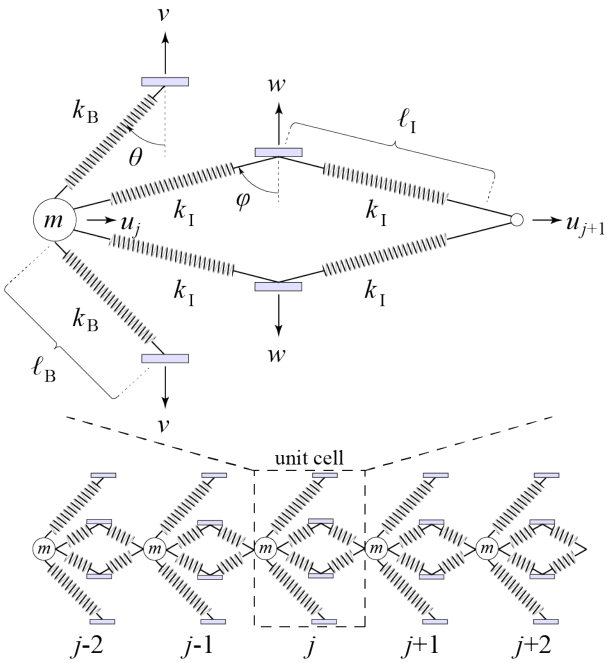

Figure 4.2: Lattice with Space-Time Variable Potential. Prescribed displacements, $v(x,t)$ and $w(x,t)$ adjust the metamaterial geometry, facilitating local and non-local potential modulation, respectively.

node is restricted to horizontal displacements, $\bar{u} = u/(\ell_{\mathrm{B}} \sin\theta)$. Consequently, the corresponding on-site potential function, possesses two degenerate ground states $\bar{u}_{\mathrm{S1,S2}} = 0, 2$. As one notable distinction with similar designs in prior studies, the remote ends of each spring may displace vertically, $\bar{v} = v/(\ell_{\mathrm{B}} \cos\theta)$. As a second distinction, neighboring degrees of freedom, $\bar{u}_j$ and $\bar{u}_{j+1}$, are linked by spring assemblies which permit adjustments to the coupling strength through vertical displacements, $\bar{w} = w/(\ell_{\mathrm{I}} \cos\varphi)$. For a lattice in which the vertical displacements depend on space and time, so too does the potential. In particular, $\bar{v}$ comprises a function which modifies the on-site potential in a manner similar to h in Fig. 4.1a. Thus, the non-dimensional equation of motion for an arbitrary degree of freedom, $\bar{u}_j$, within the lattice is (see SM, Sec. 4.5)

$$\begin{aligned} &\bar{u}_{j,\bar{t}\bar{t}} + \bar{\eta}\bar{u}_{j,t} + \bar{\chi}_{,\bar{u}_j}(\bar{u}_j,\bar{u}_{j+1}) \\ &\quad + \bar{\chi}_{,\bar{u}_j}(\bar{u}_j,\bar{u}_{j-1}) + \left[1 - h(\bar{u}_j,\bar{v}_j)\right]\bar{\psi}'(\bar{u}_j) = 0, \end{aligned} \tag{4.4}$$

where $\bar{\chi}(\bar{u}_j,\bar{u}_{j\pm1})$ is the interaction potential function. The continuum approximation of the lattice governing equations resembles the form of Eq. (4.2). In simulation, we adopt the dimensionless material and geometric parameters $\bar{k}_{\mathrm{B}} = 0.02$, $\bar{k}_{\mathrm{I}} = 0.6728$, $\theta = \pi/4$, and $\varphi = \tan^{-1}(5/2)$. The system parameter, $\tau = 0.1\mathrm{s}$, relates the dimensional and dimensionless times, $t = \tau\bar{t}$. The

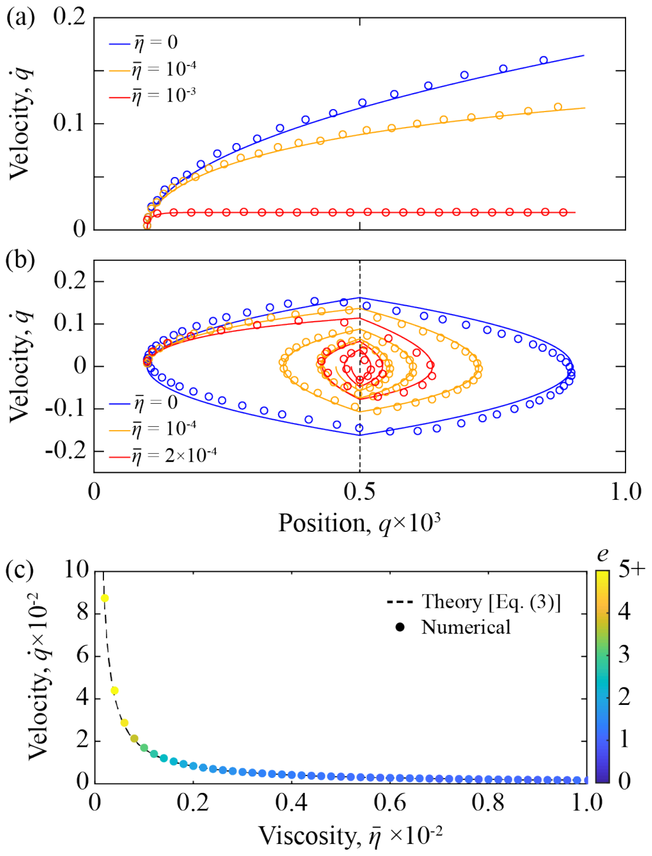

Figure 4.3: (color online). Soliton in Static Potential Grading. A comparison of theoretically predicted (solid line) and numerically observed (dots) soliton response in (a) a linear and (b) a triangular potential grading (system minimum at $q = 500$) at various levels of material damping. (c) Percent error, e, in the numerical steady-state velocity results for a linear potential grading relative to that predicted by Eq. (4.3) as a function of damping intensity.

displacement amplitudes for $\bar{v}$ and $\bar{w}$ should be kept small in order to preserve the soliton profile consistent with the particle perspective ingrained in the theoretical results.

Figure 4.3 compares the predicted and simulated response of an initially static topological mode to a spatially prescribed on-site potential for various damping intensities. For the case in which the $\bar{v}_j$ change linearly (modulation in $\bar{w}$ yields qualitatively similar results [see SM, Sec. 4.5]) such as to likewise lower the potential in the propagation direction (in this study, $\bar{\psi}_{\mathrm{B}}$ is reduced, at most, by 2.5%), the simulated position and velocity are well-described by Eq. (4.3) as evidenced by the comparisons in Fig. 4.3a. The (anti-)kink travels down the potential grading the length of the lattice such that the associated phase transformation is uni-directional and complete. Nevertheless, since the bistable potential possesses degenerate ground states, the system supports both kink and anti-kink modes, facilitating reversible transformations.[62] Conceivably, e.g., following a binary scheme with $\bar{u}_{\mathrm{S1}} \equiv \mathrm{ON}$ and $\bar{u}_{\mathrm{S2}} \equiv \mathrm{OFF}$, alternating soliton modes may constitute damping-tolerant, continuous mechanical signals for information transmission in, e.g., completely soft robots and machines.[134, 162, 163]

For vanishing initial conditions and non-zero viscosity, Eq. (4.3) gives $\dot{q}(\bar{t}) = I(1 - \mathrm{e}^{-\bar{\eta}\bar{t}})/m_0\bar{\eta}$ as the soliton velocity which converges to the steady-state value $\dot{q}_{\mathrm{ss}} = I/m_0\bar{\eta}$, a result similar to that obtained by Hwang and Arrieta[62] via a perturbation approach. Figure 4.3c compares the theoretical and numerical [at $\bar{t} \geq -\frac{1}{\bar{\eta}}\ln(0.01)$] results for $\dot{q}_{\mathrm{ss}}$ as a function of the viscosity, revealing greater agreement toward higher values of $\bar{\eta}$ (equiv., slower propagation speeds) as measured by the relative percentage error, e. As $\bar{\eta} \to 0$ and the steady-state velocity increases, the relativistic effects disregarded in the formulation of Eq. (4.3) become significant, widening the discrepancy between theory and simulation.

For the case in which the $\bar{v}_j$ change non-monotonically, the traveling soliton may be

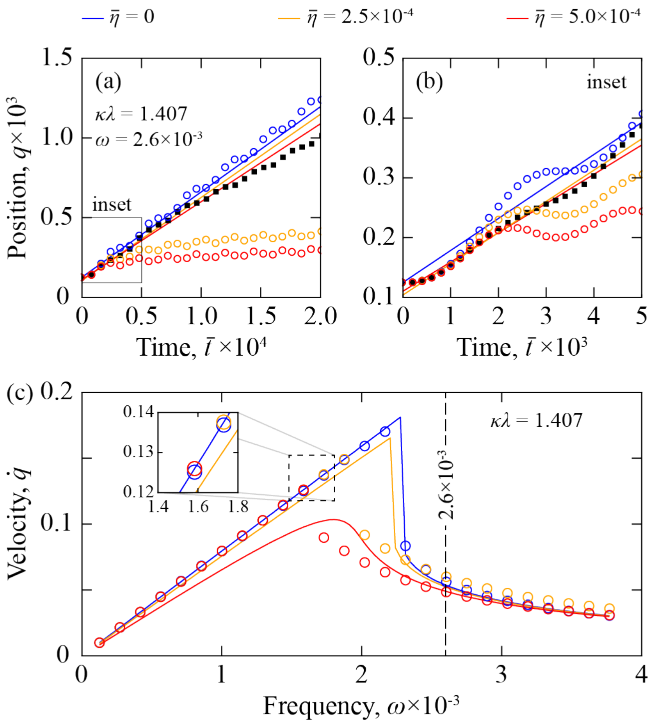

Figure 4.4: Lattices with Space-Time Variable Potential. (a,b) A comparison of theoretically predicted (solid line) and numerically determined soliton position for a continuous sinusoidal modulation, $\bar{v}_j = \bar{V}\sin(\kappa ja+\vartheta-\omega\bar{t})$ (dots), and a pulsed sinusoidal modulation, $\bar{v}_j = \bar{V}\sin(\kappa ja+\vartheta-\omega\bar{t})\mathscr{H}(\mathrm{sgn}[\sin(\omega_\mathrm{s}\bar{t})])$ (squares), with $\bar{V} = 2.5\times10^{-3}$ and $\omega_\mathrm{s} = 2.1\times10^{-3}$. Different damping levels are represented for the continuous sinusoid. Only $\bar{\eta} = 5\times10^{-4}$ is plotted for the pulsed sinusoid. (c) A comparison of theoretically predicted (solid line) and numerically observed (dots) soliton velocities. The numerical velocities are calculated as the average velocity over a period, $T = 2\pi/\omega_\mathrm{r}$.

trapped within a system-level local minimum. The trapped soliton oscillates about the minimum with a frequency determinable by Eq. (4.3) (see SM, Sec. 4.5), causing the region to undergo repeated, autonomous transformations. Fig. 4.3b illustrates the oscillation of the soliton center in a (symmetric) system-level, triangular potential well. Naturally, dissipation alters the oscillation frequency and amplitude over time. Ultimately, the damped soliton settles into the minimum.

As a practical limitation, monotonic potential gradings prevent the construction of arbitrarily long lattices as the potential, ultimately, vanishes. However, a prescribed spatio-temporal variation in the potential manifesting mobile system-level minima may transport a

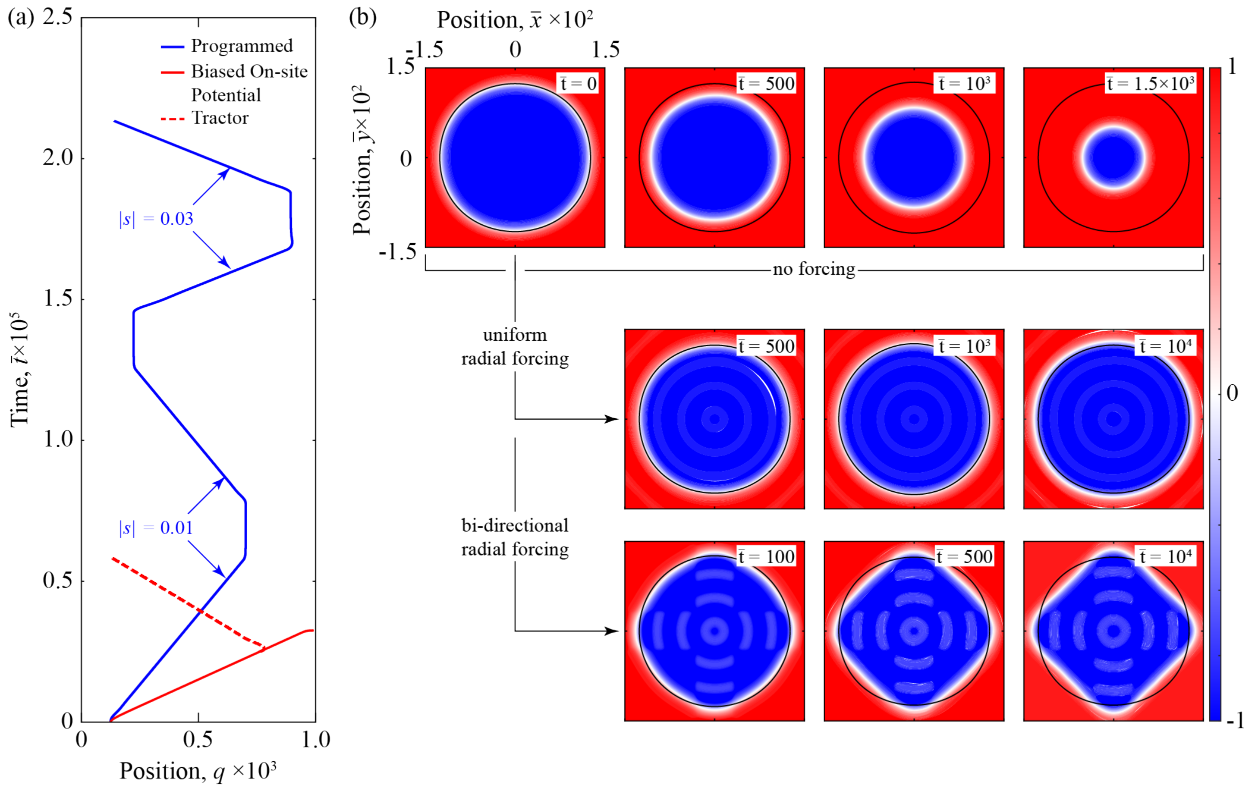

Figure 4.5: Application of Spatio-Temporal Potential Modulation. (a) Soliton response to a programmed modulation and tractor beam ($\bar{V} = 0.0025$) (b) (top row) The collapse of a circular wave front in a 2D lattice in the absence of a potential variation; the expansion (middle row) and shaping (bottom row) of the same initial wave front due to a uniform radial ($\bar{V} = 0.0125$) and directional radial spatio-temporal variation ($\bar{V} = 0.05$) representing a repulsor.

transition wave front with a predictable velocity in lattices of any length.

We consider the response of an initially static transition wave in the proposed lattice where the prescribed displacement modulation, $\bar{v}_j = \bar{V}\sin(\kappa ja + \vartheta - \omega\bar{t})$, is a small-amplitude ($\bar{V} = 2.5\times10^{-3}$) sinusoid of frequency, ω, and wavenumber, κ. Consequently, the lattice possesses multiple potential minima which propagate with velocity $s_\mathrm{p} = \omega/\kappa$ and to which the soliton is drawn, stimulating mobility. In the simulations, one of these minima is initially aligned with the soliton center at $q(0) = q_0$ using the phase shift, ϑ.

Figures 4.4a,b display the simulated soliton response to a continuous sinusoidal modulation for different damping intensities. In each case, the response (dots) exhibits an oscillatory behavior;

however, while the undamped soliton propagates with a constant mean velocity, the damped soliton slows to a near halt, seemingly limiting the utility of the proposed strategy in practical (dissipative) systems. However, alternative modulation waveforms may be more effective in driving the damped soliton. For example, utilizing the pulsed sinusoid, $\bar{v}_j = \bar{V}\sin(\kappa ja + \vartheta - \omega\bar{t})\mathscr{H}(\mathrm{sgn}[\sin(\omega_\mathrm{s}\bar{t})])$ ($\mathscr{H}$ is the Heaviside function), enables long propagation times even at $\bar{\eta} = 5\times 10^{-4}$, a damping intensity which shortened propagation times in the case of the continuous sinusoid. Nevertheless, if the complexity of the modulation is measured by the number of tuning parameters in its mathematical description, then the continuous sinusoid is one of the simplest, and so, to simplify the theoretical analysis and exhibition of spatio-temporal potentials, the continuous sinusoid is applied in the following.

The governing equation corresponding to the sinusoidal modulation is (see SM, Sec. 4.5)

$$\ddot{q}(\bar{t}) = \frac{I}{m_0}\cos(\vartheta - \omega_\mathrm{r}\bar{t}) - \eta\dot{q}(\bar{t}), \tag{4.5}$$

where $\omega_\mathrm{r} = \omega - \kappa\dot{q}$ and, for simplicity, we let $q_0 = 0$. To facilitate an analytical result from integration, we assume ω_r to be, essentially, constant which is approached in the case of small accelerations and times. Integrating Eq. (4.5) yields

$$\begin{aligned}\dot{q}(\bar{t}) = s(\bar{t}) = &\left[\frac{I}{m_0(\bar{\eta}^2+\omega_\mathrm{r}^2)}\right]\\ &\Big(\omega_\mathrm{r}\left[\sin(\vartheta)\mathrm{e}^{-\bar{\eta}\bar{t}} - \sin(\vartheta - \omega_\mathrm{r}\bar{t})\right]\\ &\qquad - \bar{\eta}\left[\cos(\vartheta)\mathrm{e}^{-\bar{\eta}\bar{t}} - \cos(\vartheta - \omega_\mathrm{r}\bar{t})\right]\Big).\end{aligned}$$

Consistent with the small times assumption, we further consider $\mathrm{e}^{-\bar{\eta}\bar{t}} \approx 1$ for several time periods,

$T = 2\pi/\omega_\mathrm{r}$, then the oscillatory behavior predicted by the above relation can be averaged over T to formulate the following cubic equation for the (perhaps transient) soliton mean speed over small times:

$$\begin{aligned} s^3 - 2s_\mathrm{p}s^2 + \left[s_\mathrm{p}^2 + \frac{\bar{\eta}^2}{\kappa^2} + \frac{I}{m_0\kappa}\sin(\vartheta)\right] s \\ - \frac{I}{m_0\kappa^2}\left[\kappa s_\mathrm{p}\sin(\vartheta) - \bar{\eta}\cos(\vartheta)\right] = 0. \end{aligned} \tag{4.6}$$

For sufficiently slow moving modulations, the above polynomial possesses only one real root, $s \leq s_\mathrm{p}$. Conversely, if the potential modulation travels with sufficient speed, there exists three real roots, the smallest of which is observed in simulations. These roots are plotted as solid lines in Figs. 4.4a,b, showing good agreement with the initial transient regions of the simulations, especially in the case $\bar{\eta} = 0$ for which $\mathrm{e}^{-\bar{\eta}\bar{t}} = 1\ \forall \bar{t}$ and s may be interpreted as either the steady-state mean speed or, paradoxically, as the speed over a “transient" period of infinite duration. For the special case of $\bar{\eta} = 0$, the theoretical velocity is the piecewise expression

$$\dot{q} = \begin{cases} s_\mathrm{p}, & s_\mathrm{p} \leq s_\mathrm{c} \\ \frac{1}{2}\left(s_\mathrm{p} - \sqrt{s_\mathrm{p}^2 - s_\mathrm{c}^2}\right), & s_\mathrm{p} > s_\mathrm{c} \end{cases} \tag{4.7}$$

where the critical speed $s_\mathrm{c} = \sqrt{4I\sin(\vartheta)/m_0\kappa}$ separates two kinetic regimes. For $s_\mathrm{p} \leq s_\mathrm{c}$, the speed of the potential modulation is sufficiently slow as to ensure that, as the minimum moves away from the soliton center, the transition wave is able to continuously re-equilibrate and, thus, travel with an identical mean, steady-state velocity, $\dot{q} = s_\mathrm{p}$. Alternatively, in the region $s_\mathrm{p} > s_\mathrm{c}$, the soliton center is outpaced by the minima and, therefore, the transition wave travels at a reduced mean speed, alternately entering and exiting successive lattice-level potential wells. The damped soliton exhibits qualitatively similar behavior, interestingly, leading to faster than predicted propagation for slow moving modulations. These results can be seen in Fig. 4.4c which compares ω-dependent theoretical and numerical results for different damping intensities, exhibiting excellent agreement, especially in the undamped scenario.

In the preceding, we theoretically describe and numerically analyze the physics of solitons in multistable metamaterials subject to spatio-temporal forcing, the result of a commensurate modulation in the elastic potential. In the context of soliton management, such an approach allows for the on-demand control of the kinetics and extent of phase transformations in systems of arbitrary size. To illustrate this ability, in the following, we present three examples of transition wave control. In each case, the spatio-temporal variation in the (on-site) potential stems from prescribed sinusoidal displacements, $\bar{v}_j = \bar{V}\sin(\kappa ja + \vartheta - \omega\bar{t})$.

For the moment, we consider a dissipative ($\bar{\eta} = 10^{-3}$) 1D metamaterial identical to that in Fig. 4.2 with the exception of an additional elastic component, $\bar{k}_\mathrm{X}$, which contributes $\bar{k}_\mathrm{X}\bar{u}^2/2$ to the on-site potential. In one scenario, $\bar{k}_\mathrm{X} = 0$, yielding degenerate ground states which prohibit the self-sustained propagation of transition waves.[59,60] Despite this condition, as shown in Fig. 4.5a, the movements of the soliton center may be programmed by utilizing a potential variation wherein κ and ω are assigned different values for specific time intervals: the soliton either remains static or propagates, including reversing propagation direction and altering propagation speed. In this manner, the kinetics and extent (i.e., position) of the associated phase transformation are controlled. In a second scenario, $\bar{k}_\mathrm{X} = 10^{-6}$ manifests a biased on-site energy landscape which supports the self-sustained, uni-directional propagation of a single soliton mode,[62] rendering the corresponding transformation irreversible. Figure 4.5a plots the position of a transition wave front within the biased system, showing it to move with constant velocity until terminating at the system boundary at $q = 10^3$. However, while in transit, a spontaneous forcing – arbitrarily, initiated at $\bar{t} = 25 \times 10^3$ – stemming from a spatio-temporal potential variation counters the local energy bias and permits the reversal of the soliton propagation direction and, thus, the phase transformation in opposition to the energy minimizing tendency of the unforced system. In this manner, the modulation represents as a tractor.

For the third scenario, we consider a 2D bistable mechanical metamaterial modeled after that introduced in Frazier and Kochmann[61] (see SM, Sec. 4.5) which possesses two degenerate ground states. Within this system, we initiate a circular phase which, subsequently, tends to collapse inward and vanish due to an energy-minimizing, “surface tension" effect related to the wave-front curvature. The snapshots in the first row of Fig. 4.5b depict this process. However, as indicated in the second row of Fig. 4.5b by the slight increase in the circular phase diameter, a radially directed spatio-temporal potential modulation is able to maintain the circular phase by repelling the wave front. Moreover, as illustrated in the third row, by directing the sinusoidal modulation along specific axes, the shape of the wave front can be deformed away from circular on demand. In opposing the natural tendency of the circular phase to collapse, the modulation acts as a repulsor.

4.5 Conclusion

In summary, this letter interprets (topological) solitons as Newtonian particles and applies the associated dynamics concepts to their prediction and control in multistable metamaterials. It was shown that spatio-temporal modulations of the metamaterial elastic potential stimulates soliton motion in a manner similar to the electric/magnetic fields in solid state systems. This represents means to manipulate the post-fabrication metamaterial phase transformation kinetics and phase distribution on demand and, potentially, remotely; a capability which supports the adoption of multistable metamaterials in applications demanding multi-functionality. The theoretical findings are supported by the simulation results of a representative metamaterial. The method provides a viable alternative to using defects, to stabilize phase distribution in 2D, as demonstrated by the example preventing collapse of a circular phase in a modified automimetic lattice. Nevertheless, the particle interpretation restricts the forcing in order to avoid relativistic effects. In addition, without a check-and-amend scheme, the accuracy of theoretical predictions may diminish in time, especially when potentials possess a high degree of spatial variability, resulting in distortion of the soliton profile.

Supplementary Material

See Supplementary Material[4] for additional results, detailed derivations and calculation procedures.

Declaration

Chapter 4, in full, is a reprint of the material as it appears in V. Ramakrishnan and M. J. Frazier, "Transition waves in multi-stable metamaterials with space-time modulated potentials", *Appl. Phys. Lett.*, **vol. 117**, p. 151901, October 2020. The dissertation author is the primary author of this paper.

---

[4] `https://aip.scitation.org/doi/suppl/10.1063/5.0023472`

Chapter 5

Periodic Pattern Formation in Active Architected materials

5.1 Abstract

Nature is replete with phenomena such as self-organization in biological and chemical systems that uniquely require the system to exist far from equilibrium. The complexity of the internal processes from which the non-equilibrium response emerges restricts the theoretical understanding to that derived from phenomenological models, whose general form resembles elastodynamic equations, albeit with a forcing that arises from non-reciprocity in the state variables. Motivated by this observation, the quality of elastodynamic models to derive directly from first principles (i.e., Newtons laws), and the potential to control non-equilibrium behavior, we study the non-equilibrium response of an architected material comprising active elements (i.e., motors)

that, in addition to the elastic coupling typical of mechanical systems, enforce non-reciprocity via electric coupling. The system exhibits pattern formation in the displacement field. We develop an analytical model to study the material dynamics and compare the theoretical, numerical, and experimental results, to demonstrate a predictive capability.

5.2 Introduction

There exist fascinating systems in the universe, cutting across multiple length and time scales that self-organize themselves into interesting patterns (e.g., solar granulation on the surface of the sun,[164] formation of sand dunes,[165] spiral patterns in chemical reactions[166]), that primarily arise due to an interplay between the underlying diffusion and energy dissipation mechanisms, constantly driving these systems away from the thermodynamic equilibrium. These non-equilibrium systems have fascinated the research community and prompted development of theoretical models to gain deeper insights into these processes. The development of a phenomenological reaction-diffusion model,[167] has been a notable effort in this regard that has proven effective in modelling the non-equilibrium behavior in certain biological[168] and chemical systems.[166] Extensive theoretical studies under a diverse set of diffusion and reaction conditions[169–172] have revealed the presence of unique non-equilibrium patterns, e.g., spatially periodic instabilities (i.e., Turing patterns[173]), spatio-temporal oscillations (e.g., spiral waves[170,174]) and, stationary periodic patterns,[175] that have since been identified as the basis for cardiac rhythm,[176] spot-formations in marine creatures,[168] cell growth and morphogenesis,[173,177] and vegetation distribution in water scarce environments.[178]

Analyzing from a mechanics and materials perspective, we notice a correspondence between the components of the phenomenological reaction-diffusion equation and the elastodynamic equation governing elastic wave propagation in materials.[179,180] Furthermore, replicating the non-equilibrium behavior seen in reaction-diffusion systems, on an architected material platform can allow emergence of novel material morphologies for customizing the material behavior and expand their functionality. Previous efforts to control architected material behavior have employed creative design strategies, e.g., incorporating active elements (e.g., piezo-electrics[41,45,47]), geometric instability[38,132] or multi-stability,[9,67,69,70] contributing to the emergence of a post-fabrication tuning capability, opening up new avenues to create functional devices such as acoustic wave guides,[12,43] acoustic diodes,[181,182] mechanical logic gates[183] and soft robots.[184,185] Although, the fundamental behavior in all these designs emerges from the inherent tendency to minimize the potential energy, restricting the material operation around the thermodynamic equilibrium. Therefore, motivated by the non-equilibrium, self-organization behavior observed in certain biological and chemical systems, the resemblance of the elastodynamic wave equation to the phenomenological reaction-diffusion equation, the quality of elastodynamic models to derive directly from first principles (i.e., Newtons laws) rather than phenomenologically, and the potential to control non-equilibrium behavior, we propose an architected material capable of replicating Turing reaction-diffusion dynamics[173] in a mechanical setting. The emergent class of non-equilibrium materials can be conducive to realizing beneficial functionalities such as self-morphing autonomous surfaces.

In this chapter, we construct an active architected material whose dynamics are analogous to a chemical reaction-diffusion system. The architected material utilizes a programmable, non-reciprocal electrical interaction between two distinct mono atomic chain of rotating units to realize periodic, non-equilibrium rotational patterns akin to the periodic patterns observed in

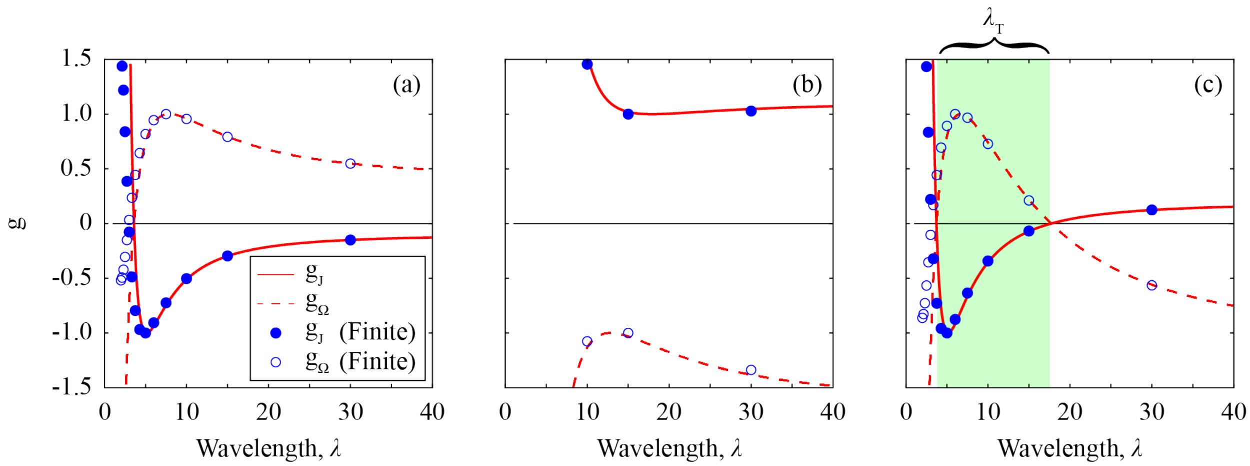

Figure 5.1: $g_J(\lambda) = \mathrm{Det}(\mathbf{J})/|\min[\mathrm{Det}(\mathbf{J})]|$ (Eq. (5.6)) and $g_\Omega(\lambda) = \Omega_1/|\max(\Omega_1)|$ plots for an (a) unconditionally unstable system, (b) unconditionally stable system, and (c) conditionally stable system.

chemical and biological systems. We perform analytical and numerical studies and experimentally demonstrate a robust, multi-wavelength pattern forming ability of our architected material when subject to different initial perturbations from the thermodynamic equilibrium.

5.3 Results

5.3.1 The Turing Instability

$$u_{,t} = \Delta u + R_u(u,v)$$

$$\gamma v_{,t} = d\Delta v + R_v(u,v) \tag{5.1}$$

Eq. (5.1)[170] represents a non-dimensional, phenomenological form of a reaction-diffusion model consisting of two reagents - the activator and the inhibitor, respectively, with concentrations, u and v. The functions R_u and R_v representing the reaction dynamics for the respective reagents, are chosen such that presence of u facilitates a chemical reaction leading to an increase in concentration of both u and v while, the presence of v impedes the production of reagents u and v. The coefficients d and γ quantify the relative diffusion and temporal dynamics of the activator-inhibitor reagent pair. The fundamental bedrock of the non-linear, self-organizing behavior arising in biological and chemical systems in nature is attributed to this discrepancy in the reaction-diffusion dynamics between the underlying reagents. A variety of interesting non-equilibrium behavior[170, 173–175] arise for different range of d and γ. In this chapter, we focus on the dynamics of a reaction-diffusion system involving faster diffusion and temporal effects of the inhibitor, i.e., $d > 1$ and $\gamma < 1$ to study and replicate the emergent spatial periodic instabilities[167, 173] in our mechanical system.

Consider a thermodynamic equilibrium, (u_0, v_0) such that, the reaction functions, $R_u(u_0, v_0) = R_v(u_0, v_0) = 0$. For small perturbations about this equilibrium $[u_0 + \tilde{u}(\mathbf{x}, t), v_0 + \tilde{v}(\mathbf{x}, t)]$, taking a Taylor expansion of functions, R_u and R_v, Eq.(5.1) can be rewritten in the matrix form :

$$\dot{\mathbf{U}} = \mathbf{D}\Delta\mathbf{U} + \mathbf{R}\mathbf{U} \tag{5.2}$$

where,

$$\mathbf{U} = \begin{bmatrix} \tilde{u} \\ \tilde{v} \end{bmatrix}, \ \mathbf{D} = \begin{bmatrix} 1 & 0 \\ 0 & d/\gamma \end{bmatrix}, \ \mathbf{R} = \left.\begin{bmatrix} R_{u,u} & R_{u,v} \\ R_{v,u}/\gamma & R_{v,v}/\gamma \end{bmatrix}\right|_{(u_0, v_0)}$$

represent the perturbed concentration vector, diffusion matrix and the reaction jacobian matrix, respectively.

A spatial Fourier transform of Eq. (5.2) yields:

$$\dot{\tilde{\mathbf{U}}} = (\mathbf{R} - \kappa^2\mathbf{D})\tilde{\mathbf{U}} \tag{5.3}$$

where, $\kappa = 2\pi/\lambda$, denotes the spatial frequency, corresponding to a non-dimensional wavelength, λ. Assuming an *ansatz*, $\tilde{\mathbf{U}} = \tilde{\mathbf{U}}(0)e^{\Omega t}$ for Eq. (5.3), generates the eigenvalues:

$$\Omega_{1,2}(\kappa) = \frac{\mathrm{Tr}(\mathbf{J}) \pm \sqrt{[\mathrm{Tr}(\mathbf{J})]^2 - 4\mathrm{Det}(\mathbf{J})}}{2} \tag{5.4}$$

where, $\mathbf{J} = \mathbf{R} - \kappa^2\mathbf{D}$, and $\Omega_1 > \Omega_2$. The eigenvalues, $\Omega_{1,2}$ determine the nature of stability of the thermodynamic equilibrium, (u_0, v_0) to an applied initial perturbation of periodicity, κ. Depending on the choice of system parameters, the above analysis can yield three possible eigenvalue pairs:

- $\Omega_1 > 0 \; \forall \; \lambda \in \mathbb{R}^+$ - an unconditionally unstable system (Fig. 5.1a),
- $\Omega_{1,2} < 0 \; \forall \; \lambda \in \mathbb{R}^+$ - an unconditionally stable system (Fig. 5.1b),
- $\Omega_1 > 0, \; \Omega_2 < 0 \; \forall \; \lambda \in \lambda_\mathrm{T}$ and $\Omega_{1,2} < 0$ otherwise - conditionally stable system (Fig. 5.1c).

Perturbing an unconditionally unstable system away from the thermodynamic equilibrium can lead to random pattern formation or oscillations in reagent concentrations, depending on the reaction-diffusion parameters and the characteristics of initial perturbation. While, an unconditionally stable system exhibits an extremely stable response to perturbations, where the system recovers the equilibrium reagent concentrations in the steady state. Both these systems present scenarios with no further interesting dynamics to explore. However, when the thermodynamic equilibrium is conditionally stable, perturbations of certain wavelengths, λ_T are able to trigger an instability, leading to the emergence of new non-equilibrium stable spatial concentration gradients. These instabilities are periodic in nature and are referred to as Turing patterns.[173] The conditional stability of the thermodynamic equilibrium requires the reaction and diffusion terms to satisfy the conditions:

$$\mathrm{Tr}(\mathbf{R}) < 0, \tag{5.5a}$$

$$\mathrm{Det}(\mathbf{R}) > 0, \tag{5.5b}$$

$$R_{v,v} + dR_{u,u} > 2\gamma\sqrt{\mathrm{Det}(\mathbf{D})\mathrm{Det}(\mathbf{R})}, \tag{5.5c}$$

Eq. (5.5)a,b ensure the existence of a homogeneous, thermodynamic equilibrium (u_0, v_0), i.e., $\Omega_{1,2}|_{\kappa=0} < 0$. Eq. (5.5)c ensures a system instability, i.e., $\Omega_1 > 0$ for certain wavelengths, λ_T by setting:

$$\mathrm{Det}(\mathbf{J}) = \kappa^4 \mathrm{Det}(\mathbf{D}) - \left(\frac{R_{v,v} + dR_{u,u}}{\gamma}\right)\kappa^2 + \mathrm{Det}(\mathbf{R}) < 0 \tag{5.6}$$

At the onset of instability, regions perturbed to a higher activator concentration, u emerge as active reaction sites where, the reaction dynamics lead to an increase in the concentrations of both reagents u and v. Simultaneously, reagent v by virtue of a higher diffusion rate readily spreads to the neighbouring sites, inhibiting the chemical reactions in the immediate vicinity. These reaction-diffusion dynamics of the reagents compete with each other and, over time, isolated regions with higher and lower concentrations of u and v emerge, ultimately halting the dynamics of the system, creating a stationary, periodic distribution of reagent concentrations. The periodicity of these emergent Turing patterns mirror the dominant wavelength involved in the initial perturbation. Therefore, a single wavelength perturbation yields a Turing pattern of the corresponding wavelength while perturbations comprising multiple Fourier wavelength components, result in a Turing pattern corresponding to the most unstable wavelength having the highest positive eigenvalue. However, studies on 2D/3D reaction-diffusion systems have shown that boundary conditions and initial conditions/perturbations[169, 171, 186] can also play a crucial role in influencing the pattern formation dynamics.

Inspired by this on-demand pattern formation ability supported by these activator-inhibitor systems, we attempt to replicate the underlying mechanisms in a customizable mechanical system: an architected material with mechanical and electrical components. The electrical system consisting of motors and a control system plays a vital role in applying a non-reciprocal torque on the lattice sites, ensuring conditional stability of the material. The material design allows tunable domain distributions in a kinematic degree of freedom, i.e., rotational displacement/phase. The following sections will analytically study the architected material behavior using a mass-spring-damper model and validate the analytical predictions through numerical and experimental investigations.

5.3.2 Architected Material

Fig. 5.2 depicts the architected material experimental setup and the equivalent mass-spring-damper model. The two parallel arrays of 3D printed rotating cylinders mounted onto onsite electric DC motors in Fig. 5.2a-i, represent the activator and inhibitor lattice sites. Each lattice site is elastically linked to its intra-layer neighbors via silicone bands (white), within both layers. The elastic response of these bands are quantified using non-linear torque functions, $\tau_\alpha(\alpha)$ and $\tau_\beta(\beta)$, respectively, based on Instron tests (see Fig. 5.5) and subsequently incorporated into our analytical and numerical model. The motors associated with each lattice site are also equipped with rotary encoders that relay the motor orientation data to an external electrical control system. Each unit cell, i.e., activator-inhibitor pair (α_j, β_j) is associated with a unique electrical control system, i.e.,

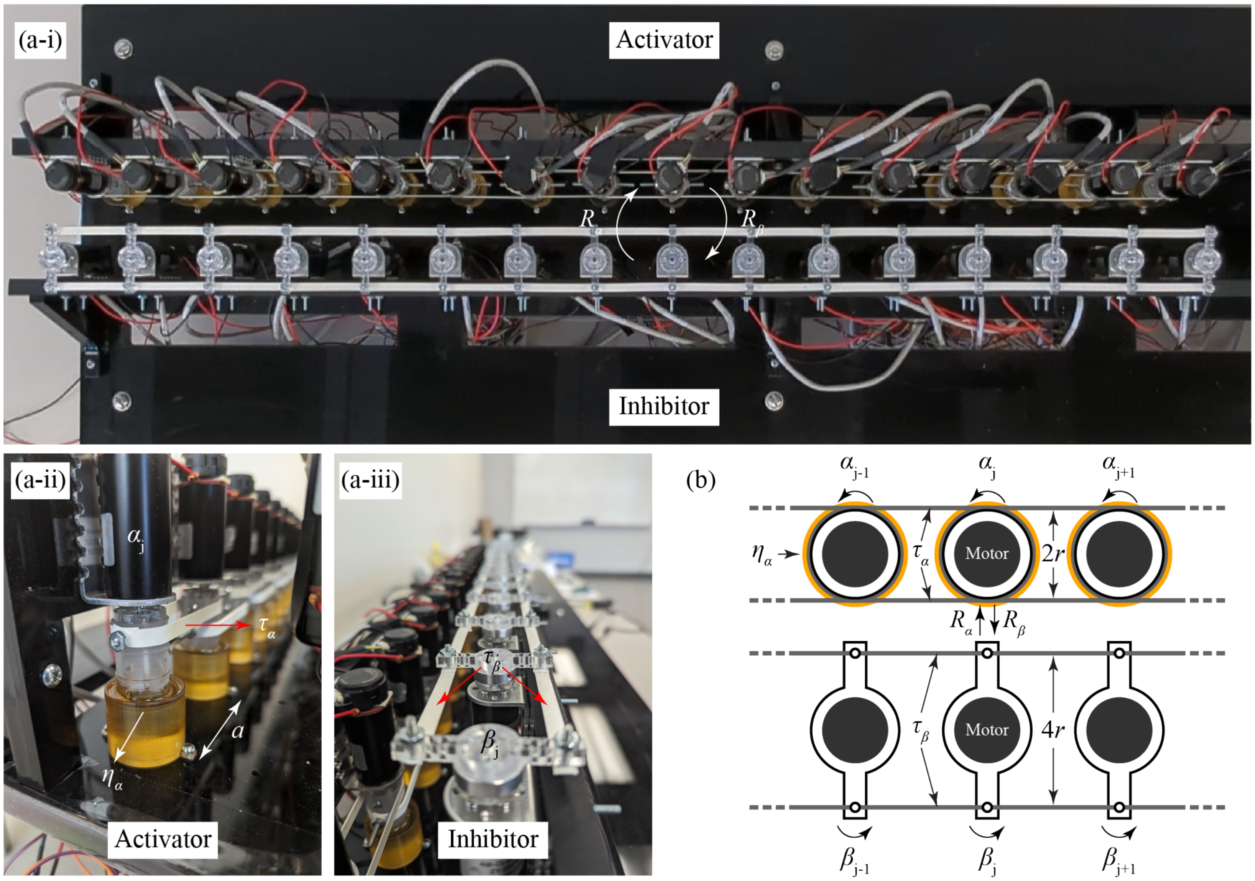

Figure 5.2: Architected Material. (a-i) Top view of the experimental setup showing the activator-inhibitor motor arrangements, (a-ii) Zoomed in view of an activator lattice site, (a-iii) Zoomed in view of an inhibitor lattice site, (b) Equivalent reduced order mass-spring-damper architected material model.

a printed circuit board (PCB) consisting of a micro-controller and two motor drivers (see Methods and Fig. 5.10). The micro-controller receives the encoder data from the activator-inhibitor motors, calculates the external feedback torques $R_\alpha(\alpha,\beta)$ and $R_\beta(\alpha,\beta)$, and directs the motor drivers to supply the proportional voltage across the motor terminals. The PCB associated with each unit cell functions independently and operates the activator-inhibitor motors on the above feedback loop continuously.

Each component of the experimental setup can be mapped onto an equivalent inertial, elastic or viscous mechanical element allowing us to develop a reduced order mass-spring-damper model shown in Fig. 5.2b. Consequently, the equations of motion for the j^{th} unit cell of the architected material can be formulated as:

$$\eta_\alpha \alpha_{j,t} = -[\tau_\alpha(\alpha_j, \alpha_{j-1}) + \tau_\alpha(\alpha_j, \alpha_{j+1})]... \\ + R_\alpha(\alpha_j, \beta_j) - I_\alpha \alpha_{j,tt}, \tag{5.7a}$$

$$\eta_\beta \beta_{j,t} = -[\tau_\beta(\beta_j, \beta_{j-1}) + \tau_\beta(\beta_j, \beta_{j+1})]... \\ + R_\beta(\alpha_j, \beta_j) - I_\beta \beta_{j,tt}, \tag{5.7b}$$

where, I_α, τ_α and I_β, τ_β represent the rotational mass moment of inertia and the elastic interaction torque function, respectively, on the j^{th} activator and inhibitor lattice sites and functions:

$$R_\alpha(\alpha_j, \beta_j) = k_{\alpha\beta}(\beta_j - \alpha_j) - \psi'(\alpha_j) - \sigma\beta_j, \tag{5.8a}$$

$$R_\beta(\alpha_j, \beta_j) = k_{\alpha\beta}(\alpha_j - \beta_j), \tag{5.8b}$$

capture the torque contributions of the electric motors on the activator and inhibitor lattice sites, respectively. Both functions consist of a reciprocal, inter-layer linear interaction spring torque proportional to stiffness, $k_{\alpha\beta}$. Although, R_α contains two additional terms: an on-site non-monotonic torque, $\psi'(\alpha_j)$ with roots $\alpha = 0, \pm\alpha^*$, and a linear feedback torque based on the inhibitor rotation, β_j and proportional to coefficient, σ, rendering the cumulative interaction between the layers, non-reciprocal. The feedback torques in Eq. (5.8) are specifically chosen to mimic the qualitative features of the reaction terms in the Fitz-Nagumo reaction-diffusion model[187–190] in a mechanical setting. The viscous effects on both layers are quantified by viscous coefficients η_α and η_β. Please refer to Methods and Appendix for a detailed description and analysis of the architected material components.

Overall, Eq. (5.7) closely resembles the phenomenological reaction-diffusion equation (Eq. (5.1)) *sans* the inertial terms. Hence, to maintain the validity of the reaction-diffusion stability analysis (Eq. (5.5)), the rotational masses on the activator layer are suspended in a highly viscous fluid, i.e., honey to ensure the dominance of viscous effects on the temporal dynamics of the architected material, minimizing inertial interference. In addition, suspending the activator lattice in honey also distinguishes the viscous dynamics, γ between the layers. In line with this assumption, the inertial terms are neglected in our theoretical and numerical analysis from hereon.

5.3.3 Numerical and Experimental Results

Taking the essential conditions from Eq. (5.5) into consideration, we identify and use parameters - $k_\beta/k_\alpha = 3.12$, $\gamma = 0.1$, $\alpha^* = \pi/2$, $k_1 = 0.06$, $k_2 = -0.06$, $\sigma = 0.072$, $k_{\alpha\beta} = 0.02$ (see Appendix), that are conducive to mechanical Turing pattern formation in our architected material. Numerical and experimental tests are now performed for different initial perturbations and the steady state data from both sources are compared and analyzed.

Fig. 5.3b-c plot the numerical simulation data (solid) and the experimental encoder data (circles) for two different initial perturbations applied to the thermodynamic equilibrium state shown in Fig. 5.3a, as rotational impulse loads to the activator layer. As expected from Fig. 5.1c, perturbing the architected material from the thermodynamic equilibrium, $\alpha_0 = \beta_0 = 0$, produce mechanical Turing patterns of wavelengths, $\lambda = 15$ and $\lambda = 10$ within the Turing wavelength regime. Disturbing the thermodynamic equilibrium state, simultaneously triggers an elastic interaction between the intra-layer neighbors and a non-reciprocal inter-layer interaction,

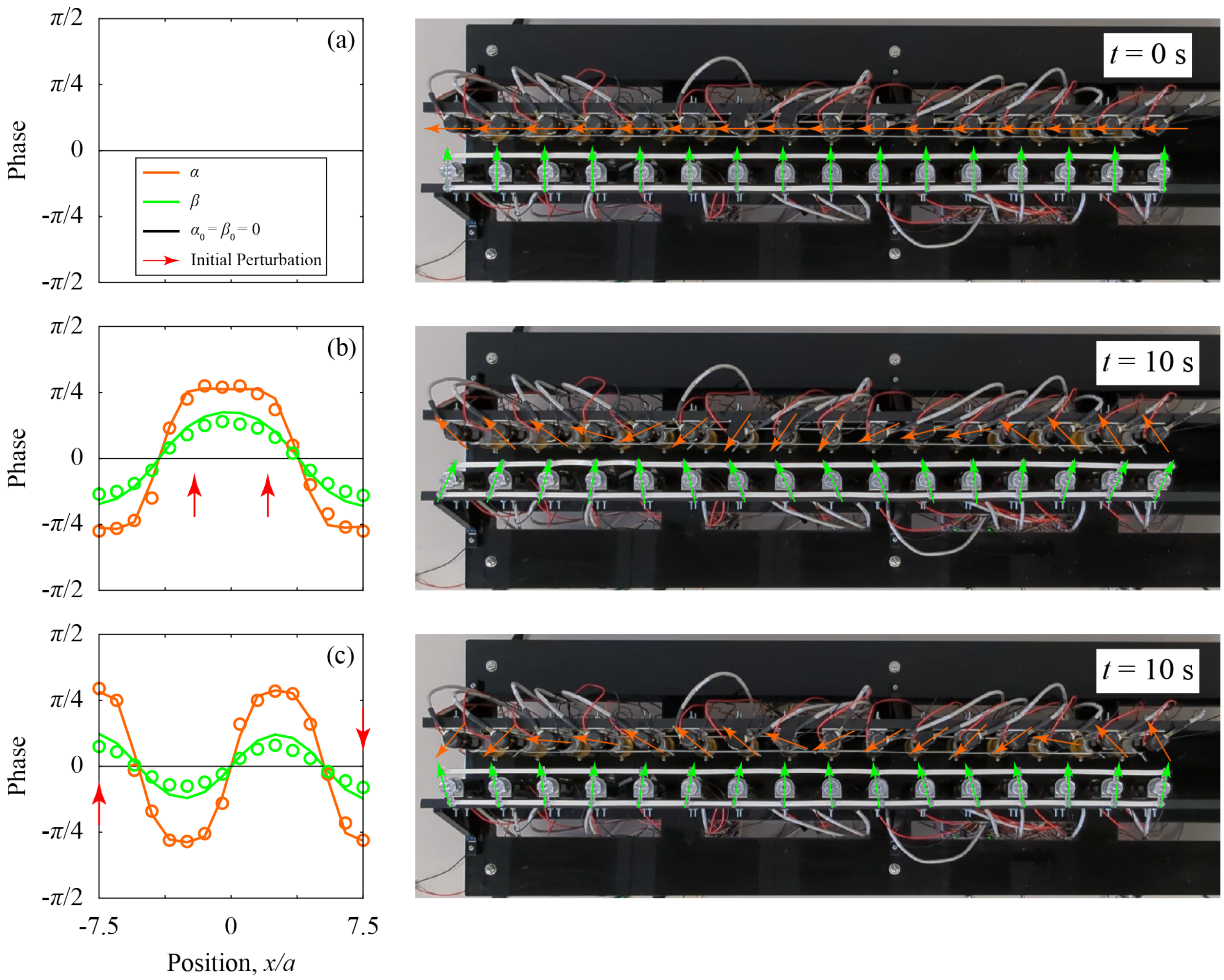

Figure 5.3: Mechanical Turing Patterns in an Architected Material with 16 unit cells. (a) Thermodynamic equilibrium orientation, $\alpha_0 = \beta_0 = 0$ for the architected material. Comparison of numerical (solid) and experimental (circles) motor orientations for (b) a CCW-CCW perturbation at $j = 6, 10$, resulting in a steady state periodicity of $\lambda = 15$, (c) a CCW-CW perturbation at $j = 1, 16$, resulting in a steady state periodicity of $\lambda = 10$.

leading to a transient deformation in both the activator and inhibitor layers. The competition between the non-reciprocal effects to localize the elastic deformation and the silicone bands to spread-out the elastic deformation causes the rotational phase distribution to evolve and attain a new, non-equilibrium steady state configuration.

When the activator boundary lattice sites, $j = 6, 10$ are subject to a counter clockwise - counter clockwise (CCW-CCW) rotational initial perturbation, the numerical simulation predicts a steady state phase distribution of periodicity, $\lambda = 15$. Fig. 5.3b contrasts the numerical and experimental data for this scenario showing an excellent correlation. Alternately, Fig. 5.3c plots the numerical and experimental data, when the activator boundary lattice sites, $j = 1, 16$ are subject to a counter clockwise - clockwise (CCW-CW) rotational initial perturbation. The experimental data manifests a periodicity, $\lambda = 10$ in the rotational phase distribution, closely resembling the numerical prediction. The experimental setup was subjected to multiple tests and consistently produced a well correlated output for the respective initial conditions, establishing the consistency and accuracy of our architected material design. The multi-wavelength, mechanical Turing pattern formation in our architected material serves as a proof of concept and, establishes a template to replicate complex dynamics observed in natural systems on a customizable architected material platform.

5.4 Conclusion

We propose an active metamaterial design capable of incorporating the rich spatio-temporal dynamics previously found only in chemical and biological reaction-diffusion type systems. This provides an interesting and unique opportunity to understand a ubiquitous, complex natural phenomenon in detail and explore its utility in mechanical systems. In this effort, we numerically analyze and experimentally verify the formation of Turing patterns in a spring-mass system with active feedback (electrical).

5.5 Methods

5.5.1 Stability analysis

The homogeneous equilibrium for the architected material (Eq. (5.7)) is calculated as $(\alpha_0, \beta_0) = (0,0)$ (see Appendix). Linearizing the dynamics around the homogeneous equilibrium produces a diffusion matrix, **D** and reaction Jacobian matrix, **R** for the architected material, analogous to those of the phenomenological reaction-diffusion model:

$$\mathbf{D} = \begin{bmatrix} k_\alpha & 0 \\ 0 & k_\beta/\gamma \end{bmatrix}, \mathbf{R} = \begin{bmatrix} -k_{\alpha\beta} - \psi''(0) & k_{\alpha\beta} - \sigma \\ k_{\alpha\beta}/\gamma & -k_{\alpha\beta}/\gamma \end{bmatrix},$$

where, $\gamma = \eta_\beta/\eta_\alpha < 1$, and, $k_\alpha = \tau_{\alpha,\alpha}(0)$ and $k_\beta = \tau_{\beta,\beta}(0)$ denote the linearized torsional interaction stiffness around the equilibrium in the respective layers. Utilizing the above matrices in Eq. (5.5), we arrive at the conditions essential for conditional stability of the architected material and choose the experimental parameters accordingly (see Appendix).

5.5.2 Mechanical components

The active architected material in Fig. 5.2 consists of two layers (α_j, β_j) of 3D printed rotating cylinders coupled to neighbouring sites via elastic bands and electrical circuits with a lattice parameter, $a = 60$mm. Each layer consists of customized 3D printed cylinders (see Fig. 5.4) with non-contact coupling between the layers via electrical circuit and motors. The coupling between adjacent unit cells is purely mechanical via elastic bands. In this section, we provide details of the mechanical and electrical setup used in the experiment.

Each lattice site in the activator and inhibitor layer (see Fig. 5.4), consists of (i) a 3D printed cylinder (Veroclear, Connex3 3D printer), (ii) a 3D printed custom mounting hub (Veroclear, Connex3 3D printer) connecting the cylinder and motor shaft, (iii) an aluminium bracket to fix the motor onto the vertical support (Pololu Item #2676), (iv) a Brushed DC coreless motor (Assun Motors, AM-CL2242MAN 1205), (v) an optical encoder attached to the motor rear shaft (Anaheim Automation, ENC-A4TS-0100-079-M).

The activator cylinders have a radius, $r = 10$ mm and height, 40 mm. The silicone bands on the activator layer are secured onto the cylindrical surface via 1-1/2 inch, $\#4-40$ machine screws and hex-nuts. On the other hand, the inhibitor cylinders are of a shorter height, 5 mm with a circular center core, to be compatible with the mounting hubs and extended arms. The silicone bands on the inhibitor layer are secured onto these extended arms via 1/2 inch, $\#4-40$ machine screws and hex-nuts at a radial distance, $2r$ to provide a higher effective torque (see Fig. 5.6).

The silicone rubber bands used on the activator and inhibitor layers are hand cut from the Food Industry High-Temperature Silicone Rubber Sheet, Product #86045K76 and #86045K58 procured from McMaster Carr. The elastic bands are cut to dimensions $83\text{mm} \times 6\text{mm} \times t$ and $55\text{mm} \times 6\text{mm} \times t$ for the activator and inhibitor layers, respectively, where, $t = 1/32''$. The length is chosen as, $L_\alpha = 83\text{mm}$ and $L_\beta = 55\text{mm}$ to ensure an initial pre-stretch around 10%.

The complimentary pair of elastic bands between the interacting cylinders ensure that one of the elastic bands always remains in tension as the cylinders rotate, applying an equal and opposite elastic restoring torque on the connected cylinders. To increase the robustness of the numerical model and accurately capture the softening elastic behavior of the silicone bands, we perform Instron tests and evaluate the non-linear 3^{rd} order polynomial approximations, $f_\alpha(\alpha)$ and $f_\beta(\beta)$ (see Fig. 5.5) for the elastic response of the silicone bands. These functions are then utilized to calculate the elastic interaction torques, $\tau_\alpha(\alpha)$ and $\tau_\beta(\beta)$.

Finally, to increase the discrepancy in the reaction-diffusion dynamics between the layers, the activator cylinders are suspended over cups containing honey. The honey ensures an increased viscous resistance to the cylinder rotation on the activator layer, playing a crucial role in ensuring conditional stability of the thermodynamic equilibrium and the realization of rotational Turing patterns in the system. The viscous coefficient of honey is quantified by performing motor speed tests in the presence of honey (see Fig. 5.9).

5.5.3 Electrical components

Control System: The control system for the inter-layer coupling between cylinders α_j and β_j consists of (i) external power supplies (ii) an optical encoder attached to the motor rear shaft (ENC-A4TS-0100-079-M), (iii) a micro-controller (Seeeduino XIAO), (iv) two brushed DC motor drivers (Pololu DRV8874), and (v) two Brushed DC coreless motor (AM-CL2242MAN 1205).

Power Supply: We utilize two kinds of external power supplies - (1) a 5V-5A DC (Pololu Item #1462) power supply to power the encoders, micro-controllers and drivers and, (2) a 9V-30A DC power supply consisting of six 9V-5A DC (Pololu Item #1465) power supplies connected in parallel to power the electric motors.

Optical Encoders: The optical encoder, ENC-A4TS-0100-079-M attached to the Brushed DC coreless motor, provides a precision of 400 counts per revolution (CPR), which translates to an angular resolution 0.0050π rad. An external 5V DC power supply powers all encoders. Each encoder outputs a pair of binary signals via the ENC A and ENC B terminals (see Fig. 5.10) that allow the respective unit cell micro-controller to process angular position of the attached motor.

Micro-controller: The Seeeduino XIAO micro-controller chip of a given unit cell, receives the encoder data from both the activator and inhibitor electric motors and relays a PWM (pulse-width modulation) and direction signal to the motor drivers based on the feedback functions R_α and R_β. The micro-controller is also powered by the external 5V DC power supply. Even though, the micro-controllers in each unit-cell don't need to be connected to an external computer to function, each micro-controller is connected to an $\mathrm{I}^2\mathrm{C}$ bus that relays the encoder data to a pair of central micro-controllers connected to a computer (see Fig. 5.10). This data bus enables the collection and graphical visualization of the steady state encoder data from each lattice site after the system forms rotational Turing patterns.

Motor Drivers: The DRV8874 motor drivers, intake a SLP-PMODE input from the 5V DC power supply and a VIN-GND input from a 9V DC power supply. The SLP-PMODE input activates the motor drivers while the VIN-GND input is stepped down to the appropriate voltage level by the motor driver, based on the micro-controller PWM and direction signal input and supplied across the DC motor power terminals. The DRV8874 drivers are able to supply a maximum continuous current of 2.1A at stall.

Electric DC Motors: The Brushed Coreless DC motors, AM-CL2242MAN 1205 are rated for a maximum stall torque, $\tau = 90$ mNm at 12V and a stall current of 4.3A. However, since the motor driver DRV8874 is rated for a 2.1A continuous maximum current, we restrict the motor supply voltage at 5.86V and stall torque at 44 mNm via the micro-controller, to ensure a stall current below 2.1A at all times and avoid any electrical damage.

Software: An Arduino software code is uploaded to each Seeeduino XIAO micro-controller to realize the feedback torque on the activator and inhibitor layers. The software code directs the micro-controller of a given unit cell, j to receive the angular positions α_j and

β_j, calculate the values $R_\alpha(\alpha_j, \beta_j)$ and $R_\beta(\alpha_j, \beta_j)$ and relay the proportional levels of PWM and direction signals to the motor drivers and direct the drivers to supply the appropriate voltage across the motor terminals.

5.5.4 Calibration and Measurements

The elastic non-linear resistance, f_α and f_β of the silicone bands are quantified by Instron tests. The detailed analysis and calculations of subsequent torque functions are elaborated in the Appendix.

The Voltage, $\mathrm{V_{in}}$ - no load speed, ω_{NL} response of the brushed coreless DC motor is also tested at different applied voltages and verified with the parameters listed in the manufacturer data sheet. Similar tests are used to quantify the viscous coefficient of honey, η_α used a dissipative mechanism in the experiment. The $\mathrm{V_{in}}$ - ω response in the presence of honey, is contrasted with the no load motor data to quantify the viscous torque, τ_{visc} as a function of motor speed. The test data reveals a linear increase in τ_{visc} with ω allowing us to quantify the viscous effects of honey as the slope of this curve:

$$\eta_\alpha = \frac{\mathrm{d}\tau_{\mathrm{visc}}}{\mathrm{d}\omega},$$

A detailed analysis of the motor test data is available in the Appendix.

Acknowledgements

We would like to specially acknowledge and thank Dr. S. Roberts, Mr. I. Richardson and Mr. C. Cassidy for their skillful technical assistance in conceptualizing and building the experimental setup. We thank Prof. N. Boechler, Prof. J. Friend, and Prof. N. Gravish for their insightful discussions. We also thank H. Tian for his assistance in configuring the initial Arduino control setup. This work was supported by the Hellman fellowship and start-up funds provided by the University of California.

Appendix

Architected material unit cell

Fig. 5.4 shows an image of the assembled architected material unit cell and labels the individual components constituting the lattice sites. Each lattice site in the activator and inhibitor layer, consists of (i) a 3D printed cylinder (Veroclear, Connex3 3D printer), (ii) a 3D printed custom mounting hub (Veroclear, Connex3 3D printer) connecting the cylinder and motor shaft, (iii) an aluminium bracket to fix the motor onto the vertical support (Pololu Item #2676), (iv) a Brushed DC coreless motor (Assun Motors, AM-CL2242MAN 1205), (v) an optical encoder attached to the motor rear shaft (Anaheim Automation, ENC-A4TS-0100-079-M).

The activator cylinders have a radius, $r = 10$ mm and height, H = 40 mm. On the other hand, the inhibitor cylinders are of a shorter height, H = 5 mm and have two diametrically opposite extended arms with spring connection points at a radial distance of $2r$ from the center. The silicone bands on the inhibitor layer are secured onto these extended arms at a radial distance, $2r$ to provide a higher effective torque.

The silicone rubber bands used on the activator and inhibitor layers are hand cut from Food Industry High-Temperature Silicone Rubber Sheet, Product #86045K76 and #86045K58 procured from McMaster Carr. The elastic bands are cut to dimensions 83mm $\times$ 6mm $\times\, t$ and 55mm $\times$ 6mm $\times\, t$ for the activator and inhibitor layers, respectively, where, $t = 1/32''$ denotes the thickness of the silicone sheets. The length is chosen as, $L_\alpha = 83$mm and $L_\beta = 55$mm to ensure an initial pre-stretch around 10% on both layers.

Non-linear softening elastic behavior

Formulating the tensile resistance of the silicone bands as a linear spring force would fail to capture the softening material response over an extended deformation range. Hence, we perform tensile tests on multiple identical silicone bands using the Instron to characterize their non-linear force-displacement behavior. This data is averaged for four tests and plotted for reference in Fig. 5.5a,b, reinforcing a softening elastic response. The silicone bands are now integrated into our numerical model as non-linear springs whose force-displacement function is modelled as a 3rd order polynomial approximation of the Instron data:

$$f_\alpha(\delta) = 0.28 + 268.08\delta - 8817.84\delta^2 + 123843.17\delta^3, \tag{5.9a}$$

$$f_\beta(\delta) = 0.19 + 164.96\delta - 5965.25\delta^2 + 118186.51\delta^3, \tag{5.9b}$$

where $f_\alpha(\delta)$ and $f_\beta(\delta)$ denote the force functions for the activator and inhibitor bands, respectively. Fig. 5.5a,b contrast functions, $f_\alpha(\delta)$ and $f_\beta(\delta)$ with the Instron data for an experimental working strain range, $\varepsilon_0 - \varepsilon_{\max}$, accurately capturing the elastic response of these bands within this range. The lower limit, ε_0 is taken as the pre-strain in the silicone bands in the initial configuration and the upper limit, $\varepsilon_{\max}$ is chosen such that the actual strain experienced by the silicone bands in the experiment is well within this limit.

In the the activator layer, the silicone bands wrap around a quarter sector length, $0.5r\pi$ of the connecting cylinders. Therefore, the strain limits for the activator layer are calculated as:

$$\varepsilon_0 = \frac{\delta_{\alpha 0}}{L_\alpha} = \left(\frac{a + r\pi}{L_\alpha} - 1\right) \approx 10\%,\ \varepsilon_{\max} = 30\%$$

where, $L_\alpha = 83$ mm denotes the unstretched length of the elastic bands, $a = 60$ mm denotes the lattice parameter, $r = 10$ mm denotes the radius of the cylinders, and $\delta_{\alpha 0} = 8.4$ mm denotes the initial pre-stretch of the elastic bands.

While, on the the inhibitor layer, the silicone bands attach to the extended arms of the cylinders, yielding a strain range:

$$\varepsilon_0 = \frac{\delta_{\beta 0}}{L_\beta} = \left(\frac{a}{L_\beta} - 1\right) \approx 9.1\%,\ \varepsilon_{\max} = 30\%$$

where, $L_\beta = 55$ mm denotes the unstretched length of the elastic bands and $\delta_{\beta 0} = 5$ mm denotes the initial pre-stretch of the elastic bands.

Elastic interaction torque

Customized 3D printed cylinders extensions are attached to each motor shaft on the respective layer. The long cylinders of radius, r (Fig. 5.4) on the activator layer enables them to comfortably sit in a cup filled with a viscous fluid, i.e., honey and elastically interact with their intra-layer neighbours via the silicone bands. Alternately, the cylinders on the inhibitor layer are short and contain extended arms with silicone bands connecting neighbouring lattice sites at connection

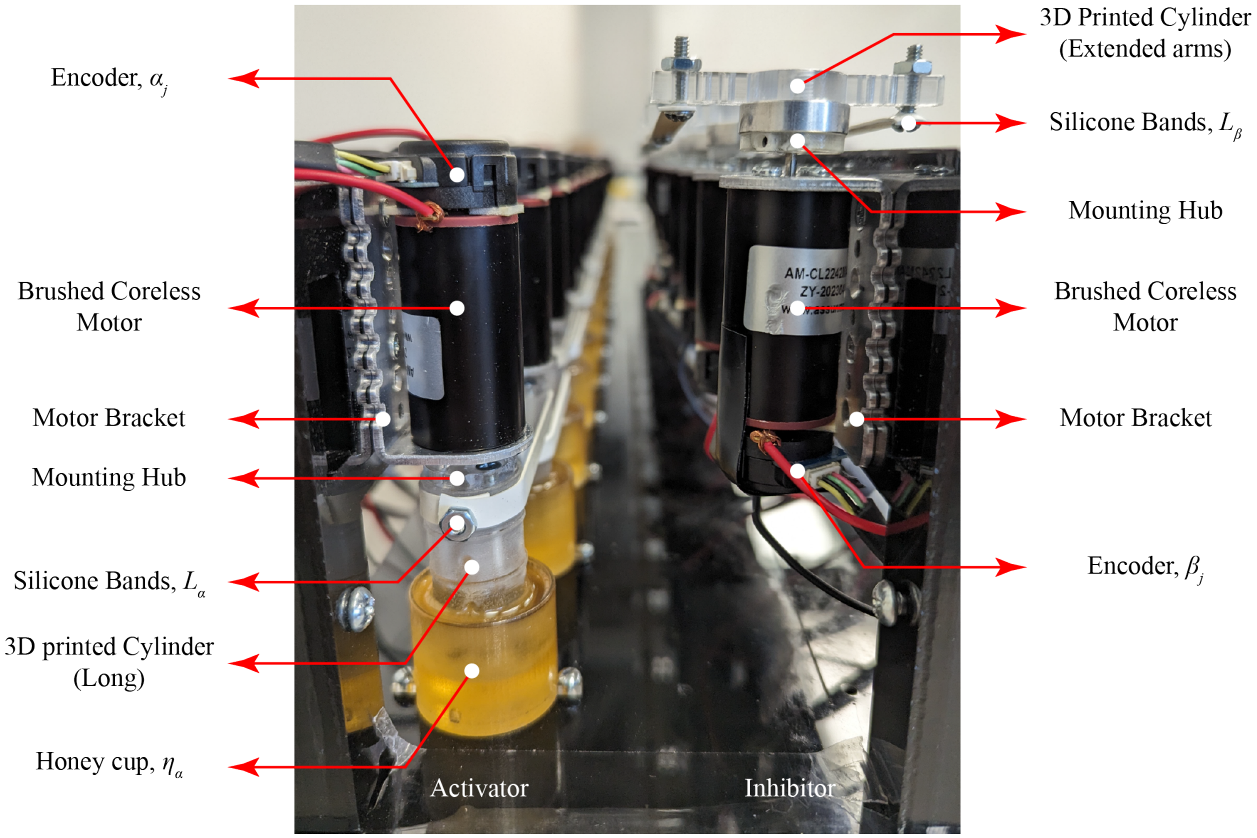

Figure 5.4: Architected Material components. Assembled view of an activator-inhibitor unit cell labelling the electrical and mechanical components.

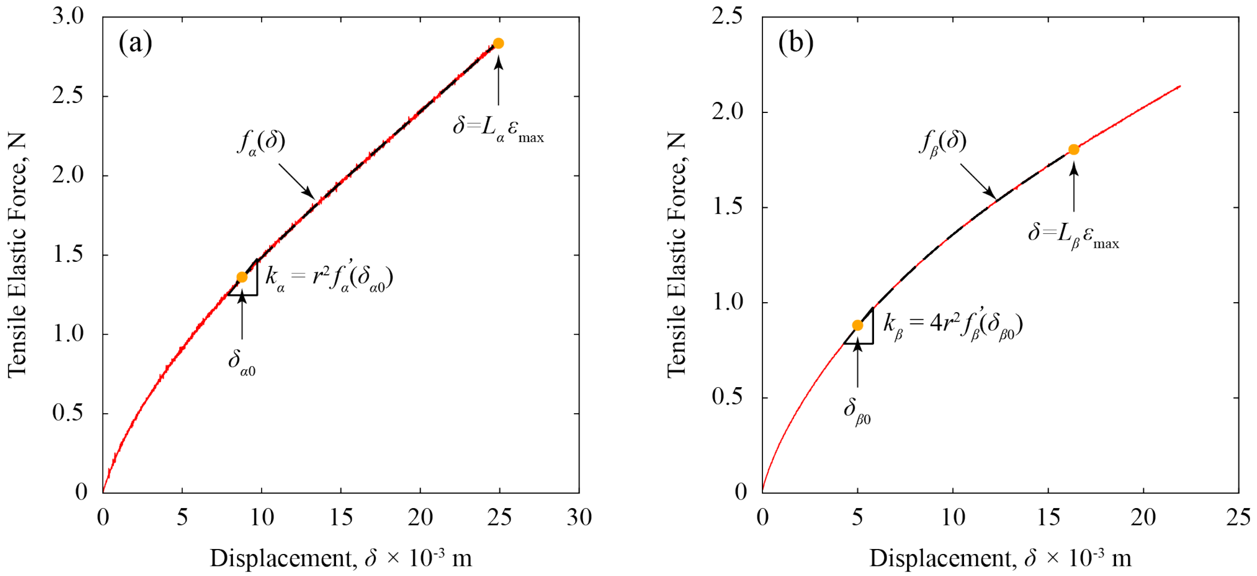

Figure 5.5: Average Force-Displacement data from Instron tests for (a) Activator silicone bands and, (b) Inhibitor silicone bands.

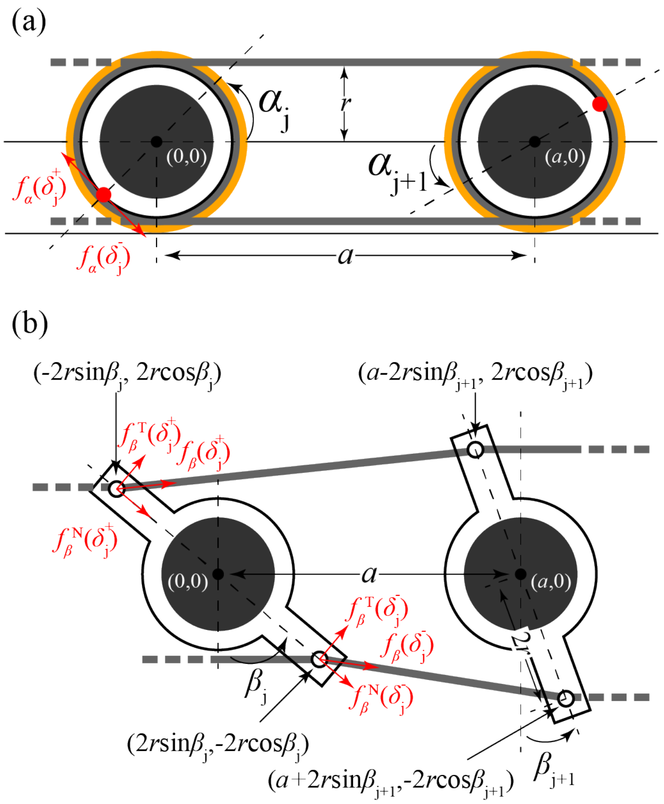

Figure 5.6: Interaction torque on (a) activator layer and (b) inhibitor layer.

points at a radial distance, $2r$ (Fig. 5.4) along these arms. This design is deliberately chosen for the following reasons:

- Connections at larger radii translate to a higher torque applied for a given spring force.
- Higher torque generation allows us to use silicone bands with a lower initial pre-tension that minimizes potential bending effects, perpendicular to the motor shaft axis on these cylinders.
- The extended arms also serve as a visual representation of the rotational Turing patterns manifested by the architected material.

Activator layer

Identifying the deformation of the pair of elastic bands between the j^{th} and $j+1^{\text{th}}$ motors on the activator layer as $\delta_j^{\pm} = \delta_{\alpha 0} \pm r(\alpha_j - \alpha_{j+1})$, the effective torque, τ_α applied on the j^{th} cylinder (Fig. 5.6a) can be expressed as:

$$\tau_\alpha(\alpha_j, \alpha_{j+1}) = \begin{cases} \left[f_\alpha(\delta_j^+) - f_\alpha(\delta_j^-)\right] r, & \text{if } \delta_j^{\pm} > 0, \\ \left[f_\alpha(\delta_j^+) - f_\alpha(0)\right] r, & \text{if } \delta_j^+ > 0, \delta_j^- < 0, \\ \left[f_\alpha(0) - f_\alpha(\delta_j^-)\right] r, & \text{if } \delta_j^+ < 0, \delta_j^- > 0, \end{cases} \tag{5.10}$$

Inhibitor layer

A similar approach using $\delta_j^{\pm} = \delta_{\beta 0} \pm \Delta_{\pm}$ where,

$$\Delta_{\pm} = \sqrt{\left[a \pm 2r(\sin\beta_j - \sin\beta_{j+1})\right]^2 + \left[\mp 2r(\cos\beta_j - \cos\beta_{j+1})\right]^2} - a$$

can be used to establish the effective torque, τ_β on the j^{th} cylinder (Fig. 5.6b) on the inhibitor layer as:

$$\tau_\beta(\beta_j, \beta_{j+1}) = \begin{cases} \left[f_\beta^{\mathrm{T}}(\delta_j^+) - f_\beta^{\mathrm{T}}(\delta_j^-)\right] 2r, & \text{if } \delta_j^{\pm} > 0, \\ \left[f_\beta^{\mathrm{T}}(\delta_j^+) - f_\beta^{\mathrm{T}}(0)\right] 2r, & \text{if } \delta_j^+ > 0, \delta_j^- < 0, \\ \left[f_\beta^{\mathrm{T}}(0) - f_\beta^{\mathrm{T}}(\delta_j^-)\right] 2r, & \text{if } \delta_j^+ < 0, \delta_j^- > 0, \end{cases} \tag{5.11}$$

where,

$$f_\beta^{\mathrm{T}}(\delta_j^{\pm}) = f_\beta(\delta_j^{\pm}) \left(\frac{\cos\beta_j \left[a \pm 2r(\sin\beta_j - \sin\beta_{j+1})\right] \mp 2r \sin\beta_j (\cos\beta_j - \cos\beta_{j+1})}{a + \Delta_{\pm}} \right), \tag{5.12}$$

denotes the tangential component of the elastic force that results in a torque on the inhibitor lattice site.

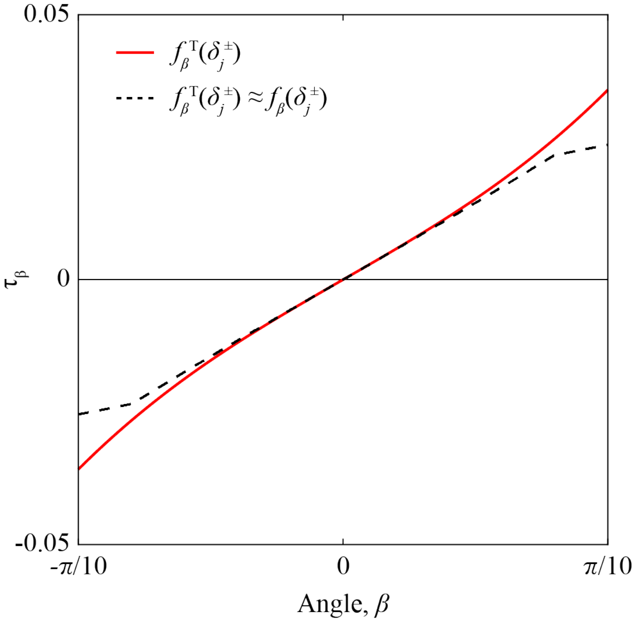

Figure 5.7: τ_β as denoted by Eq. (5.10) and Eq. (5.11).

If the change in rotations, $\beta_j - \beta_{j+1}$ on the inhibitor layer is small, $\delta_j^\pm \approx \delta_{\beta 0} \pm 2r(\beta_j - \beta_{j+1})$ and $f_\beta^{\mathrm{T}}(\delta_j^\pm) \approx f_\beta(\delta_j^\pm)$, yielding the same form as Eq. (5.10) for τ_β. Fig. 5.7 contrasts τ_β as approximated by Eq. (5.10) (dashed) and Eq. (5.11) (solid), showing a very good approximation for small angle changes between neighbouring lattice sites. As the inhibitor layer is expected to have a lower Turing pattern amplitude as compared to the activator layer, we use the Eq. (5.10) form for τ_β in our numerical model to reduce the computation time. The excellent correlation between the experimental results and the numerical simulations in Fig. 5.3, in the main text reinforces the validity of this assumption.

Electronic feedback functions

$$
\begin{aligned}
R_\alpha(\alpha,\beta) &= k_{\alpha\beta}(\beta-\alpha) - \psi'(\alpha) - \sigma\beta, \\
R_\beta(\alpha,\beta) &= k_{\alpha\beta}(\alpha-\beta),
\end{aligned}
\tag{5.13}
$$

The active, non-reciprocal feedback functions, R_α and R_β presented in Eq. (5.13), are decisive parameters, governing the non-equilibrium response of the architected material. The activator feedback function, R_α consists of three parts - a reciprocal interaction torque proportional to a spring stiffness, $k_{\alpha\beta}$ between the activator-inhibitor layers, a non-monotonic bistable torque, $\psi'(\alpha)$ and a linear, non-reciprocal feedback torque proportional to coefficient, σ. The inhibitor feedback function, R_β contains only the reciprocal interaction torque proportional to a spring stiffness, $k_{\alpha\beta}$.

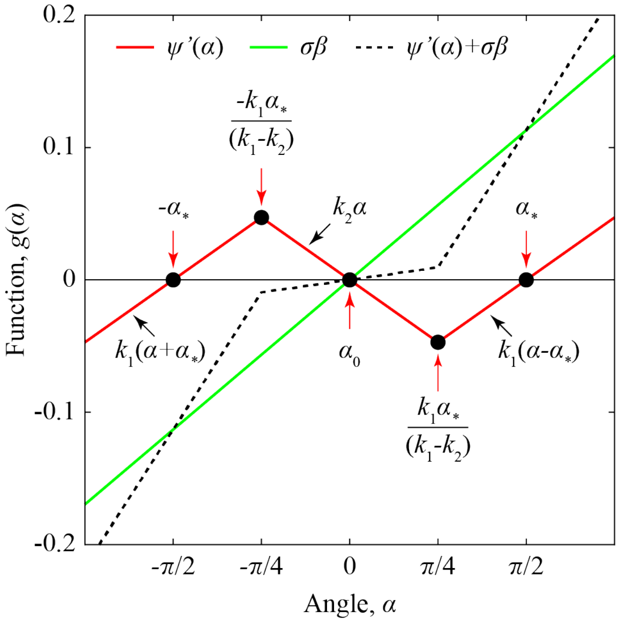

Figure 5.8: Electronic Feedback. Electro-mechanical equivalents to the reaction terms in phenomenological equations. Individual torque components, $\psi'(\alpha)$ and $\sigma\beta$ plotted for equilibrium criteria, $\beta = \alpha$, yielding a thermodynamic equilibrium at $\alpha_0 = \beta_0 = 0$ where, $\psi'(\alpha_0) + \sigma\beta_0 = 0$ (Eq. (5.15)).

Since the electronic setup operates on digital inputs and outputs, the electronic feedback can be readily correlated to a digital pulse-width modulation (PWM) value between $0-255$, provided the individual components of R_α and R_β are linear functions of encoder readings, α and β. The reciprocal spring torque and the feedback are linear functions by design. So, in order to facilitate a one-to-one correlation between the expected motor torque and the PWM signal, we emulate the qualitative characteristics of a ϕ^4-potential,[191] using a tri-linear torque function:

$$\psi'(\alpha) = \begin{cases} k_1(\alpha + \alpha_*), & \text{if } \alpha < \frac{-k_1\alpha_*}{k_1 - k_2}, \\ k_2\alpha, & \text{if } \frac{-k_1\alpha_*}{k_1-k_2} < \alpha < \frac{k_1\alpha_*}{k_1-k_2}, \\ k_1(\alpha - \alpha_*), & \text{if } \alpha > \frac{k_1\alpha_*}{k_1-k_2}, \end{cases} \tag{5.14}$$

where, $\alpha = \pm\alpha_*$ and $\alpha = 0$, respectively, represent the stable and unstable fixed points. The stable

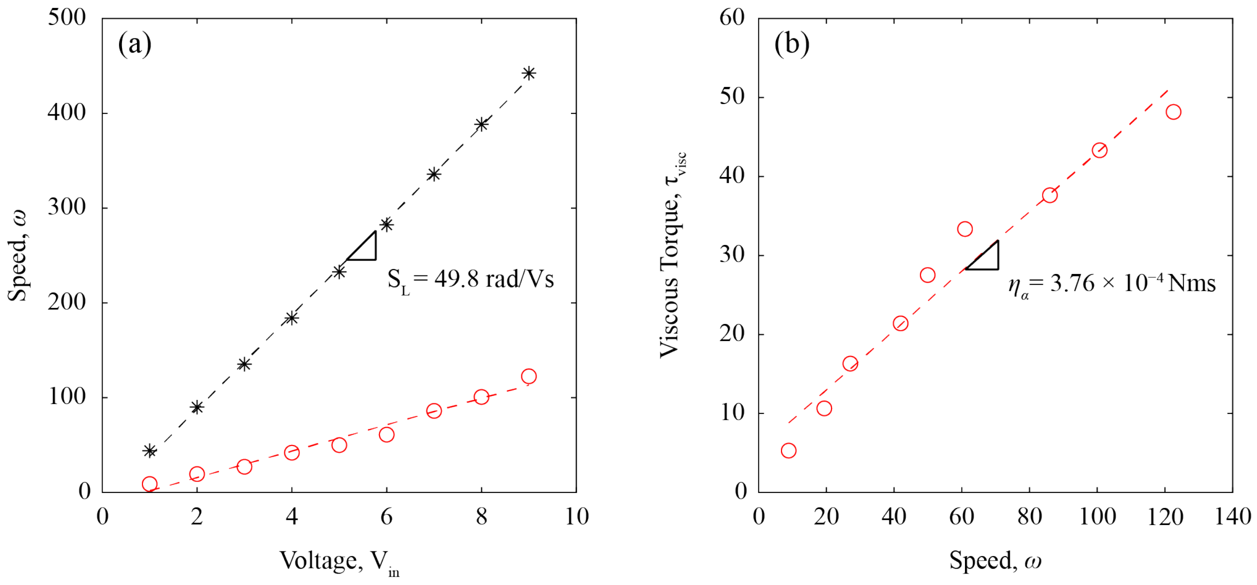

Figure 5.9: Motor Characteristics and Viscous damping coefficient of Honey. (a) Voltage, V_{in} - Speed, ω data with and without viscous effects of honey, (b) Motor speed, ω - viscous torque, τ_{visc} of honey.

fixed points for the tri-linear function used in the experiment are located at $\alpha = \pm\pi/2$. Fig. 5.8 plots the non-monotonic bistable torque and linear feedback functions used in the experiment.

Architected material - Conditional stability

The thermodynamic equilibrium for the architected material is calculated as:

$$\begin{aligned} R_\alpha(\alpha_0, \beta_0) &= k_{\alpha\beta}(\beta_0 - \alpha_0) - \psi'(\alpha_0) - \sigma\beta_0 = 0, \\ R_\beta(\alpha_0, \beta_0) &= k_{\alpha\beta}(\alpha_0 - \beta_0) = 0, \end{aligned} \tag{5.15}$$

Substituting $\psi'(\alpha)$ from Eq. (5.14) into Eq. (5.15), we get $(\alpha_0, \beta_0) = (0, 0)$. We now perform a stability analysis about the equilibrium, by linearizing the interaction torque functions as linear spring torques with stiffness:

$$k_\alpha = \left.\frac{\partial \tau_\alpha}{\partial \alpha}\right|_{\alpha=0} = r^2 \left.\frac{\partial f_\alpha}{\partial \delta}\right|_{\delta=\delta_{\alpha 0}},\ k_\beta = \left.\frac{\partial \tau_\beta}{\partial \beta}\right|_{\beta=0} = 4r^2 \left.\frac{\partial f_\beta}{\partial \delta}\right|_{\delta=\delta_{\beta 0}} \approx 3.12 k_\alpha \tag{5.16}$$

for the activator and inhibitor layer as shown in Fig. 5.5a,b. Subsequently, the elastodynamic equation can be reformulated in the continuum form:

$$\begin{aligned} \eta_\alpha \alpha_{,t} &= k_\alpha \Delta\alpha + R_\alpha(\alpha,\beta) \\ \gamma\eta_\alpha \beta_{,t} &= k_\beta \Delta\beta + R_\beta(\alpha,\beta) \end{aligned} \tag{5.17}$$

The choice of electronic motor feedback parameters, $k_{\alpha\beta} = 0.02$, $\sigma = 0.072$ and $k_1 = 0.06, k_2 = -0.06$, interaction stiffness ratio, $k_\beta/k_\alpha = 3.12$ and viscous coefficient ratio, $\gamma = \eta_\beta/\eta_\alpha \approx 0.1$, facilitates the realization of an active architected material that satisfies the conditions necessary for conditional stability:

$$k_{\alpha\beta}\left(1+\frac{1}{\gamma}\right) + k_2 > 0, \tag{5.18a}$$

$$k_{\alpha\beta}(k_2+\sigma) > 0, \tag{5.18b}$$

$$-\left(\frac{k_\beta}{k_\alpha}\right)k_2 - k_{\alpha\beta}\left(1+\frac{k_\beta}{k_\alpha}\right) > 2\sqrt{k_{\alpha\beta}\left(\frac{k_\beta}{k_\alpha}\right)(k_2+\sigma)}, \tag{5.18c}$$

manifesting periodic rotational patterns when perturbed from the thermodynamic equilibrium.

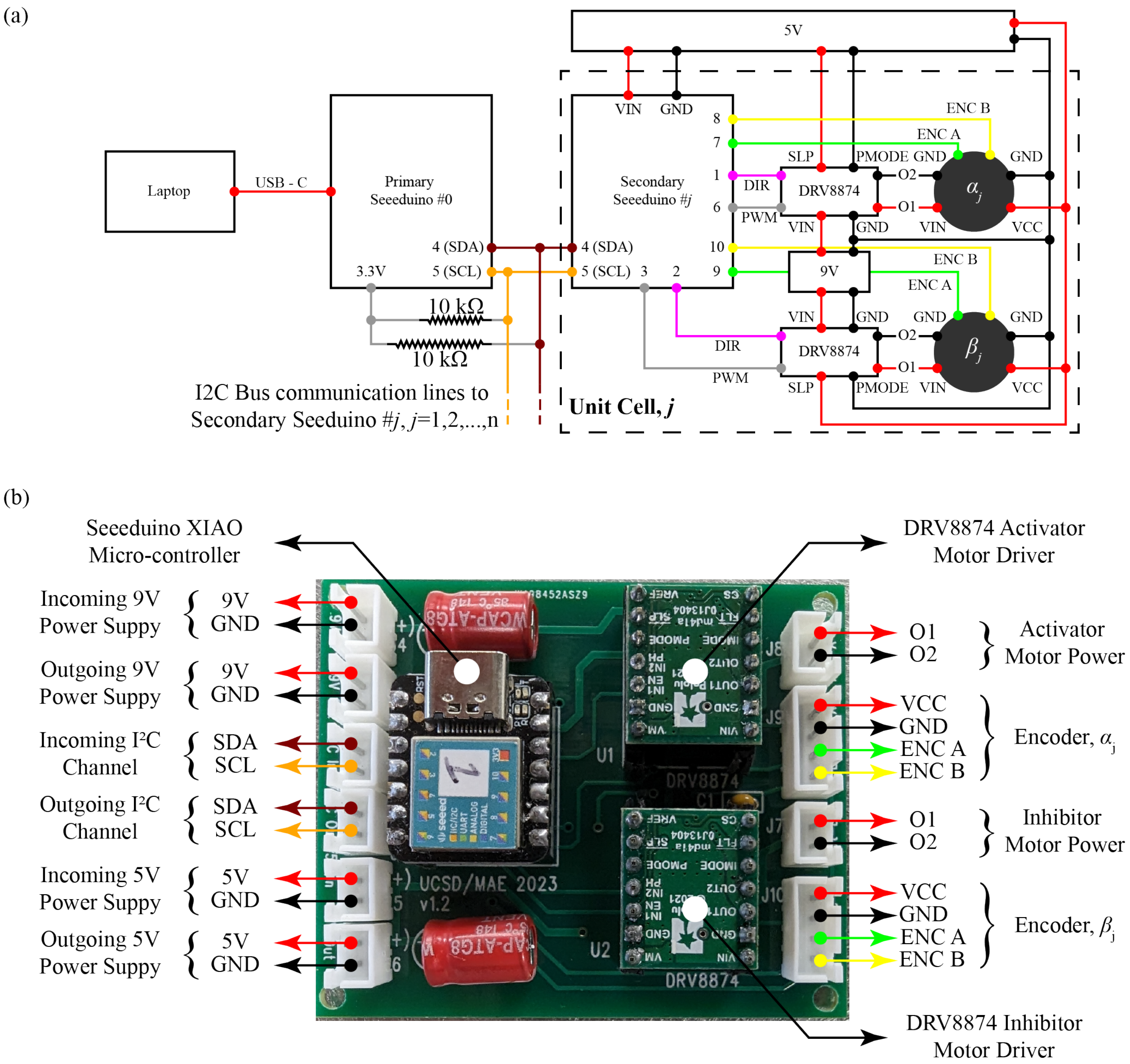

Figure 5.10: Electrical control system. (a) Electrical circuit diagram showing the internal connections within a unit cell, j of the architected material, (b) a custom built PCB circuit board with the Seeeduino XIAO micro-controller and two DRV8874 motor drivers utilized as the unit cell control system in the experiment.

Motor function and Viscous behavior

The brushed coreless motor speed is monitored at different voltages to characterize the voltage, V_{in} - no load speed, ω_{NL} behavior, plotted as $*$-markers in Fig. 5.9a. The experimental motor data suggests a linear increase in ω_{NL} with applied voltage, V_{in}, generating a proportionality constant $\mathrm{S_L} = 49.8$ rad/Vs that is in good agreement with the manufacturer data, $\mathrm{S_L^*} = 47.9$ rad/Vs, verifying the rated motor characteristics. Therefore, using the calculated motor constant, $\mathrm{S_L}$ and the motor voltage-stall torque rating of 12 V - 90 mNm, we formulate the typical linear output speed, ω - external load, τ_{ext} relation for an applied voltage, V_{in}:

$$\tau_{\mathrm{ext}} = \frac{0.09}{12}\left(\mathrm{V}_{\mathrm{in}} - \frac{\omega}{\mathrm{S_L}}\right)\ \mathrm{Nm}, \tag{5.19}$$

Note that, in the absence of any external torque or load on the motor shaft, i.e., $\tau_{\mathrm{ext}} = 0$, we recover:

$$\omega = \omega_{\mathrm{NL}} = \mathrm{S_L V_{in}},$$

The cylinders on the activator layer experience an external viscous torque, τ_{visc} as they are suspended in a honey cup. So, Eq. (5.19) will be utilized to determine the viscous coefficient of honey, η_{α}. The motor output speed, ω in the presence of a viscous medium is monitored at different applied voltages, V_{in} and this data is plotted using o-markers in Fig. 5.9a. The experimental data shows a visible decrease in output speed, ω compared to the no load speed, ω_{NL} at any given voltage, V_{in}, clearly indicating the effect of a dissipative viscous torque on the motor dynamics. The observed output speed, ω is substituted in Eq. (5.19) to determine the external viscous torque, τ_{visc} experienced by the motor shaft and plotted as a function of the output speed, ω in Fig. 5.9b. Surprisingly, the plot reveals a near linear dependence of the viscous torque on the motor speed, despite honey being classified as a non-Newtonian fluid. We verify this linear relation via multiple motor tests, allowing us to quantify the viscous coefficient of honey as the slope of this linear fit to the $\omega - \tau_{\text{visc}}$ curve:

$$\eta_\alpha = \frac{\mathrm{d}\tau_{\text{visc}}}{\mathrm{d}\omega} = 3.76 \times 10^{-4}\text{Nms}, \tag{5.20}$$

On the other hand, the inhibitor layer is not subject to any external viscous torque. Thus, the viscous coefficient on the inhibitor layer is assumed to be an order of magnitude lower than the activator layer, i.e., $\eta_\beta \approx 0.1\eta_\alpha$, in order to ensure numerical stability of our time integration scheme.[114]

Electrical control system

Fig. 5.10a represents the electrical circuit diagram for the motor control system of an isolated unit cell that provides the active feedback torques R_α and R_β. Each unit cell of the architected material comprises of a secondary Seeeduino XIAO micro-controller, encoders and motor drivers powered by a 5V-5A DC power supply and two brushed coreless motors (activator, α_j and inhibitor, β_j) controlled via the respective motor drivers. The functioning of the control system can be lucidly explained by the following iterative steps -

1. The Seeeduino micro-controller, $\#j$ receives the encoder positions, α_j and β_j from the activator (ENC A, ENC B - PIN #7, PIN #8) and inhibitor (ENC A, ENC B - PIN #9, PIN #10) motors, respectively.

2. The Seeeduino micro-controller, $\#j$ processes the active feedback torques, R_α and R_β based on the encoder values.

3. The Seeeduino micro-controller, $\#j$ then, relays a correlated direction (DIR) and pulse-width

modulation (PWM) signal via DIR, PWM - PIN #1, PIN #6 and DIR, PWM - PIN #2, PIN#3 to the DRV8874 motor drivers controlling the activator and inhibitor motors, respectively.

4. Upon receiving the DIR and PWM signals from the micro-controller, the motor drivers step down the 9V input voltage and supply the appropriate voltage across the motor terminals (O1, O2 - VIN-GND).

5. As the architected material evolves and the encoder readings change, the process repeats itself.

The electrical circuit within a given unit cell, j is self-sufficient and does not interface with the electrical circuits in the neighbouring unit cells. However, for the purpose of collecting the encoder data from all unit cells, $j = 1, 2, ..., n$ of the architected material, the secondary micro-controllers in each unit cell are connected to a primary Seeeduino micro-controller, #0 via a 3.3 V, I^{2}C bus through the SDA-SCL pins (PIN #4, PIN#5) on each micro-controller. In addition, each secondary Seeeduino micro-controller is assigned a unique address, consistent with the unit cell number, $j = 1, 2, ..., n$, to operate on this channel. The primary micro-controller then communicates with each secondary micro-controllers in sequence to extract the encoder data of the associated unit cell and relays the experimental data to a laptop via a USB-C connection, for graphical visualization and correlation with numerical simulations.

The internal connections between the micro-controller, motor drivers, the power supply lines, encoder cables and the motor power lines, in the electrical circuit in Fig. 5.10a are custom printed on a PCB board shown in Fig. 5.10b. The PCB also accommodates low capacitance capacitors across the 5V supply lines and high capacitance capacitors across the 9V supply lines and motor power lines, respectively, to protect the circuit from electrical damage due to any power surges during operation. The PCB design significantly simplifies the internal connections providing a reliable control system for the experiment.

Declaration

Chapter 5, in part, is currently being prepared for submission for publication of the material. V. Ramakrishnan and M. J. Frazier. The dissertation author is the primary author of this material.

Chapter 6

Conclusion

The studies undertaken as a part of this dissertation explore strategies to control the mesoscale phase distributions in multistable metamaterials, post-fabrication to produce a highly tunable material response. All the models presented in Chapters 2-5 introduce designs and domain control strategies, distinctly impacting the material behavior, promoting their adoption for applications in energy harvesting,[36] deployable structures and creating mechanical memory devices[192] and customizable waveguides.[67] This chapter recapitulates the core findings from each of the research investigations conducted as a part of this dissertation.

6.1 Contributions

Reviewing the tunable metamaterials literature in detail, we notice that previous attempts at tuning metamaterial performance post fabrication focused on a specific material property (predominantly the stiffness) or achieved multi-property tuning at the expense of a trade-off between properties (e.g., damping and stiffness). Chapter 2 introduces an architected material platform that can independently tune the complete triad of acoustic properties, i.e., mass, damping and stiffness, addressing the need for an architected material design capable of exhibiting a diverse set of acoustic response. Integrating kinematic amplification and geometric multistability into an asymmetric unit cell design enables a highly tunable architected material that can realize effects such as band gaps formation and migration, metadamping and adjustable sonic wave speed on a single platform.

Chapter 3 presents a related study on a tunable metamaterial design, proposing a less-invasive, strain engineering strategy to change the effective stiffness. The bi-layer material architecture consists of a metamaterial layer characterized by on-site (LOC) or interaction (INT) multistability, resting on top of an elastic foundation. The inter-layer connectivity allows us to tune the metamaterial phase distribution and the associated elastic properties by applying a quasi-static boundary strain on the elastic foundation. The metamaterial re-configuration is stable, (conditionally) reversible and happens among a finite number of acoustically unique morphologies. This approach can be readily extended to 2D designs albeit, with slight modifications to the material architecture, e.g., inclusion of defects, non-linear wave interactions with the phase boundaries, to counter the elastic curvature effects.

Identifying the centrality of the location of phase boundaries or domain walls on the material morphology and acoustic properties, Chapter 4 puts forth an approach to model these non-linear, phase transition waves (i.e., topological solitons) as a quasi-particle to accurately predict their position and velocity when subject to external spatio-temporal modulations to the elastic potential. The analytical model clearly distinguishes two distinct regimes of soliton propagation when subject to a sinusoidal spatio-temporal modulation - (1) the soliton is trapped in an initial local energy minima and carried forward by the modulation with an equivalent speed and, (2) the modulation outpaces the soliton causing it to jump between energy minimas and travel at a reduced speed. Further, to illustrate the utility of our model, we present a tractor (1D) and repulsor (2D) beam examples where, a customized external modulation counteracts the inherent energy minimizing tendency in the system to attract and repel the solitary wave away from the thermodynamic equilibrium state. The phenomenological nature of the proposed method provides an effective strategy for soliton management in any type of multistable metamaterials supporting topological solitons. Thus, the modelling and tuning methods add to the existing repertoire of design strategies being employed to produce multistable metamaterial designs for applications demanding multi-functionality.

Finally, drawing inspiration from the ability of certain biological and chemical systems governed by chemical reaction and diffusion dynamics, to exist in states far from the thermodynamic equilibrium, Chapter 5 proposes an equivalent architected material design capable of emulating these reaction-diffusion dynamics in a mechanical form. The controlled diffusion and instantaneous energy dissipation mechanisms for chemical reactions allow these natural systems to break free from the inherent energy minimizing tendencies of thermodynamics, i.e., entropy and produce peculiar steady state responses such as Turing patterns. Identifying the qualitative features and components of the reaction-diffusion process and drawing parallels to the elastodynamic wave equation, we build an architected material consisting of two elastically linked arrays of rotating cylinders where, on-site electric motors supply a customized, non-reciprocal torque based on the instantaneous rotational configuration at the relevant lattice sites. We demonstrate the formation of multi-wavelength mechanical Turing patterns in the architected material via experiments. The results open new avenues for scientific exploration into the non-equilibrium behavior of architected materials and a means to enhance their functionality, e.g., controllable shape morphing autonomous surfaces.

6.2 Future Research Directions

Overall, the multistable architected materials discussed as part of this dissertation address specific unexplored aspects of the post-fabrication material performance both in terms of the methods and outcomes of property tuning. Building upon these results and observations, the following potential research directions emerge, that pique my scientific thought and may be of interest to the metamaterials community.

- **Actuation and manifestation of multistability:** The dissertation explores the concept of multistability in metamaterials from the perspective of translational or rotational phase distributions and actuation techniques. Although, the elastodynamic equations governing the material performance provide a phenomenological framework that can recreate a similar performance using qualitatively equivalent components (e.g., photo-sensitive, thermo-sensitive, magnetic components) to facilitate non-contact actuation. Furthermore, the phase transformations within the material architecture can be engineered to manifest locomotion,[66] mechanical computation devices.[119] Therefore, exploring multistable metamaterial designs that are conducive to creation of functional devices is a relevant research direction.

- **Creating functional materials:** Chapters 2-4 present metamaterial architectures whose acoustic behavior can be programmed according to the operational requirements. Though the analytical and numerical reduced order models capture the qualitative essence of physical components, the predicted material behavior holds good only within certain limits. In experiments, we need to account for design constraints (e.g., material non-linearities, bending energies at pin-joints, gravity affecting in plane motion of masses) that can have a non-negligible affect on the material behavior. Chapter 5 is a constructive step in this regard that incorporates these experimental irregularities into the numerical model and simultaneously modifies the architected material design to accurately replicate the analytical and numerical results. Furthermore, to create functional multistable materials, the metamaterial designs and the domain control strategies need to be replicated at the appropriate length scale, conducive to the material application requirements. Therefore, investigating functional material designs is another potential area of interest.

Bibliography

[1] F. Auricchio, A. Bacigalupo, L. Gambarotta, M. Lepidi, S. Morganti, and F. Vadala, “A novel layered topology of auxetic materials based on the tetrachiral honeycomb microstructure,” *Mater. Des.*, vol. 179, p. 107883, October 2019.

[2] A. Rafsanjani and D. Pasini, “Bistable auxetic mechanical metamaterials inspired by ancient geometric motifs,” *Extreme Mech. Lett.*, vol. 9, pp. 291–296, September 2016.

[3] T. A. M. Hewage, K. L. Alderson, A. Alderson, and F. Scarpa, “Double-negative mechanical metamaterials displaying simultaneous negative stiffness and negative Poisson’s Ratio Properties,” *Adv. Mater.*, vol. 28, pp. 10323–10332, December 2016.

[4] L. Cabras, M. Brun, and D. Misseroni, “Micro-structured medium with large isotropic negative thermal expansion,” *Proc. R. Soc. A.*, vol. 475, p. 20190468, December 2019.

[5] X. Tan, B. Wang, S. Zhu, S. Chen, K. Yao, P. Xu, L. Wu, and Y. Sun, “Novel multidirectional negative stiffness mechanical metamaterials,” *Smart Mater. Struct.*, vol. 29, p. 015037, January 2020.

[6] Z. Yang, J. Mei, M. Yang, N. H. Chan, and P. Sheng, “Membrane-type acoustic metamaterial with negative dynamic mass,” *Phys. Rev. Lett.*, vol. 101, p. 204301, November 2008.

[7] B. Deng, P. Wang, Q. He, V. Tournat, and K. Bertoldi, “Metamaterials with amplitude gaps for elastic solitons,” *Nat. Commun.*, vol. 9, p. 3410, August 2018.

[8] N. X. Fang, D. Xi, J. Xu, M. Ambati, W. Srituravanich, C. Sun, and X. Zhang, “Ultrasonic metamaterials with negative modulus,” *Nat. Mater.*, vol. 5, pp. 452–456, June 2006.

[9] H. Yang and L. Ma, “Multi-stable mechanical metamaterials with shape-reconfiguration and zero Poisson’s ratio,” *Mater. Des.*, vol. 152, pp. 181–190, August 2018.

[10] G. Trainiti, Y. Xia, J. Marconi, G. Cazzulani, A. Erturk, and M. Ruzzene, “Time-periodic stiffness modulation in elastic metamaterials for selective wave filtering: theory and experiment,” *Phys. Rev. Lett.*, vol. 122, p. 124301, March 2019.

[11] Y. Xie, W. Wang, H. Chen, A. Konneker, B.-I. Popa, and S. A. Cummer, “Wavefront modulation and subwavelength diffractive acoustics with an acoustic metasurface,” *Nat. Commun.*, vol. 5, p. 5553, November 2014.

[12] A. Shelke, S. Banerjee, A. Habib, E. K. Rahani, R. Ahmed, and T. Kundu, “Wave guiding and wave modulation using phononic crystal defects,” *J. Intell. Mater. Syst. Struct.*, vol. 25, pp. 1541–1552, October 2013.

[13] N. Boechler, G. Theocharis, and C. Daraio, “Bifurcation-based acoustic switching and rectification,” *Nat. Mater.*, vol. 10, pp. 665–668, September 2011.

[14] B. Liang, X. S. Guo, J. Tu, D. Zhang, and J. C. Cheng, “An acoustic rectifier,” *Nat. Mater.*, vol. 9, pp. 989–992, December 2010.

[15] C. Ma, R. G. Parker, and B. B. Yellen, “Optimization of an acoustic rectifier for uni-directional wave propagation in periodic mass–spring lattices,” *J. Sound Vib.*, vol. 332, pp. 4876–4894, September 2013.

[16] R. A. Shelby, D. R. Smith, and S. Schultz, “Experimental verification of a negative index of refraction,” *Science*, vol. 292, pp. 77–79, April 2001.

[17] K. Sun, R. Fan, X. Zhang, Z. Zhang, Z. Shi, N. Wang, P. Xie, Z. Wang, G. Fan, H. Liu, C. Liu, T. Li, C. Yan, and Z. Guo, “An overview of metamaterials and their achievements in wireless power transfer,” *J. Mater. Chem. C*, vol. 6, pp. 2925–2943, March 2018.

[18] T. Han, T. Yuan, B. Li, and C.-W. Qiu, “Homogeneous thermal cloak with constant conductivity and tunable heat localization,” *Sci. Rep.*, vol. 3, p. 1593, March 2013.

[19] T. Han, X. Bai, D. Gao, J. T. Thong, B. Li, and C.-W. Qiu, “Experimental demonstration of a bilayer thermal cloak,” *Phys. Rev. Lett.*, vol. 112, p. 054302, March 2014.

[20] L. Xu, S. Yang, and J. Huang, “Passive metashells with adaptive thermal conductivities: chameleonlike behavior and its origin,” *Phys. Rev. Appl.*, vol. 11, p. 054071, May 2019.

[21] S. Nemat-Nasser and A. Srivastava, “Negative effective dynamics mass-density and stiffness: Micro-architecture and phononic transport in periodic composites,” *AIP Adv.*, vol. 1, p. 041502, 2011.

[22] H. H. Huang and C. T. Sun, “Wave attenuation mechanism in an acoustic metamaterial with negative effective mass density,” *New J. Phys.*, vol. 11, p. 013003, January 2009.

[23] C. Ren, D. Yang, and H. Qin, "Mechanical performance of multidirectional buckling-based negative stiffness metamaterials: an analytical and numerical study," *Materials*, vol. 11, p. 1078, July 2018.

[24] C. S. Wojnar and D. M. Kochmann, "A negative-stiffness phase in elastic composites can produce stable extreme effective dynamic but not static stiffness," *Philos. Mag.*, vol. 94, pp. 532–555, February 2014.

[25] M. I. Hussein and M. J. Frazier, "Metadamping: An emergent phenomenon in dissipative metamaterials," *J. Sound Vib.*, vol. 332, pp. 4767–4774, September 2013.

[26] L. Cabras and M. Brun, "Auxetic two-dimensional lattices with Poisson's ratio arbitrarily close to -1," *Proc. R. Soc. A.*, vol. 470, p. 20140538, December 2014.

[27] C. Körner and Y. Liebold-Ribeiro, "A systematic approach to identify cellular auxetic materials," *Smart Mater. Struct.*, vol. 24, p. 025013, December 2014.

[28] Y. Tang and J. Yin, "Design of cut unit geometry in hierarchical kirigami-based auxetic metamaterials for high stretchability and compressibility," *Extreme Mech. Lett.*, vol. 12, pp. 77–85, April 2017.

[29] K. Bertoldi, P. M. Reis, S. Willshaw, and T. Mullin, "Negative Poisson's ratio behavior induced by an elastic instability," *Adv. Mater.*, vol. 22, pp. 361–366, September 2009.

[30] S. Zhang, C. Xia, and N. X. Fang, "Broadband acoustic cloak for ultrasound waves," *Phys. Rev. Lett.*, vol. 106, p. 024301, January 2011.

[31] H. Chen and C. T. Chan, "Acoustic cloaking in three dimensions using acoustic metamaterials," *Appl. Phys. Lett.*, vol. 91, p. 183518, November 2007.

[32] S. A. Cummer, B.-I. Popa, D. Schurig, D. R. Smith, J. Pendry, M. Rahm, and A. Starr, "Scattering theory derivation of a 3D acoustic cloaking shell," *Phys. Rev. Lett.*, vol. 100, p. 024301, January 2008.

[33] C.-M. Lee and V. Goverdovskiy, "A multi-stage high-speed railroad vibration isolation system with negative stiffness," *J. Sound Vib.*, vol. 331, no. 4, pp. 914–921, 2012.

[34] K. T. Tan, H. Huang, and C. Sun, "Blast-wave impact mitigation using negative effective mass density concept of elastic metamaterials," *Int. J. Impact Eng.*, vol. 64, pp. 20–29, 2014.

[35] Y. Chen, T. Li, F. Scarpa, and L. Wang, "Lattice metamaterials with mechanically tunable poissons ratio for vibration control," *Phys. Rev. Appl.*, vol. 7, no. 2, p. 024012, 2017.

[36] M. Hwang and A. F. Arrieta, "Input-independent energy harvesting in bistable lattices from transition waves," *Sci. Rep.*, vol. 8, no. 1, pp. 1–9, 2018.

[37] X. Wang, J. Xu, J. Ding, C. Zhao, and Z. Huang, "A compact and low-frequency acoustic energy harvester using layered acoustic metamaterials," *Smart Mater. Struct.*, vol. 28, p. 025035, February 2019.

[38] T. Yang, Z.-G. Song, E. Clerkin, Y.-W. Zhang, J.-H. Sun, Y.-S. Su, L.-Q. Chen, and P. Hagedorn, "A programmable nonlinear acoustic metamaterial," *AIP Adv.*, vol. 7, p. 095323, September 2017.

[39] P. Wang, F. Casadei, S. Shan, J. C. Weaver, and K. Bertoldi, “Harnessing buckling to design tunable locally resonant acoustic metamaterials,” *Phys. Rev. Lett.*, vol. 113, p. 014301, July 2014.

[40] S. Rudykh and M. C. Boyce, “Transforming wave propagation in layered media via instability-induced interfacial wrinkling,” *Phys. Rev. Lett.*, vol. 112, p. 034301, Jan 2014.

[41] F. Casadei, T. Delpero, A. Bergamini, P. Ermanni, and M. Ruzzene, “Piezoelectric resonator arrays for tunable acoustic waveguides and metamaterials,” *J. Appl. Phys.*, vol. 112, no. 6, p. 064902, 2012.

[42] A. F. Arrieta, P. Hagedorn, A. Erturk, and D. J. Inman, “A piezoelectric bistable plate for nonlinear broadband energy harvesting,” *Appl. Phys. Lett.*, vol. 97, p. 104102, Septembder 2010.

[43] B.-J. Kwon, J.-Y. Jung, D. Lee, K.-C. Park, and I.-K. Oh, “Tunable acoustic waveguide based on vibro-acoustic metamaterials with shunted piezoelectric unit cells,” *Smart Mater. Struct.*, vol. 24, p. 105018, October 2015.

[44] P. Celli and S. Gonella, “Tunable directivity in metamaterials with reconfigurable cell symmetry,” *Appl. Phys. Lett.*, vol. 106, p. 091905, March 2015.

[45] F. Li, C. Zhang, and C. Liu, “Active tuning of vibration and wave propagation in elastic beams with periodically placed piezoelectric actuator/sensor pairs,” *J. Sound Vib.*, vol. 393, pp. 14–29, April 2017.

[46] G. Wang, J. Cheng, J. Chen, and Y. He, “Multi-resonant piezoelectric shunting induced by digital controllers for subwavelength elastic wave attenuation in smart metamaterial,” *Smart Mater. Struct.*, vol. 26, p. 025031, February 2017.

[47] H. B. Al Ba’ba’a, Z. Lin, and S. T. Tol, “Metadamping enhancement and tunability via scissor-like electromechanical metamaterials,” *J. Appl. Phys.*, vol. 130, p. 184901, November 2021.

[48] A. Darabi, E. Kliewer, and M. J. Leamy, “Reconfigurable acoustic multiplexer/demultiplexer using time division,” *Appl. Phys. Lett.*, vol. 119, p. 113501, September 2021.

[49] K. Bertoldi and M. C. Boyce, “Mechanically triggered transformations of phononic band gaps in periodic elastomeric structures,” *Phys. Rev. B*, vol. 77, p. 052105, February 2008.

[50] C. R. Tipton, E. Han, and T. Mullin, “Magneto-elastic buckling of a soft cellular solid,” *Soft Matter*, vol. 8, pp. 6880–6883, June 2012.

[51] C. T. Nelson, P. Gao, J. R. Jokisaari, C. Heikes, C. Adamo, A. Melville, S.-H. Baek, C. M. Folkman, B. Winchester, Y. Gu, Y. Liu, K. Zhang, E. Wang, J. Li, L.-Q. Chen, C.-B. Eom, D. G. Schlom, and X. Pan, “Domain dynamics during ferroelectric switching,” *Science*, vol. 334, pp. 968–971, November 2011.

[52] S. Emori, U. Bauer, S.-M. Ahn, E. Martinez, and G. S. D. Beach, “Current-driven dynamics of chiral ferromagnetic domain walls,” *Nat. Mater.*, vol. 12, pp. 611–616, July 2013.

[53] R. S. Elliott, N. Triantafyllidis, and J. A. Shaw, “Reversible stress-induced martensitic phase transformations in a bi-atomic crystal,” *J. Mech. Phys. Solids*, vol. 59, pp. 216–236, February 2011.

[54] J. A. Shaw and S. Kyriakides, “Thermomechanical aspects of NiTi,” *J. Mech. Phys. Solids*, vol. 43, pp. 1243–1281, August 1995.

[55] M. Mehboudi, B. M. Fregoso, Y. Yang, W. Zhu, A. van der Zande, J. Ferrer, L. Bellaiche, P. Kumar, and S. Barraza-Lopez, “Structural phase transition and material properties of few-layer monochalcogenides,” *Phys. Rev. Lett.*, vol. 117, p. 246802, December 2016.

[56] C. M. Wayman and K. Otsuka, *Shape Memory Materials*. Cambridge University Press, 1998. ISBN: 0521663849.

[57] D. M. Kochmann and K. Bertoldi, “Exploiting microstructural instabilities in solids and structures: from metamaterials to structural transitions,” *Appl. Mech. Rev.*, vol. 69, p. 050801, September 2017.

[58] D. Yang, L. Jin, R. V. Martinez, K. Bertoldi, G. M. Whitesides, and Z. Suo, “Phase-transforming and switchable metamaterials,” *Extreme Mech. Lett.*, vol. 6, pp. 1–9, March 2016.

[59] N. Nadkarni, C. Daraio, R. Abeyaratne, and D. M. Kochmann, “Universal energy transport law for dissipative and diffusive phase transitions,” *Phys. Rev. B*, vol. 93, p. 104109, March 2016.

[60] N. Nadkarni, A. F. Arrieta, C. Chong, D. M. Kochmann, and C. Daraio, “Unidirectional transition waves in bistable lattices,” *Phys. Rev. Lett.*, vol. 116, p. 244501, June 2016.

[61] M. J. Frazier and D. M. Kochmann, “Atomimetic mechanical structures with nonlinear topological domain evolution kinetics,” *Adv. Mater.*, p. 1605800, March 2017.

[62] M. Hwang and A. F. Arrieta, “Solitary waves in bistable lattices with stiffness grading: augmenting propagation control,” *Phys. Rev. E*, vol. 98, p. 042205, October 2018.

[63] A. P. Browning, F. G. Woodhouse, and M. J. Simpson, “Reversible signal transmission in an active mechanical metamaterial,” *Proc. R. Soc. A*, vol. 475, p. 20190146, July 2019.

[64] L. Jin, R. Khajehtourian, J. Mueller, A. Rafsanjani, V. Tournat, K. Bertoldi, and D. M. Kochmann, “Guided transition waves in multistable mechanical metamaterials,” *Proc. Natl. Acad. Sci.*, vol. 17, pp. 2319–2325, January 2020.

[65] H. Yasuda, L. M. Korpas, and J. R. Raney, “Transition waves and formation of domain walls in multistable mechanical metamaterials,” *Phys. Rev. Appl.*, vol. 13, p. 054067, May 2020.

[66] A. Zareei, B. Deng, and K. Bertoldi, “Harnessing transition waves to realize deployable structures,” *Proc. Natl. Acad. Sci.*, vol. 117, pp. 4015–4020, February 2020.

[67] V. Ramakrishnan and M. J. Frazier, “Architected material with independently tunable mass, damping, and stiffness via multi-stability and kinematic amplification,” *J. Acoust. Soc. Am.*, vol. 153, pp. 1283–1292, 02 2023.

[68] C. Yilmaz, G. M. Hulbert, and N. Kikuchi, “Phononic band gaps induced by inertial amplification in periodic media,” *Phys. Rev. B*, vol. 76, p. 054309, August 2007.

[69] J. Meaud and K. Che, “Tuning elastic wave propagation in multistable architected materials,” *Int. J. Solids Struct.*, vol. 122–123, pp. 69–80, September 2017.

[70] V. Ramakrishnan and M. J. Frazier, “Multistable metamaterial on elastic foundation enables tunable morphology for elastic wave control,” *J. Appl. Phys.*, vol. 127, p. 225104, June 2020.

[71] V. Ramakrishnan and M. J. Frazier, “Transition waves in multi-stable metamaterials with space-time modulated potentials,” *Appl. Phys. Lett.*, vol. 117, p. 151901, October 2020.

[72] F. Zangeneh-Nejad and R. Fleury, “Topological analog signal processing,” *Nat. Commun.*, vol. 10, p. 2058, May 2019.

[73] F. L. Jiménez, P. Upadhyaya, J. Liljenhjerte, P. M. Reis, and S. Kumar, “Soft optical composites for tunable transmittance,” *Extreme Mech. Lett.*, vol. 9, pp. 297–303, December 2016.

[74] O. R. Bilal, D. Ballagi, and C. Daraio, “Architected lattices for simultaneous broadband attenuation of airborne sound and mechanical vibrations in all directions,” *Phys. Rev. Appl.*, vol. 10, p. 054060, November 2018.

[75] Z. Xiao, P. Gao, D. Wang, X. He, and L. Wu, “Ventilated metamaterials for broadband sound insulation and tunable transmission at low frequency,” *Extreme Mech. Lett.*, vol. 46, p. 101348, May 2021.

[76] A. Palermo, Y. Wang, P. Celli, and C. Daraio, “Tuning of surface-acoustic-wave dispersion via magnetically modulated contact resonances,” *Phys. Rev. Appl.*, vol. 11, p. 044057, April 2019.

[77] S. Mhatre, E. Boatti, D. Melancon, A. Zareei, M. Dupont, M. Bechthold, and K. Bertoldi, “Deployable Structures Based on Buckling of Curved Beams Upon a Rotational Input,” *Adv. Funct. Mater.*, vol. 31, p. 2101144, August 2021.

[78] J. E. Pechac and M. J. Frazier, “Metamaterial design strategy for mechanical energy absorption under general loading,” *Extreme Mech. Lett.*, vol. 51, p. 101580, February 2022.

[79] S. G. Higgins, M. Becce, A. Belessiotis-Richards, H. Seong, J. E. Sero, and M. M. Stevens, “High-aspect-ratio nanostructured surfaces as biological metamaterials,” *Adv. Mater.*, vol. 32, p. 1903862, March 2020.

[80] Y. Roh, S.-H. Lee, J. Kwak, H. S. Song, S. Shin, Y. K. Kim, J. W. Wu, B.-K. Ju, B. Kang, and M. Seo, “Terahertz imaging with metamaterials for biological applications,” *Sens. Actuators, B*, vol. 352, p. 130993, February 2022.

[81] L. Fok, M. Ambati, and X. Zhang, “Acoustic metamaterials,” *MRS Bulletin*, vol. 33, pp. 931–934, October 2008.

[82] M. I. Hussein, M. J. Leamy, and M. Ruzzene, “Dynamics of phononic materials and structures: historical origins, recent progress, and future outlook,” *Appl. Mech. Rev.*, vol. 66, p. 040802, May 2014.

[83] M. Farhat, S. Guenneau, S. Enoch, A. B. Movchan, and G. G. Petursson, “Focussing bending waves via negative refraction in perforated thin plates,” *Appl. Phys. Lett.*, vol. 96, p. 081909, February 2010.

[84] S. Yang, J. H. Page, Z. Liu, M. L. Cowan, C. T. Chan, and P. Sheng, “Ultrasound Tunneling through 3D Phononic Crystals,” *Phys. Rev. Lett.*, vol. 88, p. 104301, February 2002.

[85] R. Süsstrunk and S. D. Huber, “Observation of phononic helical edge states in a mechanical topological insulator,” *Science*, vol. 349, pp. 47–50, July 2015.

[86] H. Xue, Y. Yang, F. Gao, Y. Chong, and B. Zhang, “Acoustic higher-order topological insulator on a kagome lattice,” *Nat. Mater.*, vol. 18, pp. 108–112, February 2019.

[87] M. Miniaci and R. K. Pal, “Design of topological elastic waveguides,” *J. Appl. Phys.*, vol. 130, p. 141101, October 2021.

[88] I. Antoniadis, D. Chronopoulos, V. Spitas, and D. Koulocheris, “Hyper-damping properties of a stiff and stable linear oscillator with a negative stiffness element,” *J. Sound Vib.*, vol. 346, pp. 37–52, June 2015.

[89] J. Mei, G. Ma, M. Yang, Z. Yang, W. Wen, and P. Sheng, “Dark acoustic metamaterials as super absorbers for low-frequency sound,” *Nat. Commun.*, vol. 3, p. 756, March 2012.

[90] C. Daraio, V. F. Nesterenko, E. B. Herbold, and S. Jin, “Tunability of solitary wave properties in one-dimensional strongly nonlinear phononic crystals,” *Phys. Rev. E*, vol. 73, p. 026610, February 2006.

[91] R. K. Pal, J. Rimoli, and M. Ruzzene, “Effect of large deformation pre-loads on the wave properties of hexagonal lattices,” *Smart Mater. Struct.*, vol. 25, p. 054010, May 2016.

[92] H. Dong and Y. Hu, “Harnessing fluid pre-pressure to tune the properties of phononic crystals,” *Extreme Mech. Lett.*, vol. 34, p. 100582, January 2020.

[93] Z. Wang, Q. Zhang, K. Zhang, and G. Hu, “Tunable digital metamaterial for broadband vibration isolation at low frequency,” *Adv. Mater.*, vol. 28, pp. 9857–9861, November 2016.

[94] S. Liu, Y. Zhao, D. Zhao, J. Wu, and C. Gao, “Tunable elastic wave bandgaps and waveguides by acoustic metamaterials with magnetorheological elastomer,” *Acoust. Phys.*, vol. 66, pp. 123–131, March 2020.

[95] A. S. Gliozzi, M. Miniaci, A. Chiappone, A. Bergamini, B. Morin, and E. Descrovi, “Tunable photo-responsive elastic metamaterials,” *Nat. Commun.*, vol. 11, May 2020.

[96] X. Ge, H. Xiang, Y. Liu, J. Shen, Y. Li, and Y. Li, “Utilizing reversible solid-liquid phase transition to tune phononic bandgaps,” *AIP Adv.*, vol. 11, p. 125323, December 2021.

[97] P. Celli and S. Gonella, “Manipulating waves with LEGO (R) bricks: A versatile experimental platform for metamaterial architectures,” *Appl. Phys. Lett.*, vol. 107, p. 081901, August 2015.

[98] Q. Zhang, K. Zhang, and G. Hu, “Tunable fluid-solid metamaterials for manipulation of elastic wave propagation in broad frequency range,” *Appl. Phys. Lett.*, vol. 112, p. 221906, June 2018.

[99] Q. Zhang, Y. Chen, K. Zhang, and G. Hu, “Programmable elastic valley Hall insulator with tunable interface propagation routes,” *Extreme Mech. Lett.*, vol. 28, pp. 76–80, April 2019.

[100] M. D. Schaeffer and M. Ruzzene, “Wave propagation in multistable magneto-elastic lattices,” *Int. J. Solids Struct.*, vol. 56–57, pp. 78–95, March 2015.

[101] M. J. Frazier and D. M. Kochmann, “Band gap transmission in periodic bistable mechanical systems,” *J. Sound Vib.*, vol. 388, pp. 315–326, February 2017.

[102] J. Meaud, “Multistable two-dimensional spring-mass lattices with tunable band gaps and wave directionality,” *J. Sound Vib.*, vol. 434, pp. 44–62, November 2018.

[103] Z. Wu, Y. Zheng, and K. W. Wang, “Metastable modular metastructures for on-demand reconfiguration of band structures and nonreciprocal wave propagation,” *Phys. Rev. E*, vol. 97, p. 022209, February 2018.

[104] M. J. Frazier, “Multi-stable acoustic metamaterials with re-configurable mass distribution,” *J. Appl. Phys.*, vol. 131, p. 165105, April 2022.

[105] N. M. M. Frandsen, O. R. Bilal, J. S. Jensen, and M. I. Hussein, “Inertial amplification of continuous structures: Large band gaps from small masses,” *J. Appl. Phys.*, vol. 119, p. 124902, March 2016.

[106] V. Settimi, M. Lepidi, and A. Bacigalupo, “Nonlinear dispersion properties of one-dimensional mechanical metamaterials with inertia amplification,” *Int. J. Mech. Sci.*, vol. 201, p. 106461, July 2021.

[107] H. B. Al Ba’ba’a, X. Zhu, and Q. Wang, “Enabling novel dispersion and topological characteristics in mechanical lattices via stable negative inertial coupling,” *Proc. R. Soc. A*, vol. 477, p. 20200820, August 2021.

[108] S. Adhikari and A. Banerjee, “Enhanced low-frequency vibration energy harvesting with inertial amplifiers,” *J. Intell. Mater. Syst. Struct.*, vol. 33, pp. 822–838, August 2021.

[109] M. I. Hussein and M. J. Frazier, “Band structure of phononic crystals with general damping,” *J. Appl. Phys.*, vol. 108, p. 093506, November 2010.

[110] M. I. Hussein, I. Patrick, A. Banerjee, and S. Adhikari, “Metadamping in inertially amplified metamaterials: trade-off between spatial attenuation and temporal attenuation,” *J. Sound Vib.*, vol. 531, p. 116977, August 2022.

[111] A. Aladwani, A. Mohammed, and M. Nouh, “Tunable dissipation in elastic metamaterials via methodic reconfiguration of inertant mechanical networks,” *Meccanica*, vol. 57, pp. 1337–1352, February 2022.

[112] D. Krattiger, R. Khajehtourian, C. L. Bacquet, and M. I. Hussein, “Anisotropic dissipation in lattice metamaterials,” *AIP Adv.*, vol. 6, no. 12, p. 121802, 2016.

[113] S. Sengupta and S. Li, “Harnessing the anisotropic multistability of stacked-origami mechanical metamaterials for effective modulus programming,” *J. Intell. Mater. Syst. Struct*, vol. 29, no. 14, pp. 2933–2945, 2018.

[114] G. Noh and K.-J. Bathe, “An explicit time integration scheme for the analysis of wave propagations,” *Comput. Struct.*, vol. 129, pp. 178–193, August 2013.

[115] M. Maldovan, “Sound and heat revolutions in phononics,” *Nature*, vol. 503, pp. 209–217, November 2013.

[116] S. A. Cummer and D. Schurig, “One path to acoustic cloaking,” *New J. Phys.*, vol. 9, p. 45, March 2007.

[117] N. Stenger, M. Wilhelm, and M. Wegener, “Experiments on elastic cloaking in thin plates,” *Phys. Rev. Lett.*, vol. 108, p. 014301, January 2012.

[118] M. Ambati, N. Fang, C. Sun, and X. Zhang, “Surface resonant states and superlensing in acoustic metamaterials,” *Phys. Rev. B*, vol. 75, p. 195447, May 2007.

[119] O. R. Bilal, A. Foehr, and C. Daraio, “Bistable metamaterial for switching and cascading elastic vibrations,” *Proc. Natl. Acad. Sci.*, vol. 114, pp. 4603–4606, May 2017.

[120] J.-F. Robillard, K. Muralidharan, J. Bucay, P. A. Deymier, W. Beck, and D. Barker, “Phononic metamaterials for thermal management: an atomistic computational study,” *Chin. J. Phys.*, vol. 49, pp. 448–461, February 2011.

[121] R. Schittny, M. Kadic, S. Guenneau, and M. Wegener, “Experiments on transformation thermodynamics: molding the flow of heat,” *Phys. Rev. Lett.*, vol. 110, p. 195901, May 2013.

[122] Y. Pennec, B. Djafari-Rouhani, J. O. Vasseur, A. Khelif, and P. A. Deymier, “Tunable filtering and demultiplexing in phononic crystals with hollow cylinders,” *Phys. Rev. E*, vol. 69, p. 046608, April 2004.

[123] R. Fleury, D. Sounas, and A. Alu, “An invisible acoustic sensor based on parity-time symmetry,” *Nat. Commun.*, vol. 6, January 2015.

[124] C.-S. Park, Y. C. Shin, S.-H. Jo, H. Yoon, W. Choi, B. D. Youn, and M. Kim, “Two-dimensional octagonal phononic crystals for highly dense piezoelectric energy harvesting,” *Nano Energy*, vol. 57, pp. 327–337, March 2019.

[125] J. Henneberg, A. Gerlach, H. Cebulla, and S. Marburg, “The potential of stop band material in multi-frequency ultrasonic transducers,” *J. Sound Vib.*, vol. 452, pp. 132–146, July 2019.

[126] A. Colombi, D. Colquitt, P. Roux, S. Guenneau, and R. V. Craster, “A seismic metamaterial: the resonant metawedge,” *Sci. Rep.*, vol. 6, p. 27717, June 2016.

[127] S. Brûlé, E. H. Javelaud, S. Enoch, and S. Guenneau, “Experiments on seismic metamaterials: molding surface waves,” *Phys. Rev. Lett.*, vol. 112, p. 133901, March 2014.

[128] O. Thorp, M. Ruzzene, and A. Baz, “Attenuation and localization of wave propagation in rods with periodic shunted piezoelectric patches,” *Smart Mater. Struct.*, vol. 10, pp. 979–989, October 2001.

[129] L. Airoldi and M. Ruzzene, “Design of tunable acoustic metamaterials through periodic arrays of resonant shunted piezos,” *New J. Phys.*, vol. 13, p. 113010, November 2011.

[130] X. Zhu, G. Wu, R. Dong, C.-M. Chen, and S. Yang, “Capillarity induced instability in responsive hydrogel membranes with periodic hole array,” *Soft Matter*, vol. 8, pp. 8088–8093, April 2012.

[131] F. Casadei and K. Bertoldi, “Harnessing fluid-structure interactions to design self-regulating acoustic metamaterials,” *J. Appl. Phys.*, vol. 115, p. 034907, January 2014.

[132] S. Shan, S. H. Kang, P. Wang, C. Qu, S. Shian, E. R. Chen, and B. Katia, “Harnessing multiple folding mechanisms in soft periodic structures for tunable control of elastic waves,” *Adv. Funct. Mater.*, vol. 24, pp. 4935–4942, May 2014.

[133] A. Rafsanjani and K. Bertoldi, “Buckling-induced kirigami,” *Phys. Rev. Lett.*, vol. 118, p. 084301, February 2017.

[134] J. R. Raney, N. Nadkarni, C. Daraio, D. M. Kochmann, J. A. Lewis, and K. Bertoldi, "Stable propagation of mechanical signals in soft media using stored elastic energy," *Proc. Natl. Acad. Sci.*, vol. 113, pp. 9722–9727, 2016.

[135] X. Xia, A. Afshar, H. Yang, C. M. Portela, D. M. Kochmann, C. V. Di Leo, and J. R. Greer, "Electrochemically reconfigurable architected materials," *Nature*, vol. 573, p. 205213, September 2019.

[136] N. Nadkarni, C. Daraio, and D. M. Kochmann, "Dynamics of periodic mechanical structures containing bistable elastic elements: From elastic to solitary wave propagation," *Phys. Rev. E*, vol. 90, p. 023204, August 2014.

[137] G. Catalan, A. Lubk, A. H. G. Vlooswijk, E. Snoeck, C. Magen Dominguez, A. Janssens, G. Rispens, G. Rijnders, D. H. A. Blank, and B. Noheda, "Flexoelectric rotation of polarization in ferroelectric thin films," *Nat. Mater.*, vol. 10, pp. 963–967, December 2011.

[138] Z. Dai, L. Liu, and Z. Zhang, "Strain engineering of 2D materials: issues and opportunities at the interface," *Adv. Mater.*, vol. 0, p. 1805417, January 2019.

[139] S. M. Allen and J. W. Cahn, "A microscopic theory for antiphase boundary motion and its application to antiphase domain coarsening," *Acta Metall.*, vol. 27, pp. 1085–1095, June 1979.

[140] S. Janbaz, R. Hedayati, and A. A. Zadpoor, "Programming the shape-shifting of flat soft matter: from self-rolling/self-twisting materials to self-folding origami," *Mater. Horiz.*, vol. 3, pp. 536–547, August 2016.

[141] K. W. Yung, P. B. Landecker, and D. D. Villani, “An analytic solution for the force between two magnetic dipoles,” *Magn. Electr. Separ.*, vol. 9, pp. 39–52, 1998.

[142] D. J. Griffiths, *Introduction to Electrodynamics*. Boston: Pearson, 2013.

[143] M. Remoissenet, *Waves called solitons: concepts and experiments*. Springer Science & Business Media, 2013.

[144] M. Peyrard, *Nonlinear Excitations in Biomolecules*. Springer, 1995. ISBN: 978-3-540-59250-1.

[145] J. Berry, C. P. Brangwynne, and M. Haataja, “Physical principles of intracellular organization via active and passive phase transitions,” *Rep. Prog. Phys.*, vol. 80, p. 046601, April 2018.

[146] Y. Hanif and U. Saleem, “Coupled sine-Gordon systems in living cellular structure,” *Mod. Phys. Lett. B*, vol. 34, p. 2050070, January 2020.

[147] A. J. Heeger, S. Kivelson, J. R. Schrieffer, and W. P. Su, “Solitons in conducting polymers,” *Rev. Mod. Phys.*, vol. 60, pp. 781–850, July 1988.

[148] G. Kalosakas, A. V. Zolotaryuk, G. P. Tsironis, and E. N. Economou, “Propagation of solitons in hydrogen-bonded chains with mass variation,” *Phys. Rev. E*, vol. 56, pp. 1088–1096, July 1997.

[149] V. A. Belinski and E. Verdaguer, *Gravitational Solitons*. Cambridge University Press, 2001. ISBN: 0-521-80586-4.

[150] G. A. Alekseev, “Collision of strong gravitational and electromagnetic waves in the expanding universe,” *Phys. Rev. D*, vol. 93, p. 061501, March 2016.

[151] Y. I. Frenkel and T. Kontorova, “On the theory of plastic deformation and twinning,” *J. Phys.*, vol. 1, pp. 137–149, 1939.

[152] P. Bak, “Commensurate phases, incommensurate phases and the devil’s staircase,” *Rep. Prog. Phys.*, vol. 45, pp. 587–629, 1982.

[153] T.-H. Kim, S. Cheon, and H. W. Yeom, “Switching chiral solitons for algebraic operation of topological quaternary digits,” *Nat. Phys.*, vol. 13, pp. 444–447, May 2017.

[154] C. Yang, Q. Zhou, H. Triki, M. Mirzazadeh, M. Ekici, W.-J. Liu, A. Biswas, and M. Belic, “Bright soliton interactions in a (2+1)-dimensional fourth-order variable-coefficient nonlinear Schrodinger equation for the Heisenberg ferromagnetic spin chain,” *Nonlinear Dyn.*, vol. 95, pp. 983–994, January 2019.

[155] P. J. Pascual and L. Vázquez, “Sine-Gordon solitons under weak stochastic perturbations,” *Phys. Rev. B*, vol. 32, pp. 8305–8311, December 1985.

[156] P. Biller and F. Petruccione, “Dynamics of sine-Gordon solitons under random perturbations: Weak additive large-scale white noise,” *Phys. Rev. B*, vol. 41, pp. 2139–2144, February 1990.

[157] J. A. González, A. Marcano, B. A. Mello, and L. Trujillo, “Controlled transport of solitons and bubbles using external perturbations,” *Chaos Solit.*, vol. 28, pp. 804–821, May 2006.

[158] M. T. Islam, X. S. Wang, and X. R. Wang, “Thermal gradient driven domain wall dynamics,” *J. Phys. Condens. Matter*, vol. 31, p. 455701, November 2019.

[159] D. Zhang, D. Sando, P. Sharma, X. Cheng, F. Ji, V. Govinden, M. Weyland, V. Nagarajan, and J. Seidel, “Superior polarization retention through engineered domain wall pinning,” *Nat. Commun..*, vol. 11, p. 349, January 2020.

[160] T. Dauxois and M. Peyrard, *Physics of Solitons*. Cambridge University Press, 2006. ISBN: 0-521-85421-0.

[161] D. J. Bergman, E. Ben-Jacob, Y. Imry, and K.-i. Maki, “Sine-Gordon solitons: particles obeying relativistic dynamics,” *Phys. Rev. A*, vol. 27, pp. 3345–3348, June 1983.

[162] E. J. Markvicka, M. D. Bartlett, X. Huang, and C. Majidi, “An autonomously electrically self-healing liquid metal-elastomer composite for robust soft-matter robotics and electronics,” *Nat. Mater.*, vol. 17, pp. 618–624, July 2018.

[163] C. Majidi, “Soft-matter engineering for soft robotics,” *Adv. Mater. Technol. (Weinheim, Ger.)*, vol. 4, p. 1800477, February 2019.

[164] R. Stein and Å. Nordlund, “Simulations of solar granulation. i. general properties,” *Astrophys. J.*, vol. 499, no. 2, p. 914, 1998.

[165] V. Cornish, “On the formation of sand-dunes,” *Geogr.*, vol. 9, no. 3, pp. 278–302, 1897.

[166] A. M. Zhabotinsky and A. N. Zaikin, “Autowave processes in a distributed chemical system,” *J. Theor. Biol.*, vol. 40, pp. 45–61, July 1973.

[167] S. Kondo and T. Miura, “Reaction-diffusion model as a framework for understanding biological pattern formation,” *Science*, vol. 329, pp. 1616–1620, September 2010.

[168] S. Kondo and R. Asai, “A reaction–diffusion wave on the skin of the marine angelfish pomacanthus,” *Nature*, vol. 376, no. 6543, pp. 765–768, 1995.

[169] R. Dillon, P. Maini, and H. Othmer, “Pattern formation in generalized turing systems: I. steady-state patterns in systems with mixed boundary conditions,” *J. Math. Biol.*, vol. 32, pp. 345–393, 1994.

[170] J. J. Tyson and J. P. Keener, “Singular perturbation theory of traveling waves in excitable media (a review),” *Phys. D*, vol. 32, no. 3, pp. 327–361, 1988.

[171] P. Arcuri and J. D. Murray, “Pattern sensitivity to boundary and initial conditions in reaction-diffusion models,” *J. Math. Biol.*, vol. 24, no. 2, pp. 141–165, 1986.

[172] G. Nicolis and I. Prigogine, “Symmetry breaking and pattern selection in far-from-equilibrium systems,” *Proc. Natl. Acad. Sci.*, vol. 78, no. 2, pp. 659–663, 1981.

[173] A. M. Turing, “The chemical basis of morphogenesis,” *Philos. Trans. R. Soc., B*, vol. 237, pp. 37–72, August 1952.

[174] B.-W. Li, L.-Y. Deng, and H. Zhang, “Chiral symmetry breaking in a reaction-diffusion system,” *Phys. Rev. E*, vol. 87, no. 4, p. 042905, 2013.

[175] Q. Zheng and J. Shen, “Pattern formation in the fitzhugh–nagumo model,” *Comput. Math. Appl.*, vol. 70, no. 5, pp. 1082–1097, 2015.

[176] L. Weise, *Spiral Wave Initiation in Reaction-Diffusion-Mechanics Systems: A Model for the Onset of Reentrant Cardiac Arrhythmia*. PhD thesis, Utrecht University, 2012.

[177] J. Bard and I. Lauder, "How well does turing's theory of morphogenesis work?," *J. Theor. Biol.*, vol. 45, no. 2, pp. 501–531, 1974.

[178] Y. R. Zelnik, H. Uecker, U. Feudel, and E. Meron, "Desertification by front propagation?," *J. Theor. Biol.*, vol. 418, pp. 27–35, 2017.

[179] K. F. Graff, *Wave Motion in Elastic Solids*. Mineola, New York: Dover Publications, 1991.

[180] J. D. Achenbach, *Wave Propagation in Elastic Solids*. London: North-Holland, 1999.

[181] A. A. Maznev, A. G. Every, and O. B. Wright, "Reciprocity in reflection and transmission: What is a 'phonon diode'?," *Wave Motion*, vol. 50, pp. 776–784, June 2013.

[182] B. Liang, B. Yuan, and J.-c. Cheng, "Acoustic diode: rectification of acoustic energy flux in one-dimensional systems," *Phys. Rev. Lett.*, vol. 103, p. 104301, September 2009.

[183] Y. Song, R. M. Panas, S. Chizari, L. A. Shaw, J. A. Jackson, J. B. Hopkins, and A. J. Pascall, "Additively manufacturable micro-mechanical logic gates," *Nat. Commun.*, vol. 10, no. 1, p. 882, 2019.

[184] J. T. Overvelde, T. Kloek, J. J. Dhaen, and K. Bertoldi, "Amplifying the response of soft actuators by harnessing snap-through instabilities," *Proc. Natl. Acad. Sci.*, vol. 112, no. 35, pp. 10863–10868, 2015.

[185] T. Chen, O. R. Bilal, K. Shea, and C. Daraio, “Harnessing bistability for directional propulsion of soft, untethered robots,” *Proc. Natl. Acad. Sci.*, vol. 115, no. 22, pp. 5698–5702, 2018.

[186] E. J. Crampin, E. A. Gaffney, and P. K. Maini, “Reaction and diffusion on growing domains: scenarios for robust pattern formation,” *Bull. Math. Biol.*, vol. 61, no. 6, pp. 1093–1120, 1999.

[187] R. FitzHugh, “Mathematical models of threshold phenomena in the nerve membrane,” *Bull. math. biophys*, vol. 17, pp. 257–278, 1955.

[188] R. FitzHugh, “Impulses and physiological states in theoretical models of nerve membrane,” *Biophys. J.*, vol. 1, pp. 445–466, July 1961.

[189] R. FitzHugh, “Mathematical models of excitation and propagation in nerve,” *Biol. Eng.*, vol. 9, pp. 1–85, 1969.

[190] J. Nagumo, S. Animoto, and S. Yoshizawa, “An active pulse transmission line simulating nerve axon,” *Proc. IRE*, vol. 50, pp. 2061–2070, October 1962.

[191] Z. Fei, V. V. Konotop, M. Peyrard, and L. Vázquez, “Kink dynamics in the periodically modulated φ^4 model,” *Phys. Rev. E*, vol. 48, pp. 548–554, July 1993.

[192] J. E. Pechac and M. J. Frazier, “Mechanical multi-level memory from multi-stable metamaterial,” *Appl. Phys. Lett.*, vol. 122, no. 21, 2023.